Topology and Correlations in Twisted Bilayer Graphene

Yves Hon Kwan

St Hugh's College

University of Oxford

A thesis submitted for the degree of

Doctor of Philosophy in Theoretical Physics

Trinity 2022

Acknowledgements

I am grateful to my supervisor Sid Parameswaran for his guidance and mentorship, both before and during my DPhil. Not only have I benefitted from his wealth of knowledge and ideas, I have also learned to become a better physicist from him. His boundless enthusiasm and energy for physics, which seem to be constants of nature, never cease to amaze me.

A special thanks to Glenn Wagner, Nick Bultinck and Steve Simon, the other members of the moiré mini-group, with whom I have had fruitful collaborations and countless discussions.

I am indebted to Shivaji Sondhi, without whom I would not be here pursuing my dreams in physics today. He has been a constant source of wisdom throughout my graduate career. Leela Sondhi deserves a special mention for her astute questioning. I am also thankful to John Chalker for guiding my first steps into condensed matter physics during my masters.

I have benefitted greatly from interactions with many colleagues, whether through discussions, collaboration, advice, or friendship. In particular, I would like to thank Sounak Biswas, Nilotpal Chakraborty, Amos Chan, Amalia Coldea, Trithep Devakul, Michele Fava, Yuval Gefen, Greg Henderson, Yichen Hu, Joe Huxford, Ming-Hao Li, Abhishodh Prakash, Patrick Wilhelm, and Sanfeng Wu.

Special thanks to Amartya and Sharan, who I have had the pleasure of being stuck with during numerous lockdowns.

I am also grateful to Rachel for her patience, company, and encouragement.

Last, but certainly not least, I would like to thank my parents. I am eternally grateful for their unconditional love and support.

Abstract

This thesis studies several examples of how topology and interactions lead to novel electronic phenomena in magic-angle twisted bilayer graphene, a moiré heterostructure that has attracted much attention owing its diversity of experimentally-observed correlated phases.

Part I focuses on neutral and charged excitations of the correlated insulators predicted within the strong coupling framework, which emphasizes the close connections of the central moiré bands to quantum Hall ferromagnetism. In Chapter 3, we show that topological excitons can be formed from the quantized anomalous Hall insulator at filling factor $\nu = +3$, and explore the possibility of a new excitonic fractional quantum Hall hierarchy. In Chapter 4, we study the properties of the three classes of domain walls that separate topological domains in this insulator. In Chapter 5, we use microscopic Hartree-Fock numerics to analyze charged spin and pseudospin skyrmions at various integer fillings, with an emphasis on the pairing of pseudospin skyrmions and its consequences for skyrmion superconductivity.

Part II reconsiders the prevailing normal state phase diagrams of the strong coupling framework. In Chapter 6, we explore the effects of heterostrain, and demonstrate the emergence of a new electronic order, the incommensurate Kekulé spiral, which possesses an unusual form of multiscale translation symmetry breaking. We argue that the phenomenology of the intermediate coupling regime is consistent with many experiments, and that strain and the incommensurate Kekulé spiral are ingredients that should play important roles in any umbrella theory of twisted bilayer graphene.

Abbreviations

We list the abbreviations used in this thesis, in order of their appearance:

- vdW: van der Waals (page 1)
- TBG: twisted bilayer graphene (page 1)
- BZ: Brillouin zone (page 2)
- vHS: van Hove singularity (page 2)
- STM: scanning tunneling microscopy (page 2)
- STS: scanning tunneling spectroscopy (page 2)
- CN: charge neutrality (page 3)
- TTG: twisted trilayer graphene (page 3)
- mBZ: moiré Brillouin zone (page 4)
- LL: Landau level (page 4)
- QAH: quantized anomalous Hall (page 5)
- HF: Hartree-Fock (page 6)
- QHFM: quantum Hall ferromagnetism (page 7)
- KIVC: Kramers intervalley coherent (page 7)
- TRS: time-reversal symmetry (page 12)
- BM: Bistritzer-MacDonald model (page 13)
- PHS: particle-hole symmetry (page 15)

- AFM: antiferromagnetic (page 25)
- IVC: intervalley coherent (page 25)
- PH: particle-hole (page 27)
- COM: centre-of-mass (page 27)
- LLL: lowest Landau level (page 29)
- FQH: fractional quantum Hall (page 37)
- FVPI: fully valley-polarized insulator (page 37)
- e-CFL: excitonic composite Fermi liquid (page 42)
- DW: domain wall (page 46)
- NLSM: non-linear sigma model (page 48)
- HFWQ: Hartree-Fock Wannier-Qi (page 51)
- SQUID: scanning superconducting quantum interference device (page 55)
- BKT: Berezenskii-Kosterlitz-Thouless (page 65)
- KD: Kekulé distortion (page 79)
- IKS: incommensurate Kekulé spiral (page 86)
- TSB: translation symmetry-breaking (page 86)
- NLT: non-local tunneling (page 91)
- SM: semimetal (page 92)
- VH: valley Hall (page 92)

Publications

Publications marked with a dagger (†) are discussed in this thesis:

13. **Spin skyrmion gaps as signatures of intervalley-coherent insulators in magic-angle twisted bilayer graphene**
    Jiachen Yu, Benjamin A. Foutty, Yves H. Kwan (co-first author), Mark E. Barber, Kenji Watanabe, Takashi Taniguchi, Zhi-Xun Shen, Siddharth A. Parameswaran, Benjamin E. Feldman
    arXiv:2206.11304

12. †**Skyrmions in twisted bilayer graphene: stability, pairing, and crystallization**
    Yves H. Kwan, Glenn Wagner, Nick Bultinck, Steven H. Simon, S.A. Parameswaran
    arXiv:2112.06936 | *Phys. Rev. X* **12**, 031020 (2022)

11. †**Global phase diagram of twisted bilayer graphene above T_c**
    Glenn Wagner, Yves H. Kwan, Nick Bultinck, Steven H. Simon, S.A. Parameswaran
    arXiv:2109.09749 | *Phys. Rev. Lett.* **128**, 156401 (2022)

10. **Beyond the Freshman's Dream: Classical fractal spin liquids from matrix cellular automata in three-dimensional lattice models**
    Sounak Biswas, Yves H. Kwan (co-first author), S. A. Parameswaran
    arXiv:2109.06207 | *Phys. Rev. B* **105**, 224410 (2022)

9. **One-Dimensional Luttinger Liquids in a Two-Dimensional Moiré Lattice**
    Pengjie Wang, Guo Yu, Yves H. Kwan (co-first author), Yanyu Jia, Shiming Lei, Sebastian Klemenz, F. Alexandre Cevallos, Trithep Devakul, Kenji Watanabe, Takashi Taniguchi, Shivaji L. Sondhi, Robert J. Cava, Leslie M. Schoop, Siddharth A. Parameswaran, Sanfeng Wu
    arXiv:2109.04637 | *Nature* **605**, 57-62 (2022)

8. †**Kekulé spiral order at all nonzero integer fillings in twisted bilayer graphene**
   Yves H. Kwan, Glenn Wagner, Tomohiro Soejima, Michael P. Zaletel, Steven H. Simon, Siddharth A. Parameswaran, Nick Bultinck
   arXiv:2105.05857 | *Phys. Rev. X* **11**, 041063 (2021)

7. **Quantum oscillations in the zeroth Landau Level and the serpentine Landau fan**
   T. Devakul, Yves H. Kwan, S. L. Sondhi, S. A. Parameswaran
   arXiv:2101.05294 | *Phys. Rev. Lett.* **127**, 116602 (2021)

6. **Theory of competing excitonic orders in insulating WTe_2 monolayers**
   Yves H. Kwan, T. Devakul, S. L. Sondhi, S. A. Parameswaran
   arXiv:2012.05255 | *Phys. Rev. B* **104**, 125133 (2021) (Editors' Suggestion)

5. †**Domain wall competition in the Chern insulating regime of twisted bilayer graphene**
   Yves H. Kwan, Glenn Wagner, Nilotpal Chakraborty, Steven H. Simon, S. A. Parameswaran
   arXiv:2007.07903 | *Phys. Rev. B* **104**, 115404 (2021)

4. †**Exciton band topology in spontaneous quantum anomalous Hall insulators: applications to twisted bilayer graphene**
   Yves H. Kwan, Yichen Hu, Steven H. Simon, S. A. Parameswaran
   arXiv:2003.11560 | *Phys. Rev. Lett.* **126**, 137601 (2021)

3. †**Excitonic fractional quantum Hall hierarchy in Moiré heterostructures**
   Yves H. Kwan, Yichen Hu, Steven H. Simon, S. A. Parameswaran
   arXiv:2003.11559 | *Phys. Rev. B* **105**, 235121 (2022)

2. **Quantum oscillations probe the Fermi surface topology of the nodal-line semimetal CaAgAs**
   Y. H. Kwan, P. Reiss, Y. Han, M. Bristow, D. Prabhakaran, D. Graf, A. McCollam, S. A. Parameswaran, A. I. Coldea
   arXiv:2001.02434 | *Phys. Rev. Research* **2**, 012055(R) (2020)

1. **Twisted bilayer graphene in a parallel magnetic field**

   Yves H. Kwan, S. A. Parameswaran, S. L. Sondhi

   arXiv:1910.04185 | *Phys. Rev. B* **101**, 205116 (2020)

Contents

Chapter 1

Introduction

Van der Waals (vdW) heterostructures form a class of materials that has generated considerable attention over the last decade [1, 2]. They comprise of 2D atomic crystals [3] that are stacked vertically and bound together by interlayer vdW forces. Direct mechanical assembly is currently the most common method of fabrication, whereby the constituent layers (produced e.g. by mechanical exfoliation) are manipulated by vdW forces and arranged into the desired configuration. Part of the allure of these systems arises from the myriad of combinations conceivable in this paradigm—possible choices of building blocks encompass semimetals (graphene), insulators (e.g. hexagonal boron nitride), semiconductors and metals (e.g. various transition metal dichalcogenides).

If the layers are stacked with a lattice or rotational mismatch, even richer possibilities arise due to the emergence of a long wavelength moiré pattern. The interplay of intralayer and interlayer interactions with this new lengthscale has consequently ushered in a new paradigm in condensed matter physics over the past few years. Coupled with the inherent tunability of 2D systems, these factors have contributed to the intense experimental and theoretical effort that has emerged to not only uncover the physical properties of these designer materials, but also explore the potential for device applications and novel functionalities.

The poster child of the moiré physics community is undoubtedly twisted bilayer graphene (TBG) in the 'magic angle' regime. The pioneering experiments on correlated electron behaviour in TBG by the Jarillo-Herrero group in 2018 [4, 5] triggered a flurry of research activity into its novel electronic properties, which continues unabated to this

day. This has also catalyzed investigations into related moiré heterostructures, notably other graphene-based materials and transitional metal dichalcogenide homobilayers and heterobilayers.

This thesis represents the author's contributions to the theoretical understanding of TBG, in particular its topological and correlated properties. In Section 1.1, we sketch an overview of TBG, primarily from the perspective of experiments. This is by no means an exhaustive survey, and is biased towards aspects that are relevant for later chapters. In Section 1.2, we provide an outline for the rest of this thesis.

1.1 Twisted bilayer graphene: a bird's eye view

Monolayer graphene is a semimetal with two Dirac points at charge neutrality at the Brillouin zone (BZ) corners [6]. When two monolayers are stacked with a relative twist angle θ, the microscopic lattice periodicity is disrupted, and a new larger lengthscale arises from the moiré beating phenomenon between the two layers. Assuming that the TBG system is still spatially periodic[1], the superlattice structure folds in the BZ and reconstructs the electronic band structure. It was recognized early on [7–10] that for smaller angles, the interlayer coupling leads to a downward renormalization of the Dirac velocity and a migration of the associated van Hove singularities (vHS) towards charge neutrality. This expectation was borne out by scanning tunneling microscopy/spectroscopy (STM/STS) on few-layer graphene samples [11–13]. At sufficiently small 'magic' twist angles around $\theta \sim 1.05°$, it was theoretically predicted that the central moiré bands (also called the flat bands), which span the electronic filling factors $-4 < \nu < 4$, would have a vanishing Dirac velocity and substantial band flattening [9]. This is exciting from the viewpoint of correlation physics because the quenching of kinetic energy is generally expected to promote the role of inter-electron interactions.

Indeed, the experimental discovery of proximate correlated insulating and superconducting phases in magic-angle TBG [4, 5] demonstrated the dramatic consequences of a small relative twist. The samples in these newer experiments were synthesized using a 'tear-and-stack' approach allowing for sub-degree twist precision, in contrast to earlier

[1]The distinction between commensurate and incommensurate twists will be discussed in Chapter 2.

studies which relied on largely uncontrolled techniques such as chemical vapour deposition or thermal decomposition of SiC. At $\nu = \pm 2$, transport and capacitance (dielectric loss) measurements detected electrical insulators with a resetting of the Hall densities upon doping these away from charge neutrality (CN) $\nu = 0$ [4]. Despite the integer filling per moiré unit cell, this insulating behaviour requires invoking correlation effects, since the superlattice band gaps are only at $|\nu| = 4$ upon accounting for spin and valley degeneracy. More striking was the appearance of superconducting domes that flank the correlated insulator at $\nu = -2$ [5], which generated a lot of excitement due to the resemblance to the phase diagram of the high-T_c cuprates. While the measured T_c in TBG was at most $\sim 2\,\mathrm{K}$, this is actually rather large in light of the tiny Fermi volume expected from general considerations of moiré band folding and empirically confirmed from quantum oscillations. The ratio T_c/T_F, where T_F is the Fermi temperature, significantly exceeds those of normal BCS superconductors, and is comparable to values seen in other strongly correlated families such as the cuprates, pnictides, and heavy fermion superconductors.

Hence many early interpretations centered around the hypothesis of a parent Mott insulator from which unconventional superconductivity descends. The connection to cuprate phenomenology was further strengthened by the finding of near-Planckian scattering rates and linear-in-T resistivity down to the milli-Kelvin scale [14–17], possibly indicative of a strange metal regime. In addition, STM spectroscopy has revealed evidence of a 'V'-shaped gap and nodal superconductivity [18], with related signatures in the closely related twisted trilayer graphene (TTG) [19]. There is also evidence for nematicity within the superconducting dome [20, 21].

Despite these similarities, TBG presents a fundamentally distinct arena to explore strongly correlated physics. From a practical standpoint, the two-dimensional and engineering nature of TBG devices confers them with many advantages (and some drawbacks) compared with their crystalline counterparts. For example, hydrostatic pressure can be easily applied, which increases the interlayer hopping and therefore the effective magic angle [22]. The graphene sheets are typically sandwiched between hexagonal boron nitride (hBN) substrate slabs, separating them from the metallic gates. Changing the thickness of this spacer controls the screening of the long-range part of the Coulomb interaction.

This has been successfully exploited to examine the interplay between insulating and superconducting orders by tuning the interaction strength [23–25]

The most significant experimental knob in TBG has to do with its gate tunability. Owing to the tiny area of the reconstructed moiré Brillouin zone (mBZ), it is possible to dope through *entire* electronic bands *in situ*, including into the remote bands $|\nu| > 4$, just by adjusting the gate voltages. This sidesteps having to fabricate multiple samples and dope using chemical substitution or impurities, which would unavoidably introduce disorder and hinder the formation of delicate correlated orders. The transport data of Ref. [26] provided the first demonstration that a single device could exhibit correlated insulators and superconducting domes around all integer fillings within the central band manifold, and not just at $|\nu| = 2$.

Even for samples and conditions where such ordered states are absent, there is still an incontrovertible body of evidence in favour of symmetry-breaking and correlation effects throughout the flat-band regime. Landau fans track the field-dependent densities where the longitudinal magnetoresistivity reaches its minimum due to filled Landau levels (LLs), and yield valuable information on the Fermi surface degeneracies. They are commonly found to emanate from fillings $|\nu| = 0, 2, 3$ with corresponding degeneracies $4, 2, 1$ [4, 5, 22–24, 26–33]. This necessitates the presence of carrier density resetting and flavour polarization since spin/valley degeneracy would imply Landau fan degeneracies of a multiple of 4. Compressibility probes [16, 29, 31, 34–37] give a complementary perspective by measuring the chemical potential $\mu(\nu)$ as a function of density. They find a characteristic sawtooth pattern in $\frac{d\mu}{dn}$ with dips (sometimes strong enough to lead to negative compressibility) near each integer filling. For single-gated devices, STM experiments [38–40] also detect distinct changes in the excitation spectrum for integer ν. The overall consensus is that of 'cascade physics', referring to the sequence of density-tuned flavour transitions which repeats roughly each time ν is increased by one. Crucially, this phenomenology continues to hold at elevated temperatures far above the Kelvin scale of the correlated insulators and superconductors. The notion of non-trivial correlations at higher temperatures is corroborated by signatures of Pomeranchuk physics around $|\nu| = 1$ [31, 34].

The tunability of TBG is accompanied with an even larger variability in observed

phenomena, which presents significant challenges when confronting experiments. Even basic questions such as the existence of correlated insulators and superconductors find contrasting answers in seemingly similar samples, pointing to the presence of confounding variables that are not easily detected or adjusted. The twist angle is an important parameter that an experimentalist would ideally be able to control to tune in and out of the flat band regime. However, samples are vulnerable to twist angle disorder [30] which is believed to have a substantial impact on the correlation phenomena but is difficult to treat theoretically. In a similar vein, scanning probes have shown that unintentional strain is ubiquitous across devices [38, 41–43]. These variations pose obstacles in the search for a unifying perspective of TBG.

The Dirac cones of the underlying graphene layers qualitatively influence the nature of the physics in TBG. Studying Hubbard-like models is a common route to gaining insight into strongly correlated materials. However as recognized in early theoretical works, applying this to TBG is complicated by the fragile topology carried by the central bands [44–46], whose extended Wannier orbitals have been dubbed 'fidget spinners' due to their shape. While real-space approaches in the extended Hubbard model have seen theoretical successes, these issues suggest that another paradigm may be more appropriate.

If the graphene layers are suitably aligned with the encapsulating hBN substrate, the Dirac points in the mBZ become gapped, imbuing TBG with strong topology in the form of nontrivial valley Chern numbers. If interactions are strong enough to spontaneously break time-reversal symmetry (TRS), this raises the possibility of forming a spontaneous Chern insulator. Indeed, this was experimentally realized and characterized through the observation of the quantized anomalous Hall (QAH[2]) effect at $\nu = +3$ in zero magnetic field [28][3]. The presence of narrow Chern bands and strong interactions points to the relevance of quantum Hall-like physics, the other paradigmatic setting for strong correlations.

The connection to quantum Hall persists even when there is no substrate align-

[2]In this thesis, we will use 'QAH' to refer to either the transport effect, the quantum state that gives rise to it, and/or the associated electronic phase. The meaning should be clear from the context. Similar comments apply for other correlated states such as the IKS and the KIVC.

[3]Ref. [27] earlier reported an non-quantized anomalous Hall effect.

ment [47], and is strengthened in the presence of a perpendicular magnetic field B. At small B well below the Hofstadter regime, numerous Chern insulators at different fillings are stabilized, which cross over to a rich array of Hofstadter ferromagnets at larger fields [16, 32, 33, 37, 39, 48–51]. There has also been recent evidence of fractional Chern insulators that remain competitive for low fields [52].

1.2 Thesis outline

Chapter 2 covers the theoretical background required for the rest of this thesis. We first give a self-contained review of the Bistrizter-Macdonald (BM) model for the non-interacting band structure, which forms the backbone of much of the analytical and numerical results in this field. We also explain some general features of moiré physics. We then present a brief summary of the so-called strong coupling[4] framework for correlations in TBG. This is predicated on a hierarchy of scales, where the dominant contribution is the part of the Coulomb interaction that respects a hidden $U(4) \times U(4)$ symmetry. This program fully embraces the quantum Hall viewpoint, and predicts a set of insulating 'generalized ferromagnets' at integer ν. A brief recap of Hartree-Fock (HF) theory and its implementation for TBG is included for completeness.

The main body of this thesis is divided into Parts I and II. In Part I, we build upon previous theoretical work on the strong coupling insulators. We study various aspects of their neutral and charged excitations, with an emphasis on seeking out novel phenomena enabled by the coexistence of strong correlations and topology in this system.

The experimental detection of a spontaneous QAH at filling factor $\nu = +3$ was the first clear piece of evidence supporting the topological nature of TBG [28]. In Chapter 3, we theoretically study the excitons of the QAH insulator, focusing on the possibility of nontrivial exciton topology inherited from the underlying electron bands which host different Chern numbers $C = \pm 1$ [53]. This idea is inspired from a toy model of LLs in opposite magnetic fields, which yields exactly flat topological exciton bands. In a realistic

[4]This is not to be confused with the usual sense of strong coupling in the cuprates, which typically refers to physics about the Mott insulating limit. We will use the terms 'strong coupling insulators' and 'generalized ferromagnets' interchangeably when referring to the correlated states predicted by the strong coupling approach to TBG.

model for interacting TBG, we indeed find the presence of topological intervalley excitons with suppressed dispersion. Based on this setting of flat-band topological bosons, we consider the intriguing possibility of a novel fractional excitonic quantum Hall hierarchy [54]. Members of the hierarchy curiously share the same quantized charge Hall effect but differ in valley and thermal responses.

Apart from excitons, domain walls represent another class of neutral excitations in the QAH [55]. However, as we discuss in Chapter 4, the domain wall structure is more complicated than the usual examples of quantum Hall ferromagnetism (QHFM), since domains in TBG have freedom in both the choice of Chern number $C = \pm 1$ and valley polarization. We show that domain edge modes can either be counter-propagating or co-propagating, with significant consequences on the robustness of the QAH effect. By developing a numerical framework to treat spatially inhomogeneous perturbations in the BM model, we validate an effective field theory for domain walls and show that the energetic competition between the different types is subtle and varies as a function of twist angle and degree of substrate alignment.

In terms of charged excitations, spin skyrmions are natural candidates in the QAH given the close connections to QHFM. However the possibility of charged flavour textures also extends to strong coupling insulators at other fillings. In particular, paired pseudospin skyrmions have been predicted to form at even integer fillings, and are key ingredients behind a recently proposed theory of purely electronically mediated skyrmion superconductivity [56]. Such objects have been analyzed in the quantum Hall limit using a sigma model description, but have never been constructed in a realistic TBG model. In Chapter 5, we discuss our results for obtaining skyrmionic excitations for both the QAH at $\nu = 3$ (spin) and the so-called Kramers intervalley coherent (KIVC) ground state at $\nu = 0, \pm 2$ (pseudospin) in the interacting BM model [57]. We confirm the paired nature of skyrmions at even integer filling, and compute the effective masses which are relevant for understanding T_c.

In Part II, we switch gears and return to the fundamental question of what the normal state in experimental TBG is. In Chapter 6, we critically assess the strengths and weaknesses of the strong coupling framework when compared to experimental findings, and propose strain as an experimentally motivated perturbation that can help bridge the gaps

between theory and experiment [58]. In particular, our comprehensive mean-field studies show that a small value of strain is capable of stabilizing an incommensurate Kekulé spiral (IKS) order over a large range of fillings within the central band subspace [59]. We demonstrate that strain and the IKS are ingredients that can and should form part of any consistent umbrella theory for the correlated physics in TBG.

Chapter 2

Theoretical Background

In this chapter, we review the necessary theoretical ideas and tools that underpin the physics in the subsequent chapters. In Sec. 2.1, we set the scene and establish notational conventions by discussing the geometry and the various symmetries of graphene and its twisted bilayer. In Sec. 2.2, we outline a derivation of the continuum model which is an oft-used approximation of the non-interacting band structure. In Sec. 2.3, we introduce interactions and give a recap of HF and its implementation in TBG. Finally in Sec. 2.4, we summarize the strong coupling framework of interacting TBG, a popular approach to understanding the correlated insulators that draws heavily from quantum Hall intuition.

2.1 Graphene

2.1.1 Monolayer

Graphene consists of carbon atoms on the sites of the honeycomb lattice, which are subdivided into A and B sublattices (Fig. 2.1a) with intra-unit-cell coordinates $\tau_{\mathrm{A}}, \tau_{\mathrm{B}}$. Each carbon forms three σ-bonds using the sp^2 hybridized orbitals, while the remaining 2p-orbitals form π-bands which are intrinsically half-filled [6]. The dispersion of these π-bands, shown in Fig. 2.1c, can be calculated in a nearest neighbour tight-binding approximation to be

$$E(\boldsymbol{k}) = \pm t|f(\boldsymbol{k})|, \quad f(\boldsymbol{k}) = e^{\frac{ik_y a}{2}}\left(2\cos\frac{\sqrt{3}k_x a}{2} + e^{-\frac{3ik_y a}{2}}\right) \tag{2.1}$$

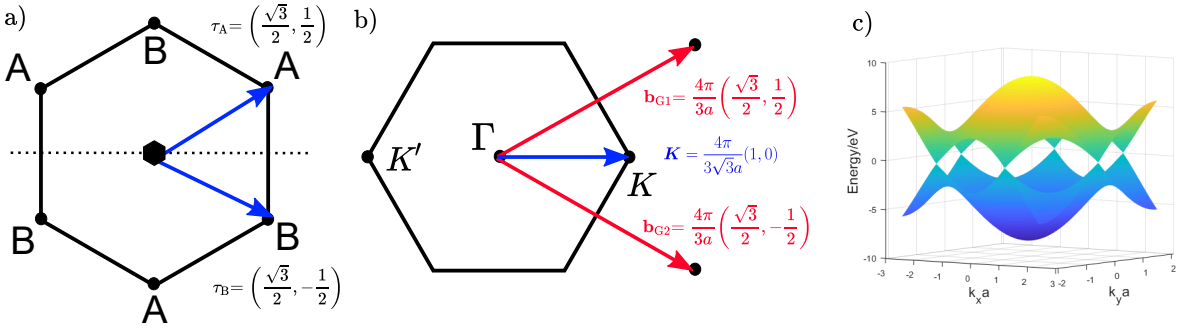

Figure 2.1: a) Real-space repeating hexagonal cell in graphene with the two sublattices labelled. Symmetry elements are also indicated. b) Graphene BZ showing the inequivalent Dirac points K, K' and the reciprocal lattice vectors $\boldsymbol{b}_{G1}, \boldsymbol{b}_{G2}$. c) Tight-binding dispersion of graphene.

where $t \simeq 2.8\,\text{eV}$ is the hopping amplitude and $a \simeq 1.42\,\text{Å}$ is the C-C bond length. At charge neutrality, this band structure hosts linear band crossing points at the two inequivalent corners of the BZ. The Hamiltonian near these two valleys (K and $K' = -K$) can be expressed as 2D analogues of the relativistic Dirac equation[1]

$$H_\tau(\boldsymbol{p}) = \frac{3ta}{2}(\tau p_x \sigma_x - p_y \sigma_y) = v_F(\tau p_x \sigma_x - p_y \sigma_y), \tag{2.2}$$

where $\tau = \pm 1$ is a valley index indicating $\pm K$, $v_F \simeq 9 \times 10^5\,\text{ms}^{-1}$ is the bare Fermi velocity, and the Pauli matrices σ act in sublattice space. At low energies in the absence of atomic-scale disorder, valley is good quantum number, and so we often speak of four flavours of fermions (including the spin degree of freedom). Spin-orbit coupling is negligible in the π-bands [60], so we will omit spin when discussing the non-interacting band structure[2]. The point group is D_{6h} which is fully realized at the hexagon centres.

2.1.2 Untwisted bilayer

Before diving into TBG, it is worth quickly summarizing what happens in untwisted bilayer graphene. The main stacking arrangements are AA-stacking where the all the carbon atoms on the two layers lie directly on top of each other, and AB-stacking (Bernal) where one layer is translated by $\boldsymbol{\tau}_B - \boldsymbol{\tau}_A$ (see Figure 2.1a) such that half of the carbons lie

[1] In this section and the next, we use the convention that $\boldsymbol{k}$ denotes an absolute momentum, while $\boldsymbol{p}$ refers to a momentum measured with respect to some special point such as the (moiré) BZ corner.

[2] For the case of graphene, the presence of inversion and time-reversal symmetry means that the bands are not spin-split anyway.

on the hexagon centres of the other layer. It turns out that AB-stacking is more common because it has a greater vdW binding energy [61]. The low-energy band structure of Bernal-stacked bilayer graphene consists of gapless quadratically dispersing fermions at the BZ corners [62].

2.1.3 Twisted bilayer

Consider the following procedure for specifying a twist configuration in TBG. Begin with AA-stacked bilayer graphene with interlayer spacing $c_0 = 3.35\,\text{Å}$. Without loss of generality layers 1 and 2 are placed at $z = \pm c_0/2$, and rotated by $\pm\theta/2$ about a hexagon centre. Finally, layer 1 (the top layer) is translated by an in-plane displacement $\boldsymbol{d}$. With the appropriate choice of θ and $\boldsymbol{d}$, this is capable of representing any arbitrary stacking configuration with fixed interlayer spacing. Two key issues need to be addressed before proceeding further: commensurability and symmetries [44].

The spatial motifs of the two layers interfere, causing the formation of a moiré pattern [63]. Generic twist angles are incommensurate and lead to quasiperiodicity. Strictly speaking, Bloch's theorem ceases to hold and it is therefore inappropriate to speak of energy bands. The condition for a commensurate and periodic superlattice is the following. Let $\boldsymbol{a}_{\text{G}i}$ be the unrotated monolayer primitive lattice vectors, and R_θ be a rotation matrix about the stacking axis. If there exists integers m_i, n_i such that $m_1 R_{\theta/2}\boldsymbol{a}_{\text{G}1} + m_2 R_{\theta/2}\boldsymbol{a}_{\text{G}2} = n_1 R_{-\theta/2}\boldsymbol{a}_{\text{G}1} + n_2 R_{-\theta/2}\boldsymbol{a}_{\text{G}2}$, then the system has discrete translation invariance [64]. The full solution set of commensurate angles can be indexed by two integers. Note that the statement of commensurability only depends on θ and not the interlayer shift $\boldsymbol{d}$. From an experimental standpoint, such considerations are largely irrelevant—it is impossible to determine whether a given sample has a commensurate twist, let alone deliberately fabricate a device with exact twist precision. In any case, experiments deal with systems of finite size. From the theory side, it is helpful to be able to leverage the machinery of Bloch's theorem and think in terms of crystal momenta. Therefore some of the literature focuses on commensurate angles where a microscopic starting point can be taken, for example the large unit cell tight-binding models considered in Refs [65, 66]. A disadvantage of such an approach is that increasingly bulky

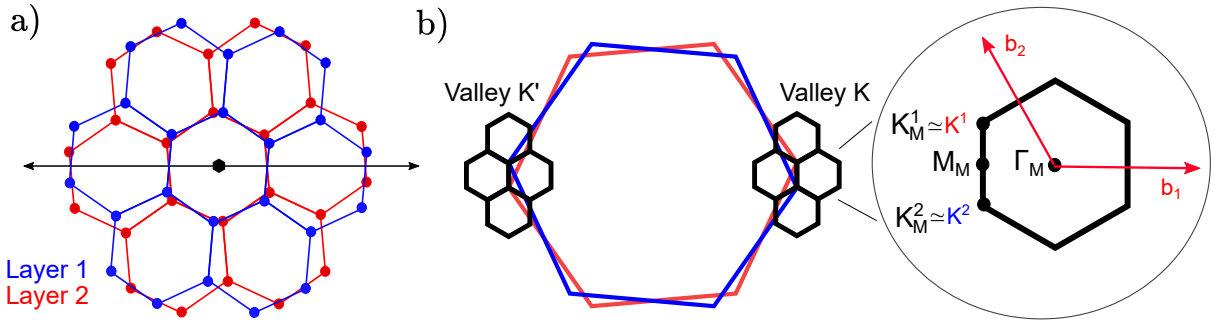

Figure 2.2: a) Real-space schematic of TBG with $\theta = 5°$ and $\boldsymbol{d} = \boldsymbol{0}$. The symmetry elements $\hat{C}_{6v}$ and $\hat{C}_{2x}$ are indicated. b) Extended zone scheme of the BZ showing how the mBZ at each valley is formed from the rotated monolayer BZ's. Circle zooms into the mBZ showing the high-symmetry momenta and the moiré reciprocal lattice vectors $\boldsymbol{b}_i$.

and unwieldy Hamiltonians are required to better approximate a fixed twist angle. The problem of restricting to commensurate approximants is sidestepped in the continuum model [9], which manages to generate a periodic Hamiltonian for any θ. At the expense of full microscopic rigour, the phenomenological continuum model is more amenable to analytical and numerical treatment.

The finite-order symmetries of TBG depend on both θ and $\boldsymbol{d}$. For an arbitrary stacking of two graphene layers, the only guaranteed symmetry is (spinless) time-reversal symmetry (TRS) denoted by $\hat{\mathcal{T}}$. For $\boldsymbol{d} = \boldsymbol{0}$, the maximal subset of monolayer symmetries is preserved (Fig. 2.2a). The symmetry generators are TRS ($\hat{\mathcal{T}}$), sixfold rotation about the z-axis ($\hat{C}_{6z}$), and twofold rotation about the x-axis[3] ($\hat{C}_{2x}$). The corresponding point group is D_6. For large twist angles, qualitative details of the band structure, such as the existence of Dirac points at charge neutrality, can depend on the symmetry group [64]. However for small twists near the magic angle regime, it is argued that such differences are invisible at experimentally resolvable energy scales, and the description in terms of D_6 symmetry is the most appropriate [44]. This is effectively captured by the continuum model since its spectrum is independent of $\boldsymbol{d}$ [9]. At small angles, intervalley hybridization is weak because a high order of interlayer hopping is required to connect the two monolayer valleys. Therefore in addition to charge conservation $U_C(1)$, an approximate $U_V(1)$ valley conservation law emerges at low energies. In fact, this is promoted to an exact $U_V(1)$ in the continuum model, leading to a total internal symmetry $SU(2)_K \times SU(2)_{K'}$ when spin

[3]This is often referred to as a 'mirror' symmetry $\hat{M}$ in the literature.

is included.

2.2 Bistritzer-Macdonald model

2.2.1 Derivation

The continuum model [9] (often referred to as the Bistritzer-MacDonald (BM) model) is a widely used approximation to the band structure of TBG. In this section, we provide a clean and direct derivation to demonstrate the simplicity of the approach and highlight where the approximations enter. The general premise is that in the low-energy limit, we can focus on momenta near one of the valleys (say valley K) and think of four species of fermions (two layers $\times$ two sublattices). Recall that we assume $\boldsymbol{d} = 0$ and that the layers are twisted by $\pm\theta/2$. The intralayer physics is simple and modelled by twisted versions of the Dirac cones of (2.2). The interlayer coupling leads to a spatially-modulating hopping amplitude between the layers, whose functional form is to be determined below.

We work in the basis of plane waves: for an electron residing in layer $l = 1, 2$ and sublattice $\sigma = \mathrm{A}, \mathrm{B}$, we define the Bloch states

$$|\boldsymbol{k}, l\sigma\rangle \equiv \left|\boldsymbol{K}^l + \boldsymbol{p}, l\sigma\right\rangle = \frac{1}{\sqrt{N}} \sum_{\boldsymbol{R}} e^{i\boldsymbol{k}\cdot(\boldsymbol{R}^l + \boldsymbol{\tau}_\sigma^l)} \left|\boldsymbol{R}^l, l\sigma\right\rangle \tag{2.3}$$

where $\boldsymbol{R}$ is an untwisted monolayer lattice vector, the superscript $l = 1, 2$ on a vector denotes rotation by $R_{\pm\theta/2}$, and the $\boldsymbol{\tau}_\sigma$ are the intra-unit-cell coordinates introduced in Fig. 2.1a. Therefore $\boldsymbol{K}^l$ correctly identifies the new positions of valley K in each layer. Consider the following interlayer matrix element

$$T^{\sigma,\sigma'}_{\boldsymbol{k},\boldsymbol{k}'} = \langle \boldsymbol{k}, 1\sigma | \, H_{\mathrm{BM}} \, | \boldsymbol{k}', 2\sigma' \rangle \tag{2.4}$$

which corresponds to an electron on sublattice σ' on the bottom layer with momentum

$\boldsymbol{k}'$ hopping to sublattice σ on the top layer with momentum $\boldsymbol{k}$. Now compute

$$\begin{aligned} T^{\sigma,\sigma'}_{\boldsymbol{k},\boldsymbol{k}'} &= \frac{1}{N}\sum_{\boldsymbol{R},\boldsymbol{R}'} e^{-i\boldsymbol{k}\cdot(\boldsymbol{R}^1+\boldsymbol{\tau}^1_\sigma)+i\boldsymbol{k}'\cdot(\boldsymbol{R}'^2+\boldsymbol{\tau}^2_{\sigma'})} \left\langle \boldsymbol{R}^1, 1\sigma \right| H_{\mathrm{BM}} \left| \boldsymbol{R}'^2, 2\sigma' \right\rangle \\ &= \frac{1}{N}\sum_{\boldsymbol{R},\boldsymbol{R}'} e^{-i\boldsymbol{k}\cdot(\boldsymbol{R}^1+\boldsymbol{\tau}^1_\sigma)+i\boldsymbol{k}'\cdot(\boldsymbol{R}'^2+\boldsymbol{\tau}^2_{\sigma'})} t(\boldsymbol{R}^1 - \boldsymbol{R}'^2 + \boldsymbol{\tau}^1_\sigma - \boldsymbol{\tau}^2_{\sigma'}) \\ &= \frac{1}{N^2 A_{\mathrm{UC}}}\sum_{\boldsymbol{R},\boldsymbol{R}'}\sum_{\boldsymbol{q}} e^{i(\boldsymbol{q}-\boldsymbol{k})\cdot\boldsymbol{R}^1+i(\boldsymbol{k}'-\boldsymbol{q})\cdot\boldsymbol{R}'^2} e^{i(\boldsymbol{q}-\boldsymbol{k})\cdot\boldsymbol{\tau}^1_\sigma} e^{i(\boldsymbol{k}'-\boldsymbol{q})\cdot\boldsymbol{\tau}^2_{\sigma'}} t(\boldsymbol{q}) \\ &= \sum_{\boldsymbol{G},\boldsymbol{G}'} \frac{t(\boldsymbol{k}+\boldsymbol{G}^1)}{A_{\mathrm{UC}}} e^{i(\boldsymbol{G}\cdot\boldsymbol{\tau}_\sigma - \boldsymbol{G}'\cdot\boldsymbol{\tau}_{\boldsymbol{\sigma}'})} \delta_{\boldsymbol{k}+\boldsymbol{G}^1,\boldsymbol{k}'+\boldsymbol{G}'^2}. \end{aligned} \tag{2.5}$$

In the second line, we introduced the interlayer hopping matrix element $t(\boldsymbol{r})$ which depends only on the distance between the sites (two-centre approximation). In the third line, we inserted the Fourier transform of the hopping element $t(\boldsymbol{r}) = \frac{1}{NA_{\mathrm{UC}}}\sum_{\boldsymbol{q}} t(\boldsymbol{q}) e^{i\boldsymbol{q}\cdot\boldsymbol{r}}$ where A_{UC} is the area of the unit cell. In the fourth line, the sum over lattice sites is used to enforce $\boldsymbol{q} = \boldsymbol{k} + \boldsymbol{G}^1 = \boldsymbol{k}' + \boldsymbol{G}'^2$ for some $\boldsymbol{G}, \boldsymbol{G}'$ (in-plane Bragg scattering) belonging to the unrotated monolayer reciprocal lattice.

At this stage, no additional approximations have been made. Now we exploit the fact that we are interested in momenta close to the monolayer Dirac points, so $|\boldsymbol{k} - \boldsymbol{K}^1|, |\boldsymbol{k}' - \boldsymbol{K}^2| \ll |\boldsymbol{K}|$. Since the the orbital overlap is smooth as a function of inter-orbital distance, the hopping element $t(\boldsymbol{q})$ is expected to fall rapidly with $|\boldsymbol{q}|$. Therefore in the sum over $\boldsymbol{G}$ in the last line of (2.5), we only keep the terms $\boldsymbol{G} = \boldsymbol{0}, -\boldsymbol{b}_{\mathrm{G}1}, -\boldsymbol{b}_{\mathrm{G}2}$, where the $\boldsymbol{b}_{\mathrm{G}i}$ are the monolayer reciprocal lattice vectors shown in Fig. 2.1b. These are the three terms for which $t(\boldsymbol{k}+\boldsymbol{G}^1)$ has the smallest argument—effectively we have kept the lowest harmonic of the moiré potential (dominant harmonic approximation). Its value is approximated as $t(|\boldsymbol{K}|)$. The delta function constrains $\boldsymbol{G}'$ to take the same three reciprocal lattice vectors if we demand that $|\boldsymbol{k}' - \boldsymbol{K}^2|$ remains small.

Aggregating these observations and performing some straightforward algebra, we ob-

tain the following description of the continuum model

$$\langle \boldsymbol{k}, 1| H_{\mathrm{BM}} |\boldsymbol{k}', 1\rangle = \hbar v_F \boldsymbol{\sigma}^*_{\theta/2} \cdot (\boldsymbol{k} - \boldsymbol{K}^1)\, \delta_{\boldsymbol{k},\boldsymbol{k}'} \tag{2.6}$$

$$\langle \boldsymbol{k}, 2| H_{\mathrm{BM}} |\boldsymbol{k}', 2\rangle = \hbar v_F \boldsymbol{\sigma}^*_{-\theta/2} \cdot (\boldsymbol{k} - \boldsymbol{K}^2)\, \delta_{\boldsymbol{k},\boldsymbol{k}'} \tag{2.7}$$

$$\langle \boldsymbol{k}, 1| H_{\mathrm{BM}} |\boldsymbol{k}', 2\rangle = T_1 \delta_{\boldsymbol{k}-\boldsymbol{k}',\boldsymbol{0}} + T_2 \delta_{\boldsymbol{k}-\boldsymbol{k}',\boldsymbol{b}_1+\boldsymbol{b}_2} + T_3 \delta_{\boldsymbol{k}-\boldsymbol{k}',\boldsymbol{b}_2} \tag{2.8}$$

$$\boldsymbol{\sigma}^*_{\theta/2} = e^{-(i\theta/4)\sigma_z} (\sigma_x, \sigma_y^*) e^{(i\theta/4)\sigma_z} \tag{2.9}$$

$$T_1 = \begin{pmatrix} w_{AA} & w_{AB} \\ w_{AB} & w_{AA} \end{pmatrix} \tag{2.10}$$

$$T_2 = \begin{pmatrix} w_{AA} & w_{AB} e^{i\phi} \\ w_{AB} e^{-i\phi} & w_{AA} \end{pmatrix} \tag{2.11}$$

$$T_3 = \begin{pmatrix} w_{AA} & w_{AB} e^{-i\phi} \\ w_{AB} e^{i\phi} & w_{AA} \end{pmatrix} \tag{2.12}$$

$$\phi = \frac{2\pi}{3}. \tag{2.13}$$

Some comments to help decipher the above equations:

1. The sublattice degree of freedom has been absorbed into the matrix structure.

2. The intralayer kinetic terms pick up a twist (2.9) due to the rotation of the layers. If we neglect this Pauli twist, which works well in the small-angle limit, the model gains an exact particle-hole symmetry (PHS).

3. In the interlayer hopping terms, we have defined the moiré reciprocal lattice vectors (RLVs) $\boldsymbol{b}_i$ in the mBZ (Fig. 2.2)

$$\begin{aligned} \boldsymbol{b}_1 &= (R_{\theta/2} - R_{-\theta/2})(\boldsymbol{b}_{\mathrm{G}2} - \boldsymbol{b}_{\mathrm{G}1}) = \sqrt{3} k_\theta (1, 0) \\ \boldsymbol{b}_2 &= (R_{\theta/2} - R_{-\theta/2}) \boldsymbol{b}_{\mathrm{G}2} = \sqrt{3} k_\theta (-\frac{1}{2}, \frac{\sqrt{3}}{2}), \end{aligned} \tag{2.14}$$

   where $k_\theta = 2k_D \sin\theta/2$ is the moiré wavevector and $k_D = 4\pi/3\sqrt{3}a$ is the monolayer Dirac momentum.

4. There are now two interlayer hopping strengths w_{AA} and w_{AB}, while we initially we had a single interlayer hopping amplitude $t(|\boldsymbol{K}|)$. This generalization is allowed

by the symmetries. We always take $w_{\mathrm{AB}} = 110\,\mathrm{meV}$.

5. H_{BM} is an infinite-dimensional matrix in the momentum basis, similar to the situation in the nearly free electron model. To solve the for energies numerically, we impose a plane wave cutoff that preserves the point group symmetries, typically keeping states with $|\boldsymbol{k} - \boldsymbol{K}| < 7k_\theta$ and checking for convergence.

6. The expressions for valley K' can be deduced using TRS.

2.2.2 Emergent moiré periodicity

Because the terms in (2.8) only allow momentum changes by integer combinations of $\boldsymbol{b}_1$ and $\boldsymbol{b}_2$, the resulting theory is periodic. Inspection of the new RLVs (2.14) reveals that the new mBZ is the monolayer BZ rotated by 90° and shrunk by the moiré scale factor $2\sin(\theta/2)$. Therefore, the real-space superlattice is similarly rotated and expanded by $1/(2\sin(\theta/2))$—a good rule of thumb is that the moiré lattice constant is $a_{\mathrm{M}} \simeq 14\,\mathrm{nm}$. By taking the inverse Fourier transform of (2.8), we can interpret the continuum model as Dirac fermions on two layers with an interlayer hopping that is local and spatially modulated with wavevector $\sim k_\theta$.

How did a periodic Hamiltonian emerge from generically incommensurate twist angles? There are two closely related reasons for this. First, we constrained the sum in (2.5) to $\boldsymbol{G} = \boldsymbol{G}'$ with the rationale that a violation of this condition involves a state with a large kinetic energy. However nothing strictly forbids us from picking say $\boldsymbol{G} = \boldsymbol{b}_{\mathrm{G}1}, \boldsymbol{G}' = \boldsymbol{0}$. Second, the intralayer physics is modelled by Dirac terms, which is a good approximation when $|\boldsymbol{k} - \boldsymbol{K}|a \ll 1$ (hence the "continuum" designation). The full monolayer physics would have allowed purely in-plane Bragg scattering by integer combinations of $\boldsymbol{b}^l_{\mathrm{G}j}$. Both processes take us out of the original plane wave cutoff given roughly by the clumps of mBZ hexagons in Fig. 2.2b. Now in general, $\boldsymbol{b}^l_{\mathrm{G}j}$ may not be expressible as an integer sum of the $\boldsymbol{b}_j$. In this case, the incommensurability is evident if an electron is Bragg-scattered by say $-\boldsymbol{b}^1_{\mathrm{G}1}$, and subsequently hops back to within the plane wave cutoff through a sequence of $\boldsymbol{b}_j$ hops, but this is exponentially suppressed at small θ due the high order of perturbation theory required[4].

[4]This also explains the emergent $U_V(1)$ valley conservation symmetry.

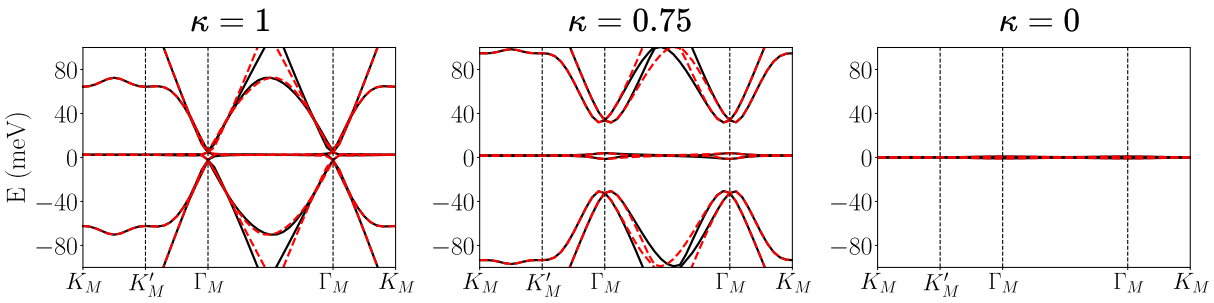

Figure 2.3: Band structure of the BM model along a cut in the mBZ for different values of the chiral ratio $\kappa = w_{\mathrm{AA}}/w_{\mathrm{AB}}$. The twist angle is held constant at the magic angle appropriate for the chiral limit $\kappa = 0$ ($\theta \simeq 1.06°$). Black (red) lines denote valley K (K').

2.2.3 Chiral ratio

Figure 2.3 plots the band structure of the BM model, focusing on the low-energy bands closest to neutrality. For the 'isotropic' limit $w_{\mathrm{AA}} = w_{\mathrm{AB}}$ originally considered by Bistritzer and MacDonald [9], it was found that the Dirac points were left intact and remained at CN[5]. Reduction of the twist angle suppressed the renormalized Dirac velocity v_F^* and flattened the central eight bands (including spin and valley). At the magic angle[6] of $\theta \simeq 1.05°$, v_F^* vanished, but the central two bands were not energetically isolated from neighbouring remote bands, in contrast to experiments which strongly suggested single-particle band gaps of the order of tens of meV [4]. This conundrum is resolved by taking into account lattice relaxation and corrugation effects [70, 71]. In TBG, we can identify regions that locally look like AA and AB-stacking. Recall that in bilayer graphene, AB-stacking is energetically more favourable than AA-stacking. Therefore in TBG, the AB regions expand at the expense of AA regions, which buckle out of plane slightly. In terms of the interlayer hoppings, this leads to $w_{\mathrm{AA}} < w_{\mathrm{AB}}$. This cleanly isolates the central bands from higher-energy states. The real-space weight of the central

[5] $\hat{C}_{2z}\hat{\mathcal{T}}$ quantizes the Berry phase of an arbitrary loop in momentum space to 0 or π, depending on if it encloses an even or odd number of Dirac points. This is a $\mathbb{Z}_2$ topological invariant which prevents the Dirac points from gapping out individually [67]. In fact, a stronger condition holds as long as the central pair of bands remain energetically isolated. For a two-band model there exists a $\mathbb{Z}$ winding number, which takes the same value for the two Dirac points in a single valley of TBG. Therefore they cannot annihilate without interference from remote bands [46, 67–69] or breaking of $U(1)_V$. In addition, the Dirac points are pinned at the mBZ corners due to $\hat{C}_{3z}$ symmetry—the degenerate states form a doublet under the D_3 symmetry group relevant for a single valley.

[6] Note that generally there is no unique definition for the magic angle. For example one could have defined it as the angle for which the central bands have the minimal bandwidth. In any case, its precise value depends on parameters, and what is important is that the band structure is such that interactions play a dominant role.

band wavefunctions is concentrated around the AA regions.

We define a key dimensionless parameter, the chiral ratio $\kappa = w_{\mathrm{AA}}/w_{\mathrm{AB}}$. Its precise value in experiments is debatable, but is expected to lie in the range $0.5 < \kappa < 0.8$ [70–73]. Interactions have been argued to renormalize this down further [74]. In Ref [75], this was taken to the extreme by setting $\kappa = 0$. In this so-called chiral limit, the model acquires a particle-hole symmetric spectrum due to the chiral symmetry $\{\hat{H}_{\mathrm{BM}}, \sigma_z\} = 0$. This can be thought of as an idealized version of realistic TBG: the central bands become degenerate, exactly flat, and energetically isolated across the entire mBZ at the magic angle. In addition, the Berry curvature and quantum geometry becomes maximally LL-like [76].

2.3 Interacting model

2.3.1 Form factors

Bloch eigenstates of the single-particle BM Hamiltonian in (2.6)–(2.13) are parameterized as

$$|\psi_{\tau,a}(\boldsymbol{k})\rangle = \sum_{\boldsymbol{G}I} u_{\boldsymbol{G}\tau a I}(\boldsymbol{k})\, |\boldsymbol{k}+\boldsymbol{G}, \tau, I\rangle \tag{2.15}$$

where a is a band label, I is a composite index for layer l and sublattice σ, $\boldsymbol{G}$ is a moiré RLV, and $\boldsymbol{k}$ is a momentum that lives in the mBZ. The associated creation operator is $\hat{c}^\dagger_{\tau a}(\boldsymbol{k})$. The ket on the RHS is a plane wave state with momentum $\boldsymbol{k}+\boldsymbol{G}$ measured with respect to an arbitrary basepoint[7] which maps onto Γ_{M} in valley τ. The Bloch functions are defined to be periodic in the mBZ, so the cell-periodic u's are *not* periodic in its momentum argument. In particular, we have

$$|u_{\tau,a}(\boldsymbol{k}+\boldsymbol{G})\rangle = e^{-i\boldsymbol{G}\hat{\boldsymbol{r}}}\, |u_{\tau,a}(\boldsymbol{k})\rangle\,. \tag{2.16}$$

We define the continuum model form factors [77]

$$\lambda_{\tau,ab}(\boldsymbol{k},\boldsymbol{q}) = \langle u_{\tau,a}(\boldsymbol{k})|u_{\tau,b}(\boldsymbol{k}+\boldsymbol{q})\rangle = \lambda^*_{\tau,ba}(\boldsymbol{k}+\boldsymbol{q},-\boldsymbol{q}), \tag{2.17}$$

[7] For convenience, the basepoints in the two valleys are chosen to be time-reversal related.

where $\boldsymbol{k}$ is a mBZ momentum, but $\boldsymbol{q}$ runs over all (intravalley) momenta. This is an important quantity since it determines the flavour-diagonal densities

$$\hat{\rho}_{\tau s}(\boldsymbol{q}) = \sum_{kab} \hat{c}^{\dagger}_{\tau as}(\boldsymbol{k}) \lambda_{\tau,ab}(\boldsymbol{k}, \boldsymbol{q}) \hat{c}_{\tau bs}(\boldsymbol{k}+\boldsymbol{q}), \tag{2.18}$$

where we have reintroduced the spin label.

2.3.2 Interactions

In terms of the form factors, the bare quartic part of the long-range interaction Hamiltonian is

$$\begin{aligned} \hat{H}_{\text{int}} &= \frac{1}{2A} \sum_{\tau s} \sum_{\boldsymbol{q}} V(\boldsymbol{q}) : \hat{\rho}^{\dagger}_{\tau s}(\boldsymbol{q}) \hat{\rho}_{\tau s}(\boldsymbol{q}) : \\ &= \frac{1}{2A} \sum_{\substack{ss'\tau\tau' \\ abcd}} \sum_{\boldsymbol{q}} \sum_{\boldsymbol{k}^{\alpha}, \boldsymbol{k}^{\beta} \in \text{ mBZ}} V(\boldsymbol{q}) \lambda_{\tau,a,b}(\boldsymbol{k}^{\alpha}, \boldsymbol{q}) \lambda^{*}_{\tau',d,c}(\boldsymbol{k}^{\beta}, \boldsymbol{q}) \\ &\qquad \times \hat{c}^{\dagger}_{\tau as}(\boldsymbol{k}^{\alpha}) \hat{c}^{\dagger}_{\tau' cs'}(\boldsymbol{k}^{\beta}+\boldsymbol{q}) \hat{c}_{\tau' ds'}(\boldsymbol{k}^{\beta}) \hat{c}_{\tau bs}(\boldsymbol{k}^{\alpha}+\boldsymbol{q}), \end{aligned} \tag{2.19}$$

where A is the area of the system. We consider a dual-gate screened interaction $V(q) = \frac{e^2}{2\epsilon_0 \epsilon_r q} \tanh qd$ with screening length $d = 25$ nm and relative permittivity $\epsilon_r = 10$ unless otherwise stated [78]. Casting $\hat{H}_{\text{int}}$ in the BM band basis makes sense since it is desirable to truncate to a subset of low-energy bands rather than keep all degrees of freedom up to the plane wave cutoff. Intervalley Coulomb scattering at momentum transfers $\boldsymbol{q} \sim \boldsymbol{K}$ is power law suppressed at small angles [79] and will be neglected for most of the ensuing analysis. However, this term is important for helping to break the $SU(2)_K \times SU(2)_{K'}$ symmetry to the physical $SU(2)$ and resolving some of the spin degeneracies of the correlated insulators. It leads to a ferromagnetic 'Hund's coupling' that prefers to align the spins in the two valleys. Phonon scattering provides a comparable antiferromagnetic contribution, such that the overall sign of the Hund's coupling is uncertain [80].

2.3.3 Hartree-Fock and subtraction

Consider a general interacting Hamiltonian in normal-ordered form

$$\hat{H}' = \hat{H}_{\text{kin}} + \hat{H}_{\text{int}} = \sum_{\alpha\beta} h_{\alpha\beta}\hat{c}^\dagger_\alpha \hat{c}_\beta + \frac{1}{2}\sum_{\alpha\beta\gamma\delta} V_{\alpha\beta\gamma\delta}\hat{c}^\dagger_\alpha \hat{c}^\dagger_\beta \hat{c}_\delta \hat{c}_\gamma. \tag{2.20}$$

A Slater determinant is described by its projector $P_{\alpha\beta} = \langle \hat{c}^\dagger_\alpha \hat{c}_\beta \rangle$, i.e. the one-body density matrix. In HF, we decouple the interaction term in the state P of the system. For reasons to be explained shortly, we may want to perform the mean-field decoupling relative to a reference projector P^0—by this we mean that P^0 should have no explicit interaction energy. This motivates the following HF Hamiltonian and expression for the total energy which prevents 'double-counting' of interactions

$$\hat{H}^{\text{HF}}[P] = \sum_{\alpha\beta} h_{\alpha\beta}\hat{c}^\dagger_\alpha \hat{c}_\beta + \sum_{\alpha\beta\gamma\delta}(P_{\gamma\delta} - P^0_{\gamma\delta})(V_{\alpha\gamma\beta\delta} - V_{\alpha\gamma\delta\beta})\hat{c}^\dagger_\alpha \hat{c}_\beta \tag{2.21}$$

$$E[P] = \sum_{\alpha\beta} h_{\alpha\beta}P_{\alpha\beta} + \frac{1}{2}\sum_{\alpha\beta\gamma\delta}(P_{\gamma\delta} - P^0_{\gamma\delta})(P_{\alpha\beta} - P^0_{\alpha\beta})(V_{\alpha\gamma\beta\delta} - V_{\alpha\gamma\delta\beta}). \tag{2.22}$$

Alternatively, we could have defined an equivalent description in terms of another Hamiltonian $\hat{H}$, where the decoupling is done with respect to just P

$$\hat{H} = \hat{H}_{\text{kin}} + \hat{H}_{\text{int}} - \hat{H}_{\text{d.c.}} \tag{2.23}$$

$$\hat{H}_{\text{d.c.}} = \sum_{\alpha\beta\gamma\delta} P^0_{\gamma\delta}(V_{\alpha\gamma\beta\delta} - V_{\alpha\gamma\delta\beta}). \tag{2.24}$$

Returning to TBG, it is tempting to declare that we should take the total Hamiltonian to be just $\hat{H} = \hat{H}_{\text{BM}} + \hat{H}_{\text{int}}$ without any additional modifications. However this prescription quickly runs into difficulty. The issues relate to PHS and the dependence on the plane wave cutoff in the BM model. For concreteness, let us assume that all the interesting physics occurs within the eight *active* central bands, and relegate the other *remote* bands to be spectator bands[8]. This means that we automatically fill (empty) all the remote valence (conduction) bands in our calculations. Now for a typical state at filling

[8] A more precise division is between *active* and *frozen* bands, since the term *remote* is generally used to refer to any bands that are not part of the central flat manifold. However for most of this thesis, we will take the active bands to be the central bands anyways, so any remote bands are indeed frozen.

factor $-4 < \nu < +4$, the central bands will be heavily renormalized due to the Hartree and Fock potentials of the filled remote bands, which formally constitute a reconstructed Dirac sea. Note that this cannot be absorbed as a chemical potential shift since the moiré superlattice imprints non-trivial momentum structure onto the moiré Bloch functions. Hence it makes sense to 'subtract' off such remote contributions. Furthermore, it is desirable to choose a scheme that respects the approximate PHS of the BM model[9], which requires subtracting off some central band pieces in $\hat{H}_{\text{d.c.}}$ as well. The net result is that the one-body part of the Hamiltonian for the central band degrees of freedom can be rather different from $\hat{H}_{\text{BM}}$. We denote the total one-body piece by $\hat{H}_{\text{SP}}$, which may be augmented to account for other factors like strain and substrate alignment.

The above considerations can be translated into a choice of the reference projector P^0. There is no unique prescription for fixing P^0, and several choices have been used in the literature with varying properties and motivations [55, 57–59, 77, 78, 81–86]. We caution that different schemes do not only lead to quantitative variations, but also contrasting qualitative behaviours for certain physical properties [57]. The basic issue is that the central bands are sufficiently narrow to begin with that the doping level and symmetry-breaking order substantially deform the effective dispersion in a detail-dependent manner [35, 87–90]. Ideally one would use multiple schemes and check that the theoretical predictions are robust.

We will primarily use the 'graphene' scheme where P^0 corresponds to the density of two *decoupled* graphene sheets at charge neutrality[10] [78, 85]. The physical motivation behind this choice is that the parameters (such as the bare Dirac velocity v_F) of the BM model are taken from *ab initio* calculations of monolayer graphene, and we should only count interactions about this reference point. This would avoid complications such as the logarithmic renormalization of the Dirac cone velocity [78].

In the charge neutrality or 'CN' scheme, P^0 is the density of filled valence bands up to the charge neutrality point of the BM model [77]. This is part of a family of related schemes parameterized by a reference filling ν^0, which guarantee the self-consistency of

[9]The experiments also exhibit PHS in many aspects, but not for some correlation signtures.

[10]Typically beyond some band cutoff far away from the central bands (but within the plane wave cutoff for diagonalizing the BM model), we assume that P^0 consists of the filled remote valence bands for simplicity. Bands that are too far from chage neutrality will be inaccurate anyways since they approach the boundary of the plane wave cutoff.

the BM band structure at filling $\nu = \nu^0$ [77, 84, 86].

In the 'average' or 'infinite-temperature' scheme, P^0 consists of filled remote valence bands, and takes the form $\frac{1}{2}\mathbb{1}$ in the central band manifold. The advantage of this scheme is that it makes strong coupling hierarchy of Section 2.4 manifest. Note that when the active bands consist of just the central bands, the final active Hamiltonian in the 'CN' and 'average' schemes makes no explicit reference to the remote bands.

Once a subtraction scheme has been chosen, the HF equations are solved in a self-consistent manner to determine the lowest energy Slater determinant. Multiple instances and types of input seed projectors are used to maximize the likelihood of convergence to the global minimum[11]. Depending on the calculation, we allow certain flavour and spatial symmetries to be broken, including moiré translation invariance if desired. The simplest Roothaan method (iteration) to solve the HF eqution often diverges due to 'charge-sloshing', especially if moiré translation symmetry is relaxed. To sidestep this and accelerate convergence, we employ the optimal damping algorithm which is guaranteed to find a local minimum [91].

2.4 Strong coupling

2.4.1 Chern basis

Since the typical Coulomb scale ($\sim \frac{e^2}{4\pi\epsilon a_{\mathrm{M}}} \sim 30\,\mathrm{meV}$) exceeds the kinetic bandwidth ($\sim 10\,\mathrm{meV}$) [92], the BM band basis may not be the most natural one in which to understand interaction physics. Indeed, as outlined in Section 1.1, there is ample experimental evidence for band reconstruction and flavour polarization, affording us the flexibility to move away from the kinetic basis. The role of the substrate in stabilizing the QAH at $\nu = +3$ and the proliferation of Chern insulating phases at finite magnetic field B advocate a different perspective that reveals the underlying topological character of the central bands and the connection to QHFM. A more appropriate basis choice is hence furnished by the *Chern basis* obtained by diagonalizing the sublattice operator σ_z [78]. Each Chern band is predominantly polarized on one sublattice, which allows us to label

[11] For skyrmions in Chapter 5, multiple seeds are useful for obtaining metastable skyrmion solutions as well.

the eight central bands with sublattice[12] σ, valley τ, and spin s. Combining these into a single index α, we can write the Bloch functions as $|\psi_\alpha(\boldsymbol{k})\rangle = e^{i\boldsymbol{k}\cdot\hat{\boldsymbol{r}}}\,|u_\alpha(\boldsymbol{k})\rangle$ with associated creation operators $\hat{d}^\dagger_\alpha(\boldsymbol{k})$. Crucially, these bands have non-trivial Chern number $C = \sigma_z\tau_z$ [44, 78, 93] and can be grouped into Chern quartets.

2.4.2 Generalized ferromagnets

The link to QHFM is sharpened in the well-studied chiral limit $\kappa = 0$ [75, 76], where the kinetic bandwidth becomes exactly zero at the magic angle and the Chern bands become completely sublattice polarized. In addition, the new chiral symmetry $\{\sigma_z, H_{\rm BM}\} = 0$, in concert with $\hat{C}_{2z}\hat{\mathcal{T}}$ and PHS $\hat{\mathcal{P}}$, heavily constrains the form factors $\lambda_{\alpha,\beta}(\boldsymbol{k},\boldsymbol{q})$ to be diagonal and to depend only the Chern number C_α: this allows us to write [78]

$$\lambda^{\rm S}_{\alpha\beta}(\boldsymbol{k},\boldsymbol{q}) = F^{\rm S}(\boldsymbol{k},\boldsymbol{q})e^{i\phi^{\rm S}(\boldsymbol{k},\boldsymbol{q})C_\alpha}\delta_{\alpha\beta}, \tag{2.25}$$

where the superscript 'S' denotes 'symmetric'. In the *chiral-flat* limit where the BM kinetic term is neglected[13], this implies a huge $U(4)_{C=1}\times U(4)_{C=-1}$ symmetry, as can be seen by checking the invariance of the density operator[14] $\hat{\rho}^{\rm S}(\boldsymbol{q}) = \sum_{\boldsymbol{k}} \hat{\boldsymbol{d}}^\dagger(\boldsymbol{k})\lambda^{\rm S}(\boldsymbol{k},\boldsymbol{q})\hat{\boldsymbol{d}}(\boldsymbol{k}+\boldsymbol{q})$ under independent Chern-number preserving rotations.

Remarkably in the chiral-flat limit at $\nu = 0$ for any repulsive interaction $V(\boldsymbol{q})$, one can prove the existence of exact Slater determinant ground states, which simply involve uniformly polarizing any four orthogonal directions within the Chern quartets ('generalized ferromagnets') [78, 83]. This is seen by exploiting the positive definiteness of the

[12] Note that σ does double duty as a Chern basis index and the microscopic sublattice index. It should be clear from the context which interpretation is being used.

[13] In addition, the subtraction term needs to satisfy the same emergent $U(4)\times U(4)$ symmetry, which is trivially the case for the 'average' scheme where P^0 is proportional to the unit matrix in the central band subspace. For the other schemes, we'd need to artificially set a particular combination of one-body terms (not just the BM kinetic term) to 0.

[14] Matrix-vector product over Chern band indices α,β is implied.

interaction Hamiltonian in the strong coupling limit

$$\hat{H}_{U_{\rm S}} = \frac{1}{2A}\sum_{\boldsymbol{q}} V(\boldsymbol{q}) \left[\delta\hat{\rho}^{\rm S}(\boldsymbol{q})\right]^{\dagger} \delta\hat{\rho}^{\rm S}(\boldsymbol{q}) \tag{2.26}$$

$$\delta\hat{\rho}(\boldsymbol{q}) = \hat{\rho}(\boldsymbol{q}) - \bar{\rho}(\boldsymbol{q}), \quad \bar{\rho}(\boldsymbol{q}) = \frac{1}{2}\sum_{\boldsymbol{kG}} \delta_{\boldsymbol{G},\boldsymbol{q}} \mathrm{Tr}\lambda^{\rm S}(\boldsymbol{k},\boldsymbol{G}), \tag{2.27}$$

which is just a rewriting of the interaction (including the subtraction term) in the 'average' scheme. $U_{\rm S}$ refers to the symmetric part of the interaction. Consider the action of $\delta\hat{\rho}^{\rm S}(\boldsymbol{q})$ on any generalized ferromagnet $|\Psi\rangle$ at $\nu = 0$. This vanishes for $\boldsymbol{q} \neq \boldsymbol{G}$ because we have filled Chern bands and the density operator is diagonal in this basis. For $\boldsymbol{q} = \boldsymbol{G}$, we could have terms like $\sim \sum_{\boldsymbol{k}} F^{\rm S}(\boldsymbol{k},\boldsymbol{G}) \sin\phi^{\rm S}(\boldsymbol{k},\boldsymbol{G}) |\Psi\rangle$ if Ψ has non-zero Chern number. However TRS $\hat{\mathcal{T}} = \tau_x\mathcal{K}$, where $\mathcal{K}$ is complex conjugation, constrains $F^{\rm S}(-\boldsymbol{k},-\boldsymbol{q}) = F^{\rm S}(\boldsymbol{k},\boldsymbol{q}), \phi^{\rm S}(-\boldsymbol{k},-\boldsymbol{q}) = \phi^{\rm S}(\boldsymbol{k},\boldsymbol{q})$. Combining this with (2.17), we obtain $F^{\rm S}(-\boldsymbol{k},\boldsymbol{G}) = F^{\rm S}(\boldsymbol{k},\boldsymbol{G}), \phi^{\rm S}(-\boldsymbol{k},\boldsymbol{G}) = -\phi^{\rm S}(\boldsymbol{k},\boldsymbol{G})$. Therefore the summation over $\boldsymbol{k}$ vanishes, meaning that we have an exact zero-energy ground state. In fact, the above construction for exact generalized ferromagnetic ground states can be extended to non-zero integer fillings if one imposes an additional 'flat-metric condition' on the form factors [83][15]. In this way, we have analytic solutions for strong-coupling insulators at every integer ν.

2.4.3 Hierarchy of scales

The utility of the chiral-flat limit lies in the existence of a hierarchy of scales which permits corrections to be treated perturbatively within the manifold of $U(4) \times U(4)$ ferromagnets [78, 83]. The energy scale of the full symmetry group is $U_{\rm S} \sim 20\,\mathrm{meV}$, and the main competing scales at physically relevant parameters are the single-particle inter-Chern tunneling ($t_{\rm S} \sim 5\,\mathrm{meV}$) and deviation from chirality ($U_{\rm A} \sim 5\,\mathrm{meV}$), with intra-Chern dispersion ($t_A \sim 1\,\mathrm{meV}$) being subleading[16].

Focusing for simplicity on the spinless insulator at neutrality such that the parent symmetry group is $U(2) \times U(2)$, the effects of the above perturbations can be captured

[15] The flat metric condition requires that $\lambda_{\alpha\beta}(\boldsymbol{k},\boldsymbol{G}) = \xi(\boldsymbol{G})\delta_{\alpha\beta}$. This is trivially true for $\boldsymbol{G} = 0$, and is approximately satisfied for large $\boldsymbol{G}$ due to the decaying Bloch function overlaps. Hence the largest violations are for the smallest shell of non-zero RLVs. The integer correlated states obtained through other numerical means suggest that the flat metric condition is a decent approximation [83].

[16] Explicit expressions for these scales can be found in Refs. [57, 78].

via anisotropies with positive strengths J and λ (i.e. energy scales $E_J = A_{\mathrm{UC}}J$ and $E_\lambda = A_{\mathrm{UC}}\lambda$). It turns out that the states that get energetically selected by these terms have total $C = 0$. Defining an intra-Chern Pauli triplet $\boldsymbol{\eta}$ and an inter-Chern Pauli triplet $\boldsymbol{\gamma}$

$$\boldsymbol{\eta} = (\sigma_x\tau_x, \sigma_x\tau_y, \tau_z), \quad \boldsymbol{\gamma} = (\sigma_x, \sigma_y\tau_z, \sigma_z\tau_z), \tag{2.28}$$

we can parameterize the strong-coupling ferromagnets residing in the Chern-neutral sector with two Chern-filtered pseudospins

$$\boldsymbol{n}_\pm(\boldsymbol{k}) \equiv \langle\Psi|\, \hat{\boldsymbol{d}}^\dagger(\boldsymbol{k})\boldsymbol{\eta}\frac{1 \pm \sigma_z\tau_z}{2}\hat{\boldsymbol{d}}(\boldsymbol{k})\,|\Psi\rangle \tag{2.29}$$

which are independent of $\boldsymbol{k}$. Inter-Chern tunneling generates superexchange $\sim J$, inducing an anti-ferromagnetic (AFM) coupling between the two pseudospins, while a finite chiral ratio κ causes the density operator to develop less symmetric parts, manifesting as a coupling $\sim \lambda$ that is AFM in-plane and FM out-of-plane. Both break the chiral-flat symmetry to distinct $U(2)$ subgroups [78]. The resulting easy-plane ground state with $\boldsymbol{n}_+ = -\boldsymbol{n}_-$ (and hence valley-$U(1)_V$ degeneracy) is the KIVC, so called because it preserves a modified Kramers TRS $\hat{\mathcal{T}}' = \tau_y\hat{\mathcal{K}}$, and possess intervalley coherence (IVC). An equivalent description of the spinless KIVC is via its density matrix $P = \frac{1}{2}(1+Q)$, where

$$Q_{\mathrm{KIVC}} = \sigma_y(\tau_x\cos\phi_{\mathrm{IVC}} + \tau_y\sin\phi_{\mathrm{IVC}}) \tag{2.30}$$

is parametrized through the IVC angle ϕ_{IVC}.

A similar analysis can be performed at the other integer fillings to determine the specific ferromagnets that are selected by the anisotropies [83, 94]. Complementary numerical techniques, such as HF, DMRG, quantum Monte Carlo, and exact diagonalization obtain ground states that are similar to generalized ferromagnets [58, 78, 81, 83, 85, 86, 95–99], thereby validating the strong coupling treatment of the interacting BM model.

Part I

Neutral and charged excitations at strong coupling

Chapter 3

Topological excitons

The structure of the ground states of condensed matter systems intricately affects their low-temperature properties, and is imprinted in the spectrum of low-energy quasiparticles and long-wavelength collective excitations. Electrical insulators generically break no continuous symmetries and hence lack gapless collective modes, and are gapped to charge transport in their bulk. However, interactions can stabilize excitons, which are bound states of a hole in the valence band and an electron in the conduction band. While also gapped, excitons typically have lower energy than unbound particle-hole (PH) excitations and dominate the optical response of direct-gap semiconductors, where they can be excited at zero wavevector. More generally, excitons form at a fixed center-of-mass (COM) wavevector $\boldsymbol{q}$ set by the momentum separation between the valence band maximum and conduction band minimum. The spectrum and transport properties of excitons can also be modified by the topology of the electronic bands near these extrema [100, 101]. This is captured by the *excitonic* Berry curvature [102] linked to the evolution of the two-particle bound state across its BZ. Such considerations are relevant, for example, to 2D transition metal dichalcogenides[1] [103], where the valley-contrasting anomalous velocity of excitons has been experimentally observed [104].

In this chapter, we focus on excitons of the $\nu = +3$ QAH in TBG aligned with the hBN substrate, i.e. hBN-TBG [27, 28]. We investigate features of the exciton spectrum and topology in hBN-TBG that are linked to the flatness and nontrivial Chern number of

[1] Certain hexagonal TMDs can be loosely thought of as 'gapped graphene'—the gapping of the Dirac points leads to a high concentration of Berry curvature at the BZ corners.

the underlying single-particle bands and the spontaneous breaking of time-reversal and spin rotation symmetries. In Section 3.1, we root our understanding of the universal topological features in an analytically tractable model that mimics the features of the hBN-TBG band structure by leveraging the mapping between $|C| = 1$ Chern bands and LLs. In Section 3.2, we return to TBG and demonstrate that topological excitons with a narrow bandwidth can indeed arise in the interacting BM model. Motivated by the emergence of flat-band topological bosons, we propose a fractional quantum Hall hierarchy built from excitons in Sec. 3.3. We close with a conclusion in Sec. 3.4. The work in this chapter is based on Refs. [53, 54].

3.1 Landau levels in opposite fields

3.1.1 Landau level mapping

In Sec. 2.4.1, we discussed how the Chern basis, obtained by diagonalizing the sublattice operator σ_z, highlights the topology of the central moiré bands. The alignment[2] of the hBN substrate with the graphene layers gaps the Dirac cones and makes this topology manifest, leading to four degenerate bands below and above charge neutrality [79, 105]. For simplicity in this section, we assume the effective sublattice splitting Δ is large enough so that we can focus our attention on the four conduction bands (say polarized on the A sublattice), which are distinguished by spin $s =\uparrow,\downarrow$ and valley $\tau = \pm$ quantum numbers. The valleys have Chern numbers $C = \tau$ and are interchanged by TRS. At $\nu = +3$ and near the magic angle, the suppressed bandwidth allows interactions to stabilize TRS-breaking valley- and spin-polarized states in which a partial subset of the bands is fully occupied—a mechanism proposed to explain the observed QAH response in hBN-TBG [28]. Such systems are sometimes referred to as orbital Chern insulators (OCIs) [106–108] to emphasize the central role played by the orbital physics rather than spins (which remain disordered in the absence of external fields at finite temperature due to the Mermin-Wagner theorem). This is in contrast to other QAH materials such as magnetic topological insulator thin films [109].

[2]The question of what constitutes ideal alignment is subtle, since hBN and TBG have a slight lattice mismatch—see discussion in Chapter 4.

To gain physical intuition and make analytical progress, we exploit the topological equivalence between $|C| = 1$ Chern bands and LLs, and consider a system of four flavors of electronic lowest Landau levels (LLLs) confined to the plane. The two valleys $\tau = \pm$ experience opposite magnetic fields $\boldsymbol{B} = -\tau B\hat{z}$, chosen to model the Chern structure of the conduction bands of hBN-TBG, and we neglect Zeeman splitting since there is no *real* external magnetic field. In Landau gauge $\boldsymbol{A}_\tau = -\tau Bx\hat{y}$, the LLL wavefunctions are $\phi_{k\tau}(\boldsymbol{r}) \propto e^{iky}e^{-\frac{(x-\tau k)^2}{2}}$, which are created by $c^\dagger_{k\tau s}$. We take $\ell_B \equiv (\hbar/eB)^{1/2} = 1$ throughout. The projected LLL Hamiltonian is [110]

$$\hat{H} = \frac{1}{2}\sum_{\substack{kpq\\ \tau\tau' ss'}} V_{\tau\tau'}(k,p,q)c^\dagger_{k+q,\tau s}c^\dagger_{k+p-q,\tau' s'}c_{k+p,\tau' s'}c_{k,\tau s} - \sum_{kp\tau s} V_{\tau+}(k,p,0)c^\dagger_{k\tau s}c_{k\tau s} + \text{const.}, \tag{3.1}$$

where the second term is the potential of a uniform background charge (equivalent to a filled $\tau = +$ LLL), and $U(\boldsymbol{r}) = e^2/r$ describes Coulomb interactions with LLL matrix elements $V_{\tau\tau'}(k,p,q) \equiv \langle k+q,\tau; k+p-q,\tau'|\,\hat{U}\,|k,\tau; k+p,\tau'\rangle$[3]. The form of (3.1) is motivated by TBG, where interactions have $SU(2)$ spin rotation invariance and the suppressed intervalley scattering contributions are neglected [79].

3.1.2 Collective modes

We consider a uniform fully spin- and valley-polarized ground state, assuming without loss of generality that the filled flavour is $(+,\uparrow)$, viz. $|G\rangle \equiv \prod_k c^\dagger_{k+\uparrow}|\text{vac}\rangle$ (Fig. 3.1a). The scenario with three filled flavours is equivalent via PH conjugation. Following Ref. [110], we compute the collective mode spectrum in the time-dependent Hartree-Fock approximation (TDHFA, equivalent to the generalized random phase approximation [111]). We solve the dynamics restricted to the basis of single PH pairs, created by the neutral

[3]The explicit expressions are

$$V_{++}(k,p,q) = \frac{e^2}{L_y}\sqrt{\frac{2}{\pi}}\int_{-\infty}^{\infty} dx\, K_0(|qx|)e^{-\frac{1}{2}(x^2+2(p-q)x+q^2+(p-q)^2)} \tag{3.2}$$

$$V_{-+}(k,p,q) = \frac{e^2}{L_y}\sqrt{\frac{2}{\pi}}\int_{-\infty}^{\infty} dx\, K_0(|qx|)e^{-\frac{1}{2}(x^2+(4k+2p)x+4k(k+p)+p^2+q^2)}. \tag{3.3}$$

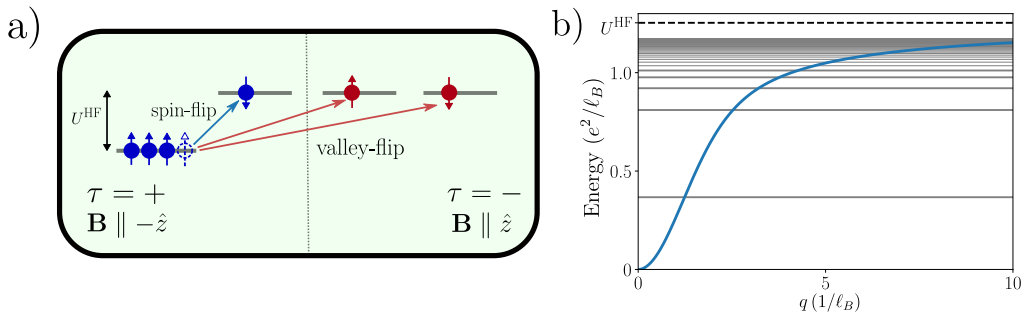

Figure 3.1: a) Schematic of the four-flavour LLL at effective filling $\nu = 1$, showing the exchange splitting $U^{\mathrm{HF}} = \sqrt{\frac{\pi}{2}}\frac{e^2}{\ell_B}$ and the different neutral excitation types. b) Spin wave energy (blue curve) as a function of y-momentum q for $\alpha = 0$ (i.e. vanishing x-momentum). Spin wave dispersion is isotropic in 2D momentum space. Horizontal lines show the momentum-independent valley-flip exciton energies. Both modes saturate to U^{HF}.

operators $b^\dagger_{\tau s}(k,q) \equiv c^\dagger_{k+q,\tau s} c_{k,+\uparrow}$ that satisfy the equation of motion

$$-i\partial_t b^\dagger_{\tau s}(k,q) = \big(\epsilon^{\mathrm{HF}}_{\tau s}(k+q) - \epsilon^{\mathrm{HF}}_{+\uparrow}(k)\big) b^\dagger_{\tau s}(k,q) - \sum_{k'} V_{\tau+}(k+q, k'-k-q, k'-k) b^\dagger_{\tau s}(k',q), \tag{3.4}$$

where $(\tau, s) \neq (+,\uparrow)$, and the k-independent HF energies are $\epsilon^{\mathrm{HF}}_{\tau s} = -\delta_{s\uparrow}\delta_{\tau+}\sum_p V_{++}(\cdot, p, p)$. (3.4) is closed for a given τ, s, and momentum transfer q as these are conserved by the Hamiltonian. Therefore, TDHFA is *exact* for the one PH subspace since we neglect LL mixing.

We solve (3.4) by finding operators $\gamma^\dagger_{\tau s}(q) = \int dk\, \psi_{q\tau s}(k) b^\dagger_{\tau s}(k,q)$ such that to leading order in $\gamma_{\tau s}(q)$, $[\hat{H}, \gamma^\dagger_{q\tau s}(k)] = \omega_{\tau s}(q)\gamma^\dagger_{q\tau s}(k)$, where $\omega_{\tau s}(q)$ is the excitation energy. The coefficients $\psi_{q\tau s}(k)$ satisfy

$$\big(U^{\mathrm{HF}} - \omega_{\tau s}(q)\big)\, \psi_{q\tau s}(k) = \int dk'\, T_{q,\tau}(k,k')\psi_{q\tau s}(k'), \tag{3.5}$$

where the kernel $T_{q,\tau}(k,k') = \frac{L_y}{2\pi} V_{\tau+}(k'+q, k-k'-q, k-k')$ and the exchange splitting $U^{\mathrm{HF}} = \sqrt{\frac{\pi}{2}}\frac{e^2}{\ell_B}$. Discretizing (3.5) yields a 1D hopping problem for each q, with matrix element $T_{q,\tau}(k,k')$ between sites k, k'.

3.1.2.1 Intravalley spin-wave mode

For $(\tau, s) = (+, \downarrow)$ and fixed q, the hopping kernel $T_{q,\tau}(k, k')$ depends only on $k - k'$. With the ansatz $\psi_{q\tau s}(k) \sim e^{ik\alpha}$ [110], the energy of this spin wave collective mode is given by [112, 113]

$$\omega_{+\downarrow}(q, \alpha) = U^{\mathrm{HF}} - \int dk\, e^{ik\alpha} V_{++}(\cdot, k - q, k), \tag{3.6}$$

plotted in Fig. 3.1b. The dispersion is isotropic in the (q, α) plane, where α can be interpreted as the x-momentum [110]. As expected for the single Goldstone mode corresponding to the ferromagnetically broken $SU(2)$ symmetry [114, 115], $\omega_{+\downarrow}(q)$ is gapless and quadratic for $q \to 0$ [112, 113, 116]. For $q \to \infty$ it saturates to U^{HF} (the loss of exchange energy in creating a hole) since in this limit electron and hole are sufficiently distant that their Coulomb interaction energy vanishes.

3.1.2.2 Intervalley exciton mode

A more interesting case is that of intervalley excitations where $\tau = -$. The spectrum is spin-independent since $\hat{H}$ is $SU(2)$-symmetric. In fact, the spectrum $\omega_{-s}(q)$ is also independent of q, and hence macroscopically degenerate—a consequence of the 'shift symmetry' of the kernel, $T_{q,-}(k, k') = T_{q+2\delta,-}(k - \delta, k' - \delta)$, where increasing q by δ corresponds to shifting the effective 1D hopping problem by $-\delta/2$. This holds for any interaction potential, not just Coulomb. The sign and the factor of two is strongly suggestive of the notion that $b^\dagger_{\tau s}(k, q)$ creates an excitation that couples to the magnetic field with an effective strength $2eB$ (recall the position-momentum locking of LLs, $\langle x \rangle = \tau k l_B^2$). This leads to a discrete q-independent spectrum of excitonic bound states (Fig. 3.1b) described by harmonic oscillator wavefunctions $\psi_{q\tau s}(k; n) \propto H_n\left[\sqrt{2}(k + \frac{q}{2})\right] e^{-(k+\frac{q}{2})^2}$ centered at $-q/2$, where H_n is a Hermite polynomial corresponding to LLs in an effective magnetic field $2B$.

For rotationally invariant interactions we can capture key features of the excitons [54] by working in symmetric gauge and performing a PH transformation on the $\tau = +$ valley,

yielding a two-body Hamiltonian for the $\tau = +$ hole and $\tau = -$ electron

$$H_{\text{exc}} = \frac{(\boldsymbol{p}_e + e\boldsymbol{A})^2}{2m} + \frac{(\boldsymbol{p}_h + e\boldsymbol{A})^2}{2m} - U(\boldsymbol{r}), \tag{3.7}$$

where we recall the opposite magnetic fields in the two valleys $\boldsymbol{A}_e = -\boldsymbol{A}_h = \boldsymbol{A}$. Transforming to COM and relative coordinates $\boldsymbol{R} = \frac{\boldsymbol{r}_h + \boldsymbol{r}_e}{2}, \boldsymbol{r} = \boldsymbol{r}_h - \boldsymbol{r}_e$ and momenta $\boldsymbol{P} = \boldsymbol{p}_h + \boldsymbol{p}_e, \boldsymbol{p} = \frac{\boldsymbol{p}_h - \boldsymbol{p}_e}{2}$, the Hamiltonian cleanly decouples into COM and relative sectors

$$H_{\boldsymbol{R}} = \frac{(\boldsymbol{P} + 2e\boldsymbol{A})^2}{4m} \tag{3.8}$$

$$H_{\boldsymbol{r}} = \frac{(\boldsymbol{p} + \frac{e}{2}\boldsymbol{A})^2}{m} - U(r). \tag{3.9}$$

The COM sector is a LLL problem for a charge $-2e$ particle in field $-B\hat{z}$. Accordingly, each discrete excitonic bound-state solution of $H_{\mathbf{r}}$ has a $2N_\Phi$-fold degeneracy corresponding to the LL degeneracy of the COM sector $H_{\mathbf{R}}$. The relative motion corresponds to a charge $-e/2$ particle in the same field and a Coulomb central potential. Solving this in terms of Haldane pseudopotentials [117] yields discrete exciton binding energies $E_m = -\frac{e^2}{\ell_B}\frac{\Gamma(m+\frac{1}{2})}{2\Gamma(m+1)}$ (where $m \geq 0$ is an integer and Γ is the gamma function), in agreement with the numerical solution of (3.5). The intervalley exciton is a composite neutral object which sees an effectively doubled magnetic field, and whose COM and relative motion are topologically non-trivial due to Landau quantization for any interaction. In analogy to usual electronic LLs, we expect the exciton bands to have Chern number $|C_{\text{exc}}| = 1$, as we verify in the next subsection. Semiclassical quantization also gives a macroscopic COM degeneracy and discrete relative energy levels, because of the Lorentz-force deflection of electrons and holes as they attract in opposing magnetic fields. In contrast, for the usual case of identical fields the PH pair is free to propagate and its energy is non-degenerate [118].

3.1.3 Excitonic Berry curvature

We are ultimately interested in studying Chern bands in zero-field crystalline systems with small but non-zero dispersion and non-uniform Berry curvature. To check what aspects of our results survive away from the fine-tuned LLL limit, we perturb our model

with a finite dispersion and Berry curvature inhomogeneity. To help bridge the gap to the crystalline setting, we transform to the magnetic Bloch basis indexed by two-dimensional momenta $\boldsymbol{k}$ in the magnetic BZ. Picking a square unit cell with side $a = \sqrt{2\pi}$ enclosing unit flux (for magic-angle TBG with $a \simeq 14\,\mathrm{nm}$, this corresponds to $B \simeq 5\,\mathrm{T}$), the single-particle magnetic Bloch operators are [79] $d^\dagger_{\boldsymbol{k}\tau} = \frac{1}{\sqrt{N_x}} \sum_{n=0}^{N_x-1} e^{i\tau k_x (k_y+nQ)} c^\dagger_{k_y+nQ,\tau}$ where $Q = \frac{2\pi}{a}$ is the BZ length and the spin index has been dropped as we are focusing on intervalley modes. Following Ref. [79] we introduce a potential $V(\boldsymbol{r}) = -w(\cos\left(\frac{2\pi x}{a}\right) + \cos\left(\frac{2\pi y}{a}\right))$, which is diagonal in this basis and projects to a single-particle dispersion $\epsilon_{\boldsymbol{k}} = -we^{-\frac{\pi}{2}}(\cos k_x a + \cos k_y a)$ in the LLL. Solving the discretized TDHFA equations, we find that exciton energies evolve with the CM momenta $\boldsymbol{q}$, forming bands within the BZ. The topology of exciton bands is encoded in their Berry curvature [102], as we now summarize.

The exciton state is

$$\left|\psi^{\mathrm{exc}}_{\boldsymbol{q}}\right\rangle = \sum_{\boldsymbol{k}} \psi_{\boldsymbol{q}}(\boldsymbol{k}) d^\dagger_{\boldsymbol{k}+\frac{\boldsymbol{q}}{2},-} d_{\boldsymbol{k}-\frac{\boldsymbol{q}}{2},+} \left|G\right\rangle . \tag{3.10}$$

After PH-transforming the + valley, we can write

$$\left|u^{\mathrm{exc}}_{\boldsymbol{q}}\right\rangle = e^{-i\boldsymbol{q}\hat{\boldsymbol{R}}} \sum_{\boldsymbol{k}} \psi_{\boldsymbol{q}}(\boldsymbol{k}) \left|\phi_{\boldsymbol{k}+\frac{\boldsymbol{q}}{2},-}\right\rangle \left|\phi^*_{\boldsymbol{k}-\frac{\boldsymbol{q}}{2},+}\right\rangle , \tag{3.11}$$

where $|\phi_{\boldsymbol{k},\tau}\rangle$ are the single-particle Bloch states, and the $e^{-i\boldsymbol{q}\hat{\boldsymbol{R}}}$ prefactor ensures that the cell-periodic part $\left|u^{\mathrm{exc}}_{\boldsymbol{q}}\right\rangle$ of $\left|\psi^{\mathrm{exc}}_{\boldsymbol{q}}\right\rangle$ satisfies $\boldsymbol{q}$-independent boundary conditions [119].

The Berry connection and gauge-invariant Berry curvature are then computed from $\left|u^{\mathrm{exc}}_{\boldsymbol{q}}\right\rangle$. If $\boldsymbol{a}^\tau = i\left\langle u^\tau_{\boldsymbol{q}}\right| \boldsymbol{\nabla}_{\boldsymbol{q}} \left|u^\tau_{\boldsymbol{q}}\right\rangle$ and $f^\tau = \boldsymbol{\nabla}_{\boldsymbol{q}} \times \boldsymbol{a}_\tau(\boldsymbol{q})$ are the Berry connection and curvature of the underlying single-particle bands, the exciton Berry curvature takes the form

$$\Omega_{\mathrm{exc}}(\boldsymbol{q}) = \Omega_{\mathrm{sp}}(\boldsymbol{q}) + \Omega_{\mathrm{e}}(\boldsymbol{q}) + \Omega_{\mathrm{sp,e}}(\boldsymbol{q}), \tag{3.12}$$

where (defining $\boldsymbol{k}_\pm = \boldsymbol{k} \pm \frac{\boldsymbol{q}}{2}$) the first contribution

$$\Omega_{\rm sp}(\boldsymbol{q}) = \frac{i}{4}\sum_{\boldsymbol{k}} |\psi_{\boldsymbol{q}}(\boldsymbol{k})|^2 \{f^+(\boldsymbol{k}_-) - f^-(\boldsymbol{k}_+)\} \tag{3.13}$$

stems from the single-particle Berry curvature,

$$\Omega_{\rm e}(\boldsymbol{q}) \;=\; i\sum_{\boldsymbol{k}} \partial_{q_x}\psi_{\boldsymbol{q}}(\boldsymbol{k})\partial_{q_y}\psi^*_{\boldsymbol{q}}(\boldsymbol{k}) - \partial_{q_y}\psi_{\boldsymbol{q}}(\boldsymbol{k})\partial_{q_x}\psi^*_{\boldsymbol{q}}(\boldsymbol{k}) \tag{3.14}$$

captures the BZ evolution of the envelope function, and

$$\Omega_{\rm sp,e}(\boldsymbol{q}) \;=\; \frac{i}{2}\sum_{\boldsymbol{k},\tau=\pm} \{\partial_{q_y}|\psi_{\boldsymbol{q}}(\boldsymbol{k})|^2 a_x^{-\tau}(\boldsymbol{k}_\tau) - (x \leftrightarrow y)\} \tag{3.15}$$

describes the coupling between the envelope function and the single-particle Berry connection. Due to the ambiguity in defining $\boldsymbol{a}$ and the phase of $\psi_{\boldsymbol{k}}(\boldsymbol{q})$, only the combination $\Omega_{\rm e} + \Omega_{\rm sp,e}$ is gauge-invariant. Numerically $\Omega_{\rm exc}(\boldsymbol{q})$ is computed on a finite momentum mesh by computing gauge-invariant (non-Abelian) lattice field strengths [120]. Integrating $\Omega_{\rm exc}(\boldsymbol{q})$ over the BZ gives a quantized exciton Chern number $C_{\rm exc} = \int_{\rm BZ} \frac{d^2q}{2\pi}\Omega_{\rm exc}(\boldsymbol{q})$.

Armed with this definition we return to our discussion of perturbing the solvable limit. At $w = 0$ the bands are flat and two-fold degenerate, consistent with the COM experiencing a doubled effective field. As the bandwidth is increased, the upper levels merge into a continuum, which engulfs additional bands as w grows [53]. At large enough w the lowest exciton band dips below $E = 0$, signaling an instability to a partially-polarized state at the one-exciton level. We also introduce Berry curvature inhomogeneity by artificially deforming the Landau gauge states[4] [53], and find that this also leads to a weak exciton dispersion. These results illustrate that the exciton dispersion arises from the interplay of the underlying band geometry, topology, dispersion, and interactions. We have also explicitly verified that low-lying exciton bands remain topological[5] with

[4]This is done by introducing a 'wobble' factor $w(k)$ into the Landau gauge eigenstates that respects the square lattice periodicity $w(k+Q) = w(k)$ and the the time-reversal relation of the two valleys $w(-k) = -w(k)$

$$\phi_{k,\tau}(w;\boldsymbol{r}) = \frac{1}{\sqrt{L_y \pi^{\frac{1}{2}}}} e^{iky} e^{-\frac{[x-\tau(k+w(k))]^2}{2}}. \tag{3.16}$$

The resulting magnetic Bloch states have Berry curvature $f^\tau(\boldsymbol{k}) = \tau + \tau\partial_{k_y} w(k_y)$.

[5]See Appendix A for an analytical calculation of the exciton Chern number in the absence of pertur-

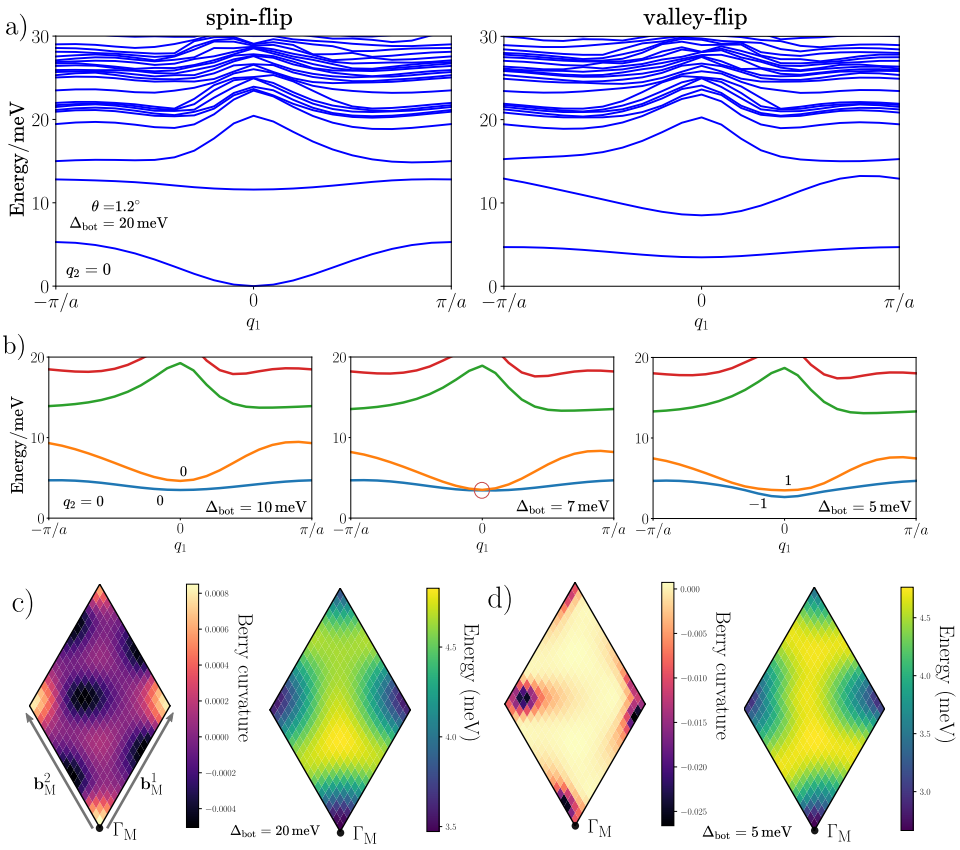

Figure 3.2: a) Spin- and valley-flip exciton spectrum of $\nu = +3$ QAH of hBN-TBG. b) As the substrate potential is varied, intervalley exciton bands cross at Γ_M in a topological transition where the Chern numbers of the lowest bands change as indicated with $|\Delta C_{\text{exc}}| = 1$. c) Berry curvature (multiplied by the mBZ area) and exciton energy for the lowest valley-flip band of a) in the mBZ. (Note that the conventions for the basis RLVs are different to those introduced in Sec. 2.2). d) Same as c) but for the $C_{\text{exc}} = -1$ band of the final panel of b). System size is 20×20.

$C_{\text{exc}} = 1$ under these perturbations, even as they acquire dispersion and Berry curvature fluctuations of their own.

3.2 Excitons in TBG

We now turn to spin and valley-flip excitons of the OCI in hBN-TBG, for which our starting point is the continuum model of Ref. [9] with twist angle $\theta \simeq 1.2°$. We choose $w_{\text{AA}} = 80\,\text{meV}$ and introduce a sublattice splitting $|\Delta| = 20$ meV on the bottom layer. We use a dual-gate screened interaction with relative permittivity $\epsilon = 9.5$ and screening

bations.

length $d_{\rm sc} = 40$ nm, and use the 'graphene' subtraction scheme. Projecting to the eight central bands, we calculate the fully flavor-polarized self-consistent QAH state at the experimentally-relevant filling $\nu = +3$ [28], from which we compute the single valley-flip or spin-flip excitonic spectra using the TDHFA[6] [111, 121]. We do not consider interband excitons that are not charged under valley or spin (such excitations exist since we keep both valence and conduction BM bands). The results are shown in Fig. 3.2 (see caption for more details). Consistent with previous studies that focused on energetics [116, 122], we find that the lowest spin-flip mode is gapless and disperses quadratically at zero momentum, while the valley-flip modes are all gapped (Fig. 3.2a). The lowest valley-flip exciton has a narrow bandwidth $\simeq 1\,$meV, and is energetically separated from higher modes (Fig. 3.2c)

For the above parameters, we find that the lowest two exciton bands have $C_{\rm exc} = 0$. We emphasize however that the physics of TBG shows large sample-to-sample variations sensitive to the precise device parameters and experimental conditions. Indeed, by varying the substrate strength, we can induce a set of band touching events which renders the lowest exciton band topological (Fig. 3.2b,d). This reveals that the different terms in (3.12) can give competing contributions to the exciton Berry curvature. Specifically, the non-trivial structure of the envelope function $\psi_{\boldsymbol{q}}(\boldsymbol{k})$ can render exciton bands trivial even if the underlying single-particle bands have equal and opposite Chern numbers and yield a nonzero gauge-invariant $\Omega_{\rm sp}(\boldsymbol{q})$. Despite these subtleties, it seems plausible that hBN-TBG can host low-lying topological exciton branches in realistic parameter regimes.

As with other topological collective modes [123–125], a non-zero Chern number for a bulk exciton band indicates the presence of chiral exciton modes [126–128] localized at the boundary of the QAH domain, traversing the bulk exciton gap to connect to a band with a distinct Chern number. These modes allow unidirectional exciton transport, acting as chiral channels for valley charge, but only emerge in TBG for a narrow range of parameters. However, even when the lowest exciton band has $C_{\rm exc} = 0$, we nevertheless find substantial curvature inherited from the underlying Chern bands (Fig. 3.2c). This can drive anomalous exciton transport in the bulk [102, 104]. Each valley-flip exciton of QAH systems such as hBN-TBG is associated with a $U(1)$ valley charge. Since the latter

[6] See Appendix B for the technical details.

is to very good approximation conserved in these systems, excitons are likely long-lived. Direct optical addressing of these excitons is challenged by the momentum mismatch between the valleys; however, it may be possible to supply this 'missing momentum' from another source, e.g. phonons [129].

3.3 Excitonic fractional quantum Hall hierarchy

3.3.1 Setup

The emergence of narrow-band topological excitons in hBN-TBG paves the way for the possible formation of novel many-exciton phases similar to the bosonic fractional quantum Hall (FQH) effect [54, 130]. To generalize our discussion to other OCI platforms, we distill the minimal ingredients necessary for our theoretical proposal. We require our system to possess two nearly-flat degenerate Chern bands with equal and opposite Chern number $C = \tau$ indexed by a conserved 'valley' quantum number[7], and we ignore spin for simplicity. For sufficiently strong interactions, the ground state at $\nu = 1$ is a fully valley-polarized Chern insulator (FVPI) with quantized Hall conductivity $\sigma_{xy} = \frac{e^2}{h}$. We assume the details of the system are such that the lowest intervalley exciton band is topological $|C_{\text{exc}}| = 1$ with a small bandwidth.

As in Sec. 3.1, we capture the main qualitative features of the problem by replacing the Chern bands with LLLs where the valleys experience equal and opposite magnetic fields. The filling factor of the LLL pair is fixed at $\nu = \nu_+ + \nu_- = 1$, where $\nu_\pm = N_\pm/N_\Phi$ is the filling factor in each valley, and $N_\Phi = A/2\pi\ell_B^2$ is the LL degeneracy. The interacting Hamiltonian (3.1) can be rewritten as

$$H_{\text{int}} = \frac{1}{2N_\Phi} \sum_{\mathbf{q},\tau,\tau'} V_{\tau\tau'}(\mathbf{q}) : \bar{\rho}_\tau(\mathbf{q})\bar{\rho}_{\tau'}(-\mathbf{q}) : . \tag{3.17}$$

Here, we have introduced the projected density operators

$$\bar{\rho}_\pm(\mathbf{q}) = F(\mathbf{q}) \sum_{k_y} e^{\pm i q_x k_y \ell_B^2} c^\dagger_{k_y - \frac{q_y}{2},\pm} c_{k_y + \frac{q_y}{2},\pm}, \tag{3.18}$$

[7] We emphasize that for generality, this need not correspond to an actual valley degree freedom like in hBN-TBG.

where $F(\mathbf{q}) = e^{-\mathbf{q}^2\ell_B^2/4}$ and $c^\dagger_{k_y,\pm}$ is the creation operator of a Landau-gauge single-particle LLL state $\phi_{k_y,\pm}(x) = \frac{e^{ik_y y} e^{-(x\mp k_y\ell_B^2)^2/2\ell_B^2}}{\sqrt{L_y \ell_B \sqrt{\pi}}}$. We choose a phenomenological interaction that only includes density-density terms

$$V_{\tau,\tau}(\mathbf{q}) = v(\mathbf{q}) = \frac{2\pi e^2}{|\mathbf{q}|}, \quad V_{\tau,-\tau}(\mathbf{q}) = v_d(\mathbf{q}) = v(\mathbf{q}) e^{-|\mathbf{q}|d}, \tag{3.19}$$

where d tunes the competition of inter and intravalley interactions. Essentially, this interaction corresponds to that of a quantum Hall bilayer where the valley corresponds to the layer. The FVPI at $\nu = 1$ is stable against both the inclusion of a weak nonzero single-particle dispersion, as well as allowing $d > 0$. Although the former is also true for conventional QHFMs where all bands have $C = 1$, the latter is unexpected: arguing in analogy with bilayer quantum Hall systems, we would anticipate that softening the intervalley interactions in this way would stabilize intervalley-coherent states with $\nu_+ = \nu_- = \frac{1}{2}$. However when $C_+ = -C_-$, even for $d \to 0$ the symmetry is reduced relative to the $C_+ = C_-$ case [79]. This is evident in the gap to the intervalley excitons of the FVPI as discussed in Sec. 3.1, which used an isotropic interaction potential.

From the analysis of (3.8) and (3.9), we can write down wavefunctions for the intervalley exciton in the symmetric gauge after performing a PH transformation in the filled $\tau = +$ band. Letting z_e, z_h be complex coordinates for the electron and hole respectively, defining $z = \frac{z^e + z^h}{2}$ and $u = z^h - z^e$, and freezing the relative coordinate u in the lowest excitonic bound state ϕ_0 with relative angular momentum $m = 0$ yields

$$\psi_{\text{exc}}(z, u) = \tilde{f}(z) e^{-|z|^2/2} \phi_0(u) \;\text{ with }\; \phi_0(u) \equiv e^{-|u|^2/8}, \tag{3.20}$$

where $\tilde{f}$ is analytic. Note that z (u) sees an effectively doubled (halved) field.

Each exciton also carries a unit of $U(1)_V$ valley polarization. Since the latter is conserved it is meaningful to consider partially valley-polarized states corresponding to a finite density of excitons. A coherent interlayer exciton condensate is expected for standard quantum Hall bilayers at $\nu_+ = \nu_- = \frac{1}{2}$ [131]. However in the present situation, similar HF trial states are energetically uncompetitive in much of the phase diagram because exciton topology forces them to host a vortex lattice analogous to Type-II super-

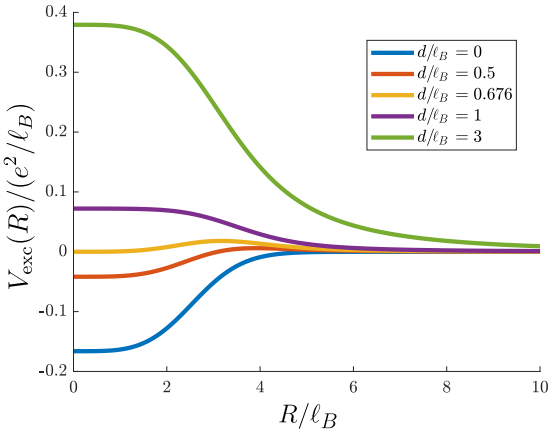

Figure 3.3: Exciton-exciton interaction profile for different d, which tunes the competition of intervalley and intravalley interactions.

conductors in a magnetic field [79]. Evidently, as bosons in a magnetic field the excitons can form various other many-body states inaccessible to a HF analysis, depending on the effective exciton-exciton interaction $V_{\rm exc}(R)$

In order to estimate the inter-exciton interaction, we consider the following single-exciton wavefunctions whose COM is localized at some position $\boldsymbol{R}$

$$\psi_{\text{exc},\boldsymbol{R}}(z^h, z^e) = \frac{e^{-\frac{|R|^2}{2}}}{2\pi} e^{z(R_{0,x}-iR_{0,y})} e^{-\frac{|u|^2}{8}-\frac{|z|^2}{2}}. \tag{3.21}$$

We propose the following antisymmetrized state for two localized excitons separated by $\boldsymbol{R}$

$$\Psi_{\text{exc},\boldsymbol{R}}(\{z^h\},\{z^e\}) \sim \mathcal{A}_e\mathcal{A}_h \psi_{\text{exc},\boldsymbol{R}}(z_1^h, z_1^e)\psi_{\text{exc},\boldsymbol{0}}(z_2^h, z_2^e) \tag{3.22}$$

where $\mathcal{A}_{h(e)}$ antisymmetrizes the holes (electrons). Evaluating the expectation value of the interaction using the potential in (3.19), we obtain

$$V_{\rm exc}(R) = \frac{e^{-\frac{R^2}{4}}(F[I_0 v] - F[I_0 v_d]) + e^{-\frac{3R^2}{4}}(F[J_0 v] - F[J_0 v_d]) - e^{-\frac{R^2}{4}}F[J_0 v] - e^{-\frac{3R^2}{4}}F[I_0 v] + 2e^{-\frac{R^2}{2}}F[v_d]}{1 - 2e^{-\frac{R^2}{2}} + e^{-R^2}}$$

$$F[I_0 V] \equiv \int_0^\infty dr\, r I_0\left(\frac{rR}{2}\right) e^{-\frac{r^2}{4}} V(r)$$

$$F[J_0 V] \equiv \int_0^\infty dr\, r J_0\left(\frac{rR}{2}\right) e^{-\frac{r^2}{4}} V(r)$$

$$F[V] \equiv \int_0^\infty dr\, r e^{-\frac{r^2}{4}} V(r)$$

where J_0 and I_0 are the unmodified and modified Bessel functions of the first kind. This

interaction is plotted in Fig. 3.3 for several values of d. The denominator reflects the normalization—as the excitons come within $\sim \ell_B$, their envelopes begin to overlap[8]. Short-range interactions are repulsive if $d/\ell_B \gtrsim 1$, and attractive if $d/\ell_B \lesssim 1$. For any $d > 0$, excitons experience an asymptotic R^{-3} repulsion that vanishes for $d = 0$. A power-law tail is generically expected, but its exponent may depend on the choice of $v(\mathbf{r})$.

3.3.2 Excitonic many-body states

We consider fillings $(\nu_+, \nu_-) = (1 - \nu_v, \nu_v)$ with $0 < \nu_v < \frac{1}{2}$, corresponding to adding $\nu_v N_\Phi$ intervalley excitons to the FVPI resulting in valley polarization $I_v^z = \frac{1}{2} - \nu_v$ per electron. For now we assume that exciton binding sets the dominant energy scale and that the inter-exciton interaction V_{exc} is always repulsive and short-ranged. Since each exciton behaves as though it occupies a $2N_\Phi$-fold degenerate LL, the effective filling factor is $\nu_b = \nu_v/2$. For $\nu_v = 1/m$ with m an integer, the tightly-bound excitons can form a $\nu_b = 1/2m$ bosonic Laughlin state. A trial wavefunction that captures this is given by

$$\Psi_{2m}(\{z^e, z^h\}) = \mathcal{P}_{\text{exc}}[\Psi_m(\{z^e\})\Psi_m(\{z^h\})] = \sum_{\sigma \in S_N} \operatorname{sgn}\sigma [\Psi_m(\{z_{i,\sigma(i)}\})^2 \prod_j \phi_0(u_{j\sigma(j)})]. \tag{3.23}$$

Here, $\Psi_m(\{z\}) = \prod_{i<j}(z_i - z_j)^m e^{-\sum_i \frac{|z_i|^2}{4}}$ and $\mathcal{P}_{\text{exc}}$ projects electron-hole pairs into the lowest excitonic level ϕ_0 [(3.20)]. This antisymmetrizes over permutations $\sigma \in S_N$ corresponding to different 'pairings' of the $N = N_\Phi/m$ electrons i and holes $\sigma(i)$ to form excitons centered at $z_{i\sigma(i)} = \frac{1}{2}(z_i^e + z_{\sigma(i)}^h)$ at separation $u_{i\sigma(i)} = z_i^h - z_{\sigma(i)}^e$ and then projects the latter onto ϕ_0[9]. $\Psi_{2m}(\{z^e, z^h\})$ is a many-body state of electrons in valley '−' and holes in valley '+', built on top of the FVPI parent state. Undoing the PH transformation

[8] This highlights a subtlety when considering many-body exciton phases, which is that single-exciton states are not all independent [132]. While this is unimportant in the dilute limit $\nu_- = 1 - \nu_+ \ll 1$, we will be interested in fillings $\nu_- = 1/m$ where m is not necessarily large. We will ignore this subtlety and consider the excitons as *bona fide* bosons.

[9] Explicitly, if $\Psi_\sigma(\{z, u\})$ is the original wavefunction written in terms of COM $(z_{i,\sigma(i)} = \frac{z_i^h + z_{\sigma(i)}^e}{2})$ and relative $(u_{i,\sigma(i)} = z_i^h - z_{\sigma(i)}^e)$ variables for a given pairing σ, then $\mathcal{P}_{\text{exc}}$ acts as

$$\mathcal{P}_{\text{exc}}\Psi(\{z^e, z^h\}) = \sum_{\sigma \in S_N} \operatorname{sgn}\sigma \int d\{u'\}\Psi_\sigma(\{z, u'\}) \prod_i \phi(u_{i,\sigma(i)})\phi^*(u'_{i,\sigma(i)}). \tag{3.24}$$

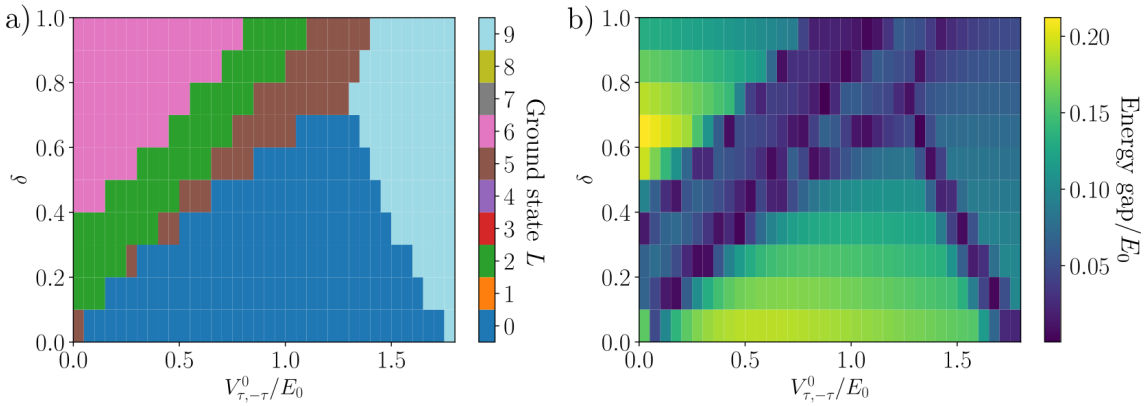

Figure 3.4: a) Phase diagram for the ground state angular momentum L from exact diagonalization for $N_+ = N_- = 5$ fermions on a sphere with flux $N_\phi = 16$, appropriate for the $m = 4$ excitonic Laughlin state. The Haldane pseudopotentials in units of $E_0 = e^2/\ell_B$ are $V^1_{\tau,\tau} = 1, V^3_{\tau,\tau} = 0.4, V^1_{\tau,-\tau} = -\delta, V^3_{\tau,-\tau} = -0.4\delta$, while the magnitude of $V^0_{\tau,-\tau}$, which is always negative, is freely varied. Hence δ controls the isotropy of the interaction (note that $V^0_{\tau,\tau}$ does not affect the spectrum due to the Pauli principle). b) Energy gap between lowest and first-excited multiplets.

in (3.23) in the '+' valley yields a purely electronic wave function.

An alternative picture of the excitonic phase structure, which allows for relatively straightforward numerical tests, is obtained by viewing the problem (after PH transformation to holes in valley '+') as a two-valley system where each component sees the *same* magnetic field and is at filling $\nu = 1/m$, and where intervalley (intravalley) interactions are attractive (repulsive) [133]. This gives distinct pictures for odd and even m. In each case, the electronic state is obtained after undoing the PH transformation.

For m odd and zero intervalley interactions, each component forms an *independent* $\nu = 1/m$ fermionic Laughlin state. Intervalley attraction locks these together, suppressing fluctuations where a particle in one valley is far from a hole in the other. However, as each valley is independently incompressible, the presence of a unique ground state in numerics does not provide confirmation of the excitonic Laughlin state.

For m even, we can attach m quanta of flux to each valley separately, yielding an equal density of composite fermions in each valley. For weak intervalley attraction we anticipate that these are stable against pairing [134], yielding a compressible state. For increasing attraction, we expect a transition into an intervalley paired state of composite

fermions, schematically given by

$$\Psi_{2m}^{\mathrm{CF}} \sim \mathcal{P}_{LLL} \prod_{i<j} (z_i^e - z_j^e)^m \prod_{k<l} (z_k^h - z_l^h)^m \det[g(z_i^e - z_j^h)] \tag{3.25}$$

where the determinant describes pairing with wavefunction $g(z)$, $\mathcal{P}_{LLL}$ projects to the LLL, and we have omitted Gaussian factors. For s-wave or strong-coupling higher-angular momentum pairing, we expect $g(z) \sim e^{-z/\xi}$ as $z \to \infty$, where $\xi \sim \mathcal{O}(\ell_B)$ is the pair size. Qualitatively, this pairs electrons and holes into tightly-bound bosons that then form a $\nu_b = 1/2m$ Laughlin state. This is consistent with our picture of (3.23), so we conclude that the two approaches describe similar physics. In non-s-wave cases, strong- and weak-pairing regimes are separated by a phase transition. For p_x+ip_y-pairing where $g(z) \sim 1/z$, this would be a transition between state (3.23) and the $(m-1, m-1, 1)$ Halperin state which also has $\nu = 1/m$ in each valley[10]. For $m = 4$, preliminary exact diagonalization studies[11] find a unique ground state in this valley polarization sector for $N = 4, 6, 8, 10$ particles on the sphere [117] at a shift [136] of 4 appropriate to (3.23) for certain short-range interactions (see caption of Fig. 3.4 for details of the interaction). This suggests that the excitonic Laughlin state is energetically competitive as there is no other obvious incompressible candidate at this shift. (Note that this is not necessarily the global ground state across all valley sectors.) Further numerical work is required to fully flesh out the phase structure and verify the applicability of (3.23).

Other unconventional phases are also possible. For example, if $\nu_v = 2/q$ with q odd, the exciton filling is $\nu_b = 1/q$, ruling out bosonic Laughlin states. In this limit, attaching q quanta of $U(1)_V$ valley flux to each exciton gives rise to a compressible excitonic composite Fermi liquid (e-CFL). This does not obviously decouple into separate flux attachments to constituent electrons/holes. The e-CFL has intervalley binding but no valley coherence, and is hence distinct from interlayer coherent CFLs [137] proposed in QH bilayers.

So far we have ignored the long-range tail of $V_{\mathrm{exc}}(R)$. While this is unlikely to destabilize FQH liquids favored by short-range repulsive interactions, the competition between

[10] The equivalence of (3.25) with $p_x + ip_y$ pairing to the Halperin state follows via the Cauchy identity [131, 135].

[11] Exact diagonalization numerics were performed using the DiagHam package [http://www.nick-ux.org/diagham/wiki/] for multicomponent fermions on the sphere.

short-range attraction and long-range repulsion [138] can drive the formation of vortex lattices and bubble and stripe phases [139, 140]. Similarly at lower density, Wigner-crystal like phases of excitons can be formed [141]. These states all have broken translational symmetry.

3.3.3 Edge structure and response

We now discuss transport properties and bulk response of the states considered above. Since the excitonic Laughlin state (3.23) is a bosonic FQH state, we expect a quantized response in the 'charge' carried by this state, which leads to a fractional quantized valley Hall response, $\sigma^V_{xx} = 0$, $\sigma^V_{xy} = -\nu_b \frac{q_V^2}{h} = -\frac{1}{2m}\frac{q_V^2}{h}$, where $q_V = 1$ is the valley charge of a single exciton. We can understand this also from an edge-state perspective. Before implementing exciton projection, in terms of the underlying electrons we can view the edge of (3.23) as built out of (i) a chiral $\nu_+ = 1$ mode of electrons in a filled LL; (ii) a chiral $\nu_+ = 1/m$ edge mode of holes in valley '+'; and (iii) a chiral $\nu_- = 1/m$ edge of electrons in valley '−'. Owing to the opposite charge of holes and the opposite sign of B in the two valleys (ii) and (iii) counter-propagate relative to (i) and co-propagate relative to each other. The exciton projection can then be viewed as binding the two co-propagating fermionic FQH edge modes due to the attractive electron-hole interactions, leading to a single bosonic $\nu_b = 1/2m$ mode propagating upstream of the charge mode.

Other cases are more complicated. For $\nu_v = 1/m$ with m even and weak intervalley interactions, we have decoupled CFL-like states [133] in which the quantized charge Hall response breaks down in favor of metallic transport. In contrast, for $\nu_v = 2/q$ with q odd, since the exciton binding dominates, both compressible and incompressible phases have a charge QH response. In the compressible e-CFL state this coexists with 'metallic' valley response from the exciton Fermi surface.

Experimentally, it is challenging to distinguish different exciton phases via electrical measurements, since nearly all of them have identical $\sigma_{xy} = e^2/h$ charge Hall response. While it is difficult to directly measure the valley Hall response, 'upstream' modes can be detected by measuring thermal conductance K_H [142]. If the upstream and downstream modes are fully thermally equilibrated, then $K_H = 0$, whereas if they are out of equi-

librium we expect a doubled response relative to the integer quantum Hall case. Phases with quantized valley Hall response show plateaus in valley polarization quantized at a rational fraction of its value in the FVPI, which would be another diagnostic.

3.4 Outlook

Electronic topology is usually diagnosed through electronic properties, e.g. quantized Hall conductivity σ_{xy} in Chern insulators. In this chapter, motivated by the properties of hBN-TBG at $\nu = +3$, we studied spontaneously TRS-breaking QAH systems (or OCIs) whose non-interacting band structure possesses degenerate and nearly flat bands ('valleys') with opposite Chern numbers, and where interactions are sufficiently strong to open a topological gap at integer filling. We found that the lowest intervalley excitons can be remarkably flat with a non-trivial exciton Chern number [53]. Furthermore, we proposed a new class of correlated states where topological excitons form a bosonic Laughin state on top of the parent QAH insulator [54].

We leveraged the topological equivalence of Chern bands and LLs to map the problem to the simpler case of a pair of LLLs in opposite magnetic fields in order to extract the key topological features. The quality of such an approximation is influenced by factors such as band flatness and quantum geometry [75, 76]—part of the interest in TBG is driven by the existence of limits where such properties are not far off from those in the LL caricature. However, there are details which reveal some of the weak links of the mapping. For example, in Sec. 3.2 we saw that the actual C_{exc} of the lowest exciton bands can depend sensitively on model parameters even though the QAH state remains robust in hBN-TBG. It would be interesting to construct analytically tractable lattice-based toy models to investigate how the contributions in (3.12) conspire to destroy the exciton topology away from the LL limit, and refine our intuition as to what systems are likely to harbour topological excitons. In Sec. 3.3, we used an inter-electron potential corresponding to a bilayer system with finite separation d in order to induce repulsive inter-exciton interactions required for the excitonic Laughlin states. However, the intra- and inter-Chern interactions are comparable—the pertinent bands are related by TRS and hence have the same spatial layer structure. The flexibility of the moiré paradigm

provides alternative arenas for such physics that may prove more favourable. The QAH has also been experimentally detected in ABC trilayer graphene aligned with hBN [143] and AB-stacked $MoTe_2/WSe_2$ [144]. Richer layer structures are present in twisted double bilayer [145–148] and twisted mono-bilayer graphene [106, 149], which have valley Chern numbers that are tuned by a vertical displacement field. In addition, the application of a small perpendicular magnetic field stabilizes Chern insulators over a wider range of fillings and systems.

Chapter 4

Domain walls

In the previous chapter, the starting point for the ground state in hBN-TBG at $\nu = +3$ was assumed to be a uniform bulk (translation-invariant) OCI, arising from full spin and valley polarization. A key ingredient is thought to be the alignment to the hBN, which is often modelled as a spatially constant sublattice splitting term $\sim \Delta\sigma_z$. The actual situation encountered experimentally is likely more involved than the intuitive picture painted above [55]. For example, the precise form of the substrate coupling is complicated by the fact that graphene and hBN have a $\sim$2% lattice mismatch and generally form their own alignment-dependent moiré pattern [150–152]. For small deviations away from a low-order commensurate superstructure, large regions (greater than the TBG moiré scale $a_{\mathrm{M}} \sim 14$ nm) emerge which are distinguished by the local properties of the single-particle bands, in particular the assignment of Chern numbers [152]. Other factors such as lattice imperfections and relaxation can also contribute to the spatial variations. Therefore in the presence of hBN-alignment, we generally expect electron interactions to locally polarize the TBG bands into large domains differing by quantum numbers such a Chern number and valley polarization.

Boundaries, or domain walls (DWs), between such domains host topologically-protected gapless modes. Similar DWs in QHFMs have been studied previously [153–158] and have been visualized on the surface of bismuth via STM [159]. As in QHFMs, DWs in magic-angle TBG generically host a pair of gapless dispersing one-dimensional modes. However as we discuss below, the unique setting of the OCI in hBN-TBG means that problem of DWs here inherits qualitatively new features due the presence of a lattice and the richer

Chern structure.

In this chapter, we focus on the properties and energetics of such DWs. In Sec. 4.1, we delineate the different types of DWs that can arise in hBN-TBG, and write down an effective field theory description. In Sec. 4.2, we develop a novel numerical technique to simulate DWs within mean-field theory, and comment on the obtained results. We close with an outlook in Sec. 4.3. The work in this chapter is based on Ref. [55].

4.1 Theoretical considerations

4.1.1 Effective field theory

We first review the notations for the central moiré bands of hBN-TBG. As we are interested in the orbital physics, we drop the spin index s since we assume that the spins are always fully polarized at $\nu = +3$. The flat bands can be labelled by sublattice (A, B) and valley indices (K, K'). We introduce Pauli matrices $\sigma_\mu(\tau_\mu)$ that act in the sublattice (valley) space, with A, B (K,K') corresponding to $\sigma_z = \pm 1$ ($\tau_z = \pm 1$). Perfect sublattice-polarization only emerges in the chiral limit [75], but it is physically reasonable to retain this label more generally [56]. Locally, a sublattice potential $\propto \Delta\sigma_z$ breaks C_{2z} symmetry, gaps the Dirac points, and assigns equal and opposite Chern numbers $C = \sigma_z\tau_z$ to the two valleys. At odd integer filling factors and in the presence of a uniform sublattice coupling Δ, interactions lift the residual $\tau_z = \pm 1$ degeneracy, leading to an OCI state that spontaneously breaks valley and time-reversal symmetries. For example if $\Delta > 0$, favouring the B sublattice, then the empty band of the OCI is either KA or $K'A$ (we will just call this KA- or $K'A$-polarized, remembering that we are working at $\nu = +3$ so that there is one unfilled band).

To simplify the analysis, we phenomenologically model the spatial modulation of the substrate with a smoothly-varying (on the scale of a_{M}, so that $U(1)_V$ continues to be a good symmetry) sublattice splitting $\Delta(\boldsymbol{r})$ which can change sign. This captures the C_{2z}-breaking effect of the hBN and generally allows for regions with locally different Chern number assignments. In this way, we focus on the interaction physics and interplay between DWs, and remain agnostic to the precise single-particle mechanism that

necessitates their formation.

If $\Delta(\boldsymbol{r})$ varies slowly, then we expect that the state locally resembles an OCI. Fluctuations in the combined sublattice-valley space can be described by a CP^3 nonlinear sigma model (NLSM) [160], which can be understood from the strong coupling considerations in Sec. 2.4. However we extract the important physics by approximating it by a simplified free energy[1] $F = \int d^2\boldsymbol{r}\, f$ for fluctuations of $\mathbb{Z}_2$ and $O(3)$ order parameters m_z and $\boldsymbol{n}$, where

$$f \sim \rho_s \left[(\nabla m_z)^2 + \frac{(m_z^2-1)^2}{\beta^2 a_{\mathrm{M}}^2} \right] + \rho_v (\nabla \boldsymbol{n})^2 - \frac{\Delta(\boldsymbol{r})}{a_{\mathrm{M}}^2} m_z n_z. \tag{4.1}$$

Recalling the inter-Chern ($\boldsymbol{\gamma}$) and intra-Chern ($\boldsymbol{\eta}$) triplets in (2.28), we have defined $m_z \sim \langle \gamma_z \rangle$ and $\boldsymbol{n} \sim \langle \boldsymbol{\eta} \rangle$. m_z represents the local Chern number, which is taken to be Ising because of the energetic penalty arising from inter-Chern coherence [55, 79][2]. The second term inside square brackets in (4.1) suppresses smooth variations of the Chern number. $\boldsymbol{n}$ is the local valley moment—note that the in-plane components $n_\mu \sim \langle \sigma_x \tau_\mu \rangle$ for $\mu = x, y$ so that they describe the valley orientation within the Chern sectors. The stiffnesses ρ_s and ρ_v should be similar in magnitude, β is an anisotropy parameter of order unity, and we have neglected anisotropies for $\boldsymbol{n}$ that are allowed in principle, but expected to be small [160]. The substrate potential couples to the sublattice polarization $m_z n_z \sim \langle \sigma_z \rangle$. F is a coarse grained theory valid on scales large compared to a_M and is not expected to be quantitatively accurate for faster variations.

4.1.2 Domain wall types

We can now identify three distinct types of DW in the OCI. For specificity, we take the DWs to lie parallel to the y-axis and separate distinct 'bulk' regions. We fix $m_z = n_z \to +1$ [KA-polarized] for $x \to -\infty$, which is compatible with imposing $\Delta > 0$ in this limit (see Fig. 4.1). We can then classify DWs based on the limiting behavior of (m_z, n_z) as $x \to \infty$ across the DW:

1. **Chern walls**, where the Chern polarization flips at the DW but the valley polar-

[1] See Appendix C for details of how this free energy is motivated from the NLSM.

[2] In other words, inter-Chern rotations are part of neither the $U(4) \times U(4)$ Goldstone manifold in the chiral-flat limit, nor the pseudo-Goldstone manifold that persists upon introducing deviations away from this idealized limit. See discussion in Sec. 2.4.

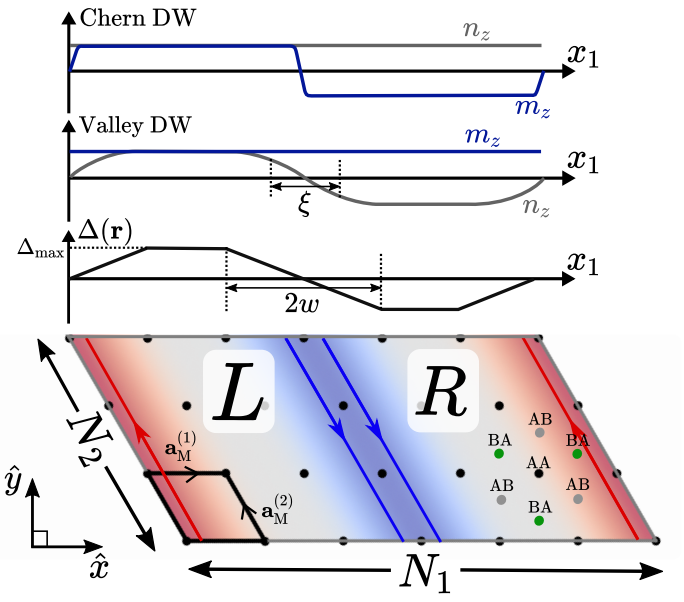

Figure 4.1: Top-down view of DWs and numerical set-up. We study systems of $N_{\text{tot}} = N_1 N_2$ moiré unit cells ($N_1 = 6, N_2 = 3$ Chern DW shown for illustration) with periodic boundary conditions. Black dots indicate AA stacking regions, where central bands have largest weight (AB, BA regions are also shown on the right). The substrate potential $\Delta(\boldsymbol{r})$ can vary along $\boldsymbol{a}_1$ (the sign-changing choice shown can stabilize two Chern or valley walls). Each Chern or intertwined DW hosts two localized co-propagating chiral modes, while a valley wall hosts non-chiral gapless modes. Top plots show the order parameter profiles for the Chern and valley walls.

ization stays the same: $(m_z, n_z) \to (-1, 1)$ [KB-polarized].

2. **Valley walls**, where the valley polarization flips while the Chern polarization is unchanged: $(m_z, n_z) \to (1, -1)$ [$K'B$-polarized].

3. **Intertwined walls**, where both Chern and valley indices change: $(m_z, n_z) \to (-1, -1)$ [$K'A$-polarized].

Examining F, it is evident that sign-changing substrate potentials (corresponding in our example to setting $\Delta < 0$ for $x \to \infty$) mandate the existence of intervening Chern or valley DWs, pinned along lines where $\Delta = 0$. In other words, the sublattice polarization has to flip from A to B, but there is still a choice for the valley polarization on each side of the $\Delta = 0$ contour.

If $\text{sign}(\Delta(\boldsymbol{r}))$ is uniform, then the two order parameters are no longer independent: a DW in m_z necessarily induces one in $\boldsymbol{n}$. One naïvely expects that in the absence of substrate pinning, such intertwined DWs can propagate through the sample and annihi-

late. However, the charge density of the central bands is modulated at the moiré scale so DWs experience a periodic potential that may pin their locations even if the substrate is uniform.

Therefore, for relatively uniform substrates, at any finite temperature entropic effects [161] will drive formation of intertwined domains weakly pinned at the moiré scale, whose Chern and valley polarization are locked by the sign of Δ. In contrast, for non-uniform substrates, we expect that the sample has Chern or valley domains that track variations in $\text{sign}(\Delta(\boldsymbol{r}))$. Are Chern or valley DWs favoured in this substrate-dominated regime? The answer has physical implications since Chern (and intertwined) DWs sew together bulk regions which differ in Chern number by ± 2. Hence they necessarily host at least a pair of chiral co-propagating edge modes—backscattering is forbidden by DW chirality, locking the Luttinger parameter to its non-interacting value. Valley DWs carry counter-propagating modes and their Luttinger parameters can be renormalized by forward scattering, or they can be gapped by backscattering if microscopic $U_V(1)$-breaking terms which we have neglected here are included.

Flipping valley polarization n_z across a DW is associated with a loss of exchange energy, penalizing the valley DW relative to the Chern DW. This cost is lowered if valley DWs develop a spatial texture, i.e, rotate smoothly over some length scale ξ due to the finite valley stiffness. We expect that smaller substrate potential gradients will favour valley DWs since they allow more texturing. Assuming a constant gradient Δ_{max}/w that switches sign at $x = 0$, variational arguments show that the width of a valley DW scales as $\xi \sim a_{\text{M}}[\rho_v/(a_{\text{M}}\Delta_{\text{max}}/w)]^{1/3}$ [154]. In contrast a Chern DW cannot smoothly interpolate between its two domains (recall m_z in (4.1) is a $\mathbb{Z}_2$ variable). Physically this is because any region of inter-Chern coherence is topologically forced to admit vortices in its order parameter [79], an effect that can counteract valley exchange physics. As a result, Chern DWs do not texture, and have a substrate-independent width of order a_M. Hence we expect smoother substrate gradients to benefit valley DWs over Chern DWs.

4.2 Numerical calculations

4.2.1 Methods

To substantiate the theoretical arguments in the previous section, we perform numerical HF calculations similar to those outlined in Sec. 3.2, but relax the requirement of translation symmetry in our HF projector P. For simplicity, we maintain moiré translation symmetry along $\boldsymbol{a}_2$ (envisioning a substrate modulation that is parallel to a moiré lattice direction) so that the HF states satisfy

$$\langle \hat{c}^\dagger_{\tau a s}(k_1, k_2)\hat{c}_{\tau' a' s'}(k_1', k_2')\rangle = \delta_{k_2,k_2'}\delta_{s,s'}P_{k_1\tau a;k_1'\tau' a'}(k_2, s) \tag{4.2}$$

and $\mathrm{Tr}P(k_2) = 7N_1$, reflecting the 7 filled central bands at $\nu = +3$. This corresponds to DWs oriented parallel to $\boldsymbol{a}_2$. The states we find are always fully spin-polarized.

The substrate potential $\Delta(\boldsymbol{r})$ presents a numerical challenge since it is not clear how to incorporate it into the translation invariant BM model. We innovate a method to treat spatially inhomogeneous substrate configurations: we project $\Delta(\boldsymbol{r})$ into the fixed Hilbert space spanned by the Bloch functions of the central bands [55]. This is justified by the large energy gap between the central and remote bands. It can be checked that the central band Hilbert spaces of the BM model solved with $\Delta = 0$ have $> 99\%$ overlap with those for the values of $\Delta \neq 0$ considered here, justifying this approach.

We determine the HF DW states self-consistently for different substrate configurations. We partition the system along $\boldsymbol{a}_1$ into equally sized left (L) and right (R) regions (Fig. 4.1). A convenient auxiliary basis for HF simulations is furnished by the single-particle HF Wannier-Qi (HFWQ) states $|W_{K\tau ns}\rangle$ [79, 93, 162–165]. These are strip wavefunctions maximally localized perpendicular to the DW, obtained by calculating the bulk HF Bloch orbitals $\left|\psi^{\mathrm{HF}}_{\tau ns}(\boldsymbol{k})\right\rangle$ in a valley-diagonal QAH state and taking a 1D Fourier transform[3]. n denotes the HF band index, and the dependence on the substrate Δ is not stated explicitly (the HFWQ construction is repeated for both positive and negative values of Δ to obtain all four possible QAH bulk wavefunctions). The purpose of the HFWQ construction is to provide an alternative basis for the bulk QAH phase that is

[3]There is no topological obstruction to exponential localization in 1D.

localized perpendicular to the DWs. The expression for $|W_{K\tau ns}\rangle$ is

$$|W_{K\tau ns}\rangle = \sum_{m_1=0}^{N_1-1} \frac{1}{\sqrt{N_1}} e^{-\mathrm{i}\sum_{m_1'=0}^{m_1} \mathcal{A}_{\tau n}^{(1)}(m_1',m_2) - \mathrm{i}\frac{2\pi m_1}{N_1}\left(\tilde{m}_1 - \frac{\theta_{\tau n}(m_2)}{2\pi}\right)} \left|\psi_{\tau ns}^{\mathrm{HF}}(m_1,m_2)\right\rangle \tag{4.3}$$

where $K = \frac{m_2}{N_2} + \tilde{m}_1$, $\tilde{m}_1 = 0, 1, \ldots, N_1 - 1$, and the momentum in the discretized momentum grid is $\boldsymbol{k} = \sum_i \frac{m_i}{N_i}\boldsymbol{b}_i$. The Chern number of the bulk HF bands can be obtained by inspecting the winding of the 1D polarization $\theta_{\tau n}(m_2) = \left(\sum_{m_1=0}^{N_1-1} \mathcal{A}_{\tau n}^{(1)}(m_1,m_2)\right)$ mod 2π, with $\mathcal{A}_{\tau n}^{(1)}(m_1,m_2)$ the discretized Berry curvature along b_1 direction. $0 \leq K < N_1$ is also approximately the average position of the HFWQ wavefunction in the $\boldsymbol{a}_1$ direction (it would be exactly the average position if the Berry curvature were uniform).

In the HF calculation of the DWs, the HFWQs are useful for constructing initial seed projectors to target specific types of DW. For example, we can bias towards a Chern wall by occupying the HFWQs corresponding to the KA-polarized QAH in region L, and KB-polarized QAH in region R. The nature of the converged HF solution can be ascertained by computing overlaps with the HFWQs (see Fig. 4.2).

Energy and spatially-resolved information on a DW solution $|\Phi\rangle$ can be extracted by computing the $T = 0$ local single-particle spectral function (see Fig. 4.2) which enters the expression for the tunneling conductance in an STM experiment

$$A_S(\omega,\boldsymbol{r}) = \sum_{\gamma\tau sI}\left[\left|\langle\gamma|\hat{\psi}_{\tau sI}^\dagger(\boldsymbol{r})|\Phi\rangle\right|^2\delta(\omega - E_\gamma + E_\Phi) + \left|\langle\gamma|\hat{\psi}_{\tau sI}(\boldsymbol{r})|\Phi\rangle\right|^2\delta(\omega + E_\gamma - E_\Phi)\right], \tag{4.4}$$

where γ runs over excited states, and $\hat{\psi}_{\tau sI}^\dagger(\boldsymbol{r})$ is a real-space creation operator for a given valley τ, spin s, and layer/sublattice I. The electron removal and addition matrix elements are approximated by their HF values using Koopman's theorem.

4.2.2 Results

Fig. 4.2 shows representative results for the three types of DW. For the case of a sign change in $\Delta(\boldsymbol{r})$, we choose $\Delta(\boldsymbol{r})$ so that it takes constant values $\pm\Delta_{\max}$ in region L/R. Depending on the initial conditions, this leads to a (meta)stable state with two Chern or valley DWs. For the Chern DW solution, there are clearly two pairs of co-propagating

chiral modes that cross the bulk band gap, and are localized at each Chern DW. Similar comments hold for the intertwined DWs that can exist as a metastable state without a modulating sublattice potential. On the other hand, the solution for the valley DW does not show any gapless modes at mean-field level because the broken $U(1)_V$ symmetry allows the counter-propagating modes to gap out. However a gapless mode must reemerge as quantum fluctuations restore $U(1)_V$ symmetry along the one-dimensional DW.

In order to investigate the competition between Chern and valley DWs, we pick $\Delta(\boldsymbol{r})$ so that it takes constant values $\pm\Delta_{\max}$ deep inside regions L/R, and linearly interpolates between them at the boundaries over a width $2w$. Fig. 4.3 shows the energy difference between the two configurations as a function of substrate gradient and twist angle. As expected, lower substrate gradients benefit valley DWs by penalizing valley rotations less, manifesting in the total exchange energy of valley DWs approaching that of Chern DWs as the substrate gradient goes to zero. Furthermore, smaller twist angles favour Chern DWs. One or the other DW type emerges from this competition as the lowest-energy solution in different parameter regimes. While beyond-HF corrections (e.g. random phase approximation) and different choices of interaction subtraction scheme can modify precise phase boundaries, our calculations provide strong evidence that Chern-valley DW competition is a generic feature of the Chern-insulating regime of TBG. [For small $\Delta_{\max}$, the DW cost can exceed the bulk penalty for the 'wrong' sign of $m_z n_z$; for finite N_1, this stabilizes a spurious uniform solution which will become uncompetitive as $N_1 \to \infty$.]

Fig. 4.4 shows the characteristic width ξ of the Chern and valley DWs for a range of substrate widths at fixed $\theta = 1.2°$. Evidently ξ is controlled by the substrate gradient $\Delta_{\max}/w$. For smaller $\Delta_{\max}/w$, the valley wall is in the scaling regime with an exponent which matches the Ginzburg-Landau prediction of $-1/3$. For large substrates, the scaling regime is cut off by the moiré lengthscale. In contrast, the Chern DW is very sharp with $\xi \lesssim a_{\mathrm{M}}$ independent of $\Delta_{\max}/w$, consistent with a large easy-axis anisotropy β in Eq.(4.1) and with the topological arguments [79] that suppress inter-Chern coherence.

For uniform $\Delta(\boldsymbol{r})$, intertwined DWs naturally stabilize at half-odd-integer positions between AA-stacking regions of maximal central band charge density[4]. For our largest

[4]One possible explanation is the following. The Chern number switching of the intertwined DW means that it pays a large energy penalty in the region of inter-Chern coherence. This cost is minimized if the DW is positioned between AA sites where the central band electronic density is not peaked. See

system sizes and a range of initial conditions, intertwined DWs fail to relax to uniform solutions even after many iterations, instead pinning on the moiré-scale charge inhomogeneity. This suggests that such domains can only grow or shrink in discrete steps of $a_{\mathrm{M}} \sim 14$ nm, i.e. intertwined DWs are long-lived metastable configurations. Despite sharing the same valley exchange physics as valley DWs, intertwined DWs are far less textured with characteristic length a_{M} due to Chern number switching. With a domain wall tension of $\sim 4\,\mathrm{meV}/a_{\mathrm{M}}$, this leads to a Curie temperature of order 40 K [166]. Therefore, intertwined wall proliferation is likely not the temperature-limiting factor of the ordered state. A similar analysis leads us to conclude that the phase transition arising from thermal fluctuations between Chern and valley walls occurs at temperatures much too large to be relevant for experiments [55][5].

4.3 Outlook

In this chapter, motivated by the likely presence of disorder/quasiperiodicity in the alignment of the substrate in hBN-TBG, we have proposed the existence of three distinct types of DWs in the OCI regime at $\nu = +3$, and numerically computed their properties in HF using the interacting BM model [55]. Chern and valley DWs emerge in substrate fluctuation-dominated samples comprised of domains with opposite local effective sublattice mass. Their competition is determined solely by the energetics at the DW region since the corresponding bulk regions are degenerate, and depends sensitively on microscopic details such as the twist angle and effective substrate gradient. In contrast, for more uniform substrates the metastability of intertwined DWs due to moiré pinning points to a distinct scenario where valley and Chern physics are locally linked. The substrate modulations that induce Chern/valley DWs also produce additional bound states at energies far from the Fermi energy (compared to the temperature), absent in the intertwined DW. While non-universal and topologically unprotected, these could provide a way to

similar comments on moiré pinning of skyrmions in Chapter 5.

[5] From the Chern versus valley DW phase diagram in Fig. 4.3, we can extract an effective line tension $\epsilon \sim 0.5\mathrm{meV}/a_{\mathrm{M}}$ for having the wrong DW. Assuming that the substrate forms a checkerboard pattern that varies on a lengthscale ξ_{dis}, and is strong enough so that the bulk domains simply track the local sublattice splitting, we can map the problem to a 2D Ising model of domain variables living on the plaquettes of the checkboard, where the 'ferromagnetic' state corresponds to where the QAH domains align according to the preferred type of DW. This gives a critical temperature $T_c \sim 13K \times \frac{\xi_{\mathrm{dis}}}{a_{\mathrm{M}}}$.

distinguish the two regimes, e.g. via STM on single-gated samples (Fig. 4.2).

Our results suggest that variations in twist angle and the sign of the substrate potential play a complex role in OCIs. In extreme limits where one type of DW is dominant across the sample, we expect that they either disrupt global valley order while retaining a robust global magnetization (if valley DWs dominate), or else lead to a vanishing net Chern number but a robust global valley order (if Chern DWs dominate). More generally, we expect a mixed scenario where both situations occur in different regions of a single sample. An added subtlety is that such fluctuations are likely to be quasiperiodic rather than truly random. In samples where $\mathrm{sign}(\Delta(\boldsymbol{r}))$ is relatively uniform, we expect instead intertwined domains that disrupt both valley order and magnetization, pinned to the moiré potential or possibly to weak variations in $\Delta(\boldsymbol{r})$ or twist angle. Pinning of DWs of various kinds is likely relevant to understanding current-driven magnetization reversal [108, 167].

Our results have implications for the observation of the QAH in TBG and other OCIs. In particular, we provide a candidate explanation for why some TBG samples at filling $\nu = +3$ exhibit the QAH whereas others do not. If electrical transport is dominated by percolating Chern or intertwined DWs, macroscopic QAH response is always destroyed due to the chiral DW network, which is similar in some respects to a doubled Chalker-Coddington network model [168]. This would describe a transition between QH plateaus whose Hall conductances differ by $2e^2/h$. Such a transition requires fine-tuning in conventional quantum Hall systems but here the relevant network model emerges naturally from disorder. A different situation pertains to valley DWs which host counter-propagating modes protected against backscattering by $U(1)_V$ conservation. Microscopic $U(1)_V$-breaking terms (neglected above) could open a gap at such achiral DWs and further lower their energy, leading to an orbital ferromagnetic, valley-disordered ground state with a macroscopically robust QAH. Intermediate scenarios suggest a new type of network model that has both chiral and achiral segments. Understanding the properties of these unusually intricate DW networks is an intriguing open question.

After the initial transport measurements of the QAH in hBN-TBG at $\nu = +3$ [28], magnetometry experiments using a scanning superconducting quantum interference device (SQUID) have confirmed the orbital nature of correlations by detecting a magnetization density of $> 1\mu_{\mathrm{B}}$ per moiré unit cell [169]. The spatial resolution of the probe allows

for imaging of submicron scale domains, whose magnetic response to a chemical potential sweep was attributed to the chiral edge states. Recently, more detailed measurements have revealed an intricate 'Chern mosaic' pattern, as well as hysteresis and anomalous Hall resistivity, at $\nu = +1$ in a device that was not intentionally aligned with the encapsulating hBN [170]. Especially given the observation of significant variations across the sample (which transport studies inevitably average over), this suggests that the DW physics described in this chapter may be locally relevant in wider settings in TBG than originally anticipated[6].

[6]Indeed, the strong coupling analysis predicts (partially) valley polarized $|C| = 1$ states at $|\nu| = 1, 3$ even without the help of an external sublattice coupling.

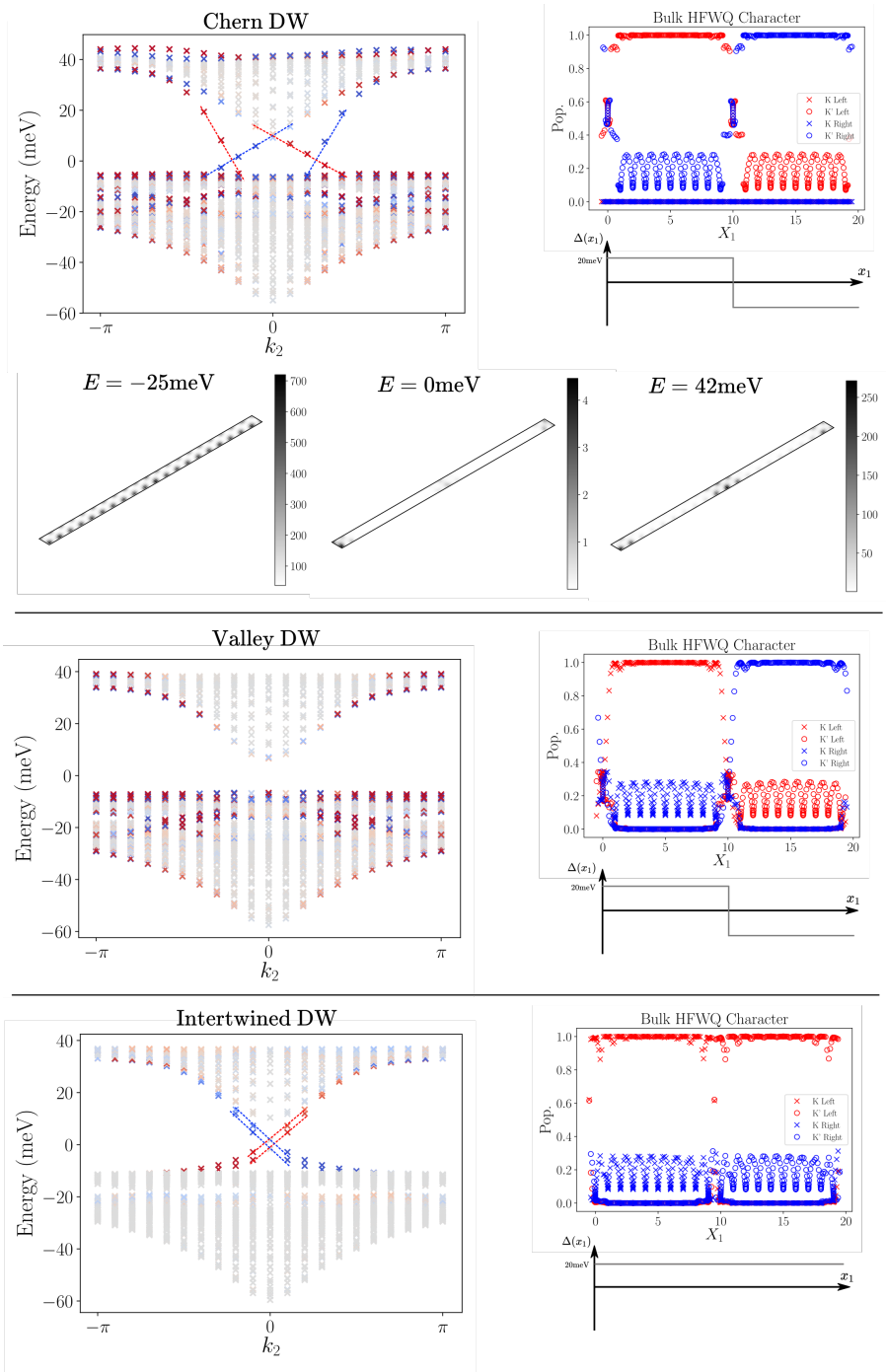

Figure 4.2: HF bandstructure (left of each row) of the three types of DWs organized by momentum parallel to the DW. Points are colour-coded according to the real-space localization of the corresponding HF orbitals (cf. Fig. 4.1). Dashed lines are guides indicating gapless chiral modes. The DW solutions are generated for a given substrate profile (bottom right of each row). Also shown are the overlap of the DW with the HFWQ orbitals (top right of each row), plotted against the average x_1 position (in units of a_M) of the orbitals. K Left, K Right refer to the K-polarized HFWQ basis constructed in a uniform substrate $\pm\Delta_{max}$ respectively, and analogously for valley K'. For the Chern wall, we also show the spatially-resolved spectral function at selected energies; only one moiré cell in the $\boldsymbol{a}_2$ direction is shown as the results are periodic. Darker regions indicate higher weight.

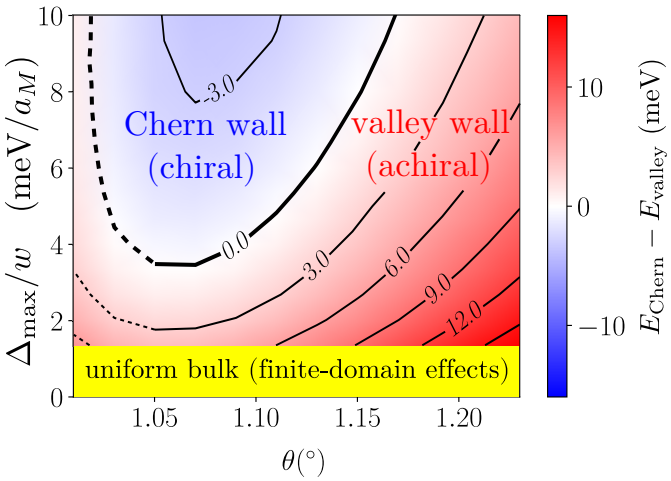

Figure 4.3: Domain wall phase diagram in the twist angle (θ)-substrate gradient ($\Delta_{\max}/w$) plane, as determined by the energy difference of the two HF solutions $E_{\text{Chern}} - E_{\text{valley}}$ plotted as contours. Chern DWs have chiral edge modes whereas valley DWs have achiral modes. Valley DWs are favoured at small $\Delta_{\max}/w$, which allows more texturing and hence reduces the exchange penalty. Contours for $\theta < 1.05^\circ$ are dashed since the gap to the remote bands becomes small enough that treating the remote bands as inert is a poorer approximation. (We take $N_1 = N_2 = 10, 2w = 3a_{\text{M}}$.)

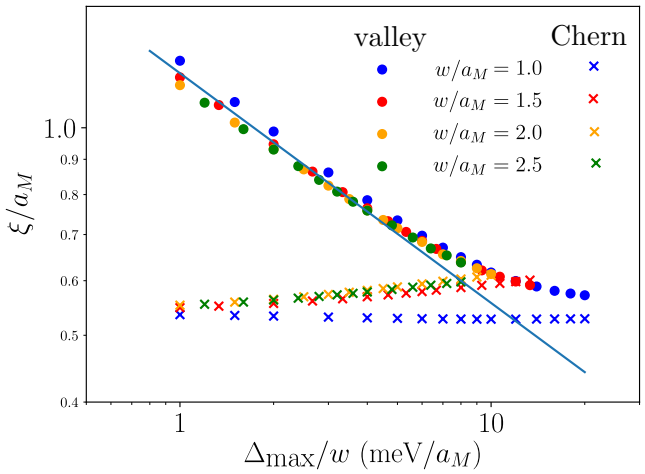

Figure 4.4: Scaling collapse of width ξ of valley (dots) and Chern (crosses) DWs against substrate gradient $\Delta_{\max}/w$ at twist angle $\theta = 1.2^\circ$, for different widths w of the $\Delta(\boldsymbol{r})$ profile. Solid line is the scaling $\xi \sim a_{\text{M}}[\rho_s/(a_{\text{M}}\Delta_{\max}/w)]^{1/3}$. $N_1 = N_2 = 10$.

Chapter 5

Pseudospin skyrmions

The previous two chapters studied how the topological structure of the QAH at $\nu = +3$ in hBN-TBG affected the properties of various neutral excitations. Throughout, the intimate connection to QHFM in LLs provided valuable insights into the physics. Drawing on this analogy further, one naturally expects that the charged excitations also inherit non-trivial topology from the underlying bands. In particular, given the $SU(2)_S$ ferromagnetism, additional charge carriers should enter the QAH as spin skyrmions rather than single spin-flip quasiparticles [80, 171–176].

It will prove worthwhile to embrace the strong coupling framework more fully and consider other filling factors and situations in order to harness richer Goldstone manifolds. Moving away from $\nu = +3$ and removing the sublattice alignment unlocks new soft directions in pseudospin or flavour space, in particular valley and sublattice rotations. These additional degrees of freedom may have subtly different properties than spin—an example is the emergence of merons in quantum Hall bilayers driven by the easy-plane anisotropy in layer space [131]. At charge neutrality and near the chiral-flat limit is where generalized skyrmions have extensive access to the approximate $U(4) \times U(4)$ symmetry of strong coupling TBG. The importance of a detailed understanding of such topological objects is underscored by a recent proposal [56] of purely electronic superconductivity arising from bosonic 'paired pseudospin skyrmions' [177, 178] of charge $2e$, whose stabilization arises from the particular features of the strong coupling Hamiltonian. Such unconventional Cooper pairs may be relevant for understanding the various superconducting domes in TBG [5, 18, 20, 22–26], whose properties and origins remain the subject of intense debate.

However, the investigation of such paired flavour textures has been limited to either analyses of the effective NLSM [56] or numerical studies of a simplified model mimicking the gross features of the central bands [179][1]. While such studies provide qualitative insight, a systematic exploration of these charged textures within a realistic microscopic model of TBG is important for establishing their possible impact in experiments. There is no guarantee that topological textures behave as expected once unavoidable complications such as momentum space structure, finite kinetic energy and the presence of a moiré lattice are accounted for, as exemplified by the topological excitons and domain walls in Chapters 3 and 4.

In this chapter, we present calculations of skyrmions in TBG using self-consistent HF calculations within the interacting BM model [57]. Our goals are to i) provide a proof-of-principle of skyrmions and their pairing in appropriate limits of TBG, ii) investigate whether such pairing can result in superconducting phenomenology consistent with that seen in experiment (in particular the dome-shaped dependence of T_c on twist angle [20], requiring knowledge of the effective mass of paired skyrmions), and iii) establish the regime in parameter space over which pairing survives away from the idealized limit.

In Sec. 5.1, we review the necessary theoretical background of the NLSM and strong coupling picture, complementing the discussion in Sec. 2.3 and 2.4. In Sec. 5.2, we discuss the properties of pseudospin skyrmions at charge neutrality. In Sec. 5.3, we present various extensions, and discuss our results in the context of experiments. We close with an outlook in Sec. 5.4. The work in this chapter is based on Ref. [57].

5.1 Theoretical considerations

5.1.1 Model and strong coupling hierarchy

We first briefly recall some important facts about the interacting Hamiltonian from Sec. 2.2 and 2.3. We ignore the weak relative rotation of the Dirac cones in the two layers so that the PHS $\hat{\mathcal{P}}$ is exact. The chiral ratio κ is a key parameter that controls the properties of the eight central moiré bands, which we project onto. While the ex-

[1] See also more recent microscopic studies in Refs. [180, 181], which are related to aspects of the work presented in this chapter.

perimental relevance of the twist angle θ as a tuning parameter is obvious, it will prove theoretically useful to vary κ away from the physical range $0.5 < \kappa < 0.8$. Gate-screened intravalley interactions are introduced which preserve the global $U(2)_K \times U(2)_{K'}$ symmetry. Subtleties arising from the correct counting of interactions lead to a renormalized one-body term $\hat{H}_{\text{SP}}$ which differs from the BM kinetic dispersion $\hat{H}_{\text{BM}}$. Crucially, the subtraction scheme is not unique, and physical predictions may depend on the choice. Most of the initial discussion of skyrmions will be based on the average scheme, which effectively leads to no corrections when interactions are recast in the strong coupling form analogous to (2.26).

As reviewed in Sec. 2.4, the Chern basis $d^\dagger_\alpha(\boldsymbol{k})$, where α is a composite index for sublattice σ, valley τ and spin s, reveals the topological nature of the central bands which split into Chern quartets with $C = \sigma_z\tau_z$. There exists an approximate hierarchy of scales $U_{\text{S}} \gg U_{\text{A}}, t_{\text{S}} \gg t_{\text{A}}$ (see Sec. 2.4.3 for a discussion of these energy scales)—the purely symmetric $U(4) \times U(4)$ model at the scale U_{S} emerges in the chiral-flat limit where exact generalized ferromagnet ground states at $\nu = 0$ can be constructed. Positive anisotropies J, λ arise from a finite dispersion and chiral ratio respectively. As we are primarily interested in pseudospin physics, we will mostly neglect the spin, resulting in an approximate $U(2) \times U(2)$ subspace (Fig. 5.1a). At neutrality, the orientation of $C = 0$ generalized ferromagnets within this manifold is given by the Chern-filtered pseudospins $\boldsymbol{n}_\pm$ defined in (2.29). Away from the chiral-flat limit, the ground space is resolved as KIVC states with $\boldsymbol{n}_- = -\boldsymbol{n}_+$ lying in-plane.

5.1.2 Non-linear sigma model and pseudospin textures

To understand low-energy excitations and spatially non-uniform configurations, it is useful to consider a continuum NLSM description purely in terms of the pseudospins [56].

The energy functional[2], familiar from QHFM, is

$$E[\boldsymbol{n}_+, \boldsymbol{n}_-] = \int d^2\boldsymbol{r} \left[\frac{\rho_{\rm ps}}{2} \left((\nabla \boldsymbol{n}_+)^2 + (\nabla \boldsymbol{n}_-)^2 \right) \right.$$
$$+ (J+\lambda)\boldsymbol{n}_+ \cdot \boldsymbol{n}_- - 2\lambda n_+^z n_-^z \qquad (5.1)$$
$$\left. + \frac{1}{2} \int d^2\boldsymbol{r}'\, \delta\rho(\boldsymbol{r}) V(\boldsymbol{r}-\boldsymbol{r}') \delta\rho(\boldsymbol{r}') \right]$$

where $\rho_{\rm ps}$ is the pseudospin stiffness in the isotropic (chiral-flat) limit, and $\delta\rho = \delta\rho_+ + \delta\rho_-$ consists of the topological charge (Pontryagin index) densities of the two Chern sectors

$$\delta\rho_\pm(\boldsymbol{r}) = \pm e \rho_{{\rm top},\pm}(\boldsymbol{r}) = \pm \frac{e}{4\pi} \boldsymbol{n}_\pm \cdot \partial_x \boldsymbol{n}_\pm \times \partial_y \boldsymbol{n}_\pm. \qquad (5.2)$$

The skyrmion number is given by $N_{{\rm top},\pm} = \int d^2\boldsymbol{r}\, \rho_{{\rm top},\pm}(\boldsymbol{r})$, where skyrmions and anti-skyrmions have $N_{\rm top} = +1$ and $N_{\rm top} = -1$ respectively.

The NLSM parameters $J, \lambda, \rho_{\rm ps}$ are plotted in Fig. 5.1b[3]. In the 'average' subtraction scheme, the superexchange J has a prominent minimum and nearly vanishes around $\theta \simeq 1.08°$, coincident with where the bare BM bandwidth is smallest. λ is a monotonically increasing function of $w_{\rm AA}$ and is largely insensitive to θ. The pseudospin stiffness $\simeq 1.3\,$meV is a property of the maximally-symmetric manifold and has a very weak dependence on twist angle. While there are sizable regions where $\lambda > J$, this only occurs for the average scheme where J is directly tied to the bare BM scale, which is substantially smaller than the bandwidth obtained via STM measurements of the vHS's in the density of states [38, 41–43, 182]. Therefore we will mostly be interested in the case $J \gtrsim \lambda$ that is conducive to skyrmion pairing as explained below.

Consider first the isotropic limit $J = \lambda = 0$ where the Chern sectors decouple. The ground state at $\nu = 0$ is specified by free choices of uniform pseudospins $\boldsymbol{n}_\pm^0$. An additional charge enters as a $1e$-skyrmion (in one of the Chern sectors) rather than a particle-like excitation if the energy for a well separated skyrmion-antiskrymion pair ($8\pi\rho_{\rm ps}$) exceeds the particle-hole gap ($\Delta_{\rm ph}$). We can use the Polyakov solution [171] which minimizes the gradient energy. Due to the lack of any Zeeman-like term, the skyrmion prefers to

[2]Note that at this level of approximation, the energy functional contains anisotropic couplings betwen $\boldsymbol{n}_+$ and $\boldsymbol{n}_-$, but not anisotropic fields.

[3]The explicit expressions, which are somewhat involved, can be found in Appendix A of Ref. [57].

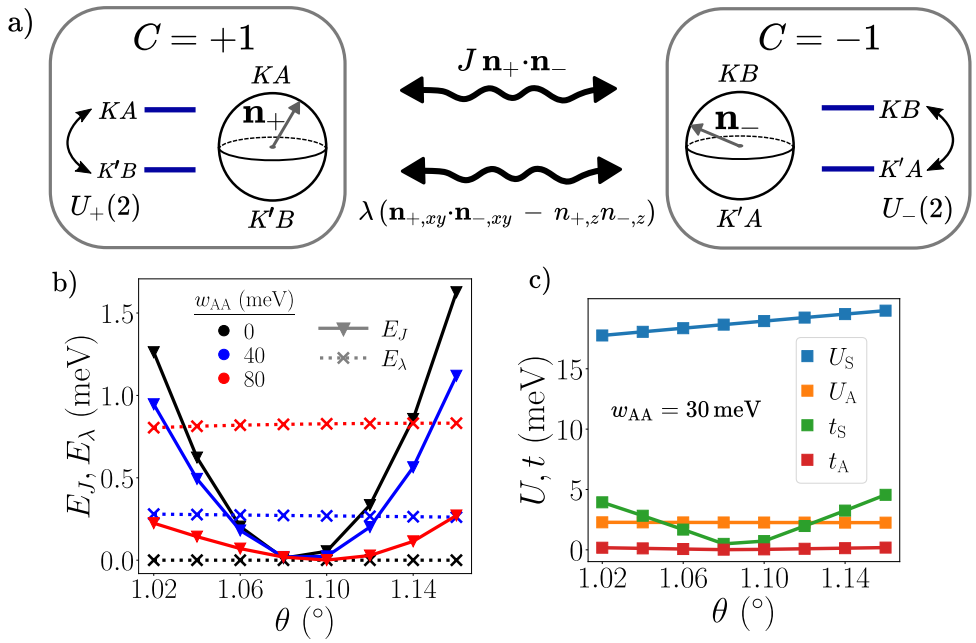

Figure 5.1: a) Schematic of Chern sectors with $C = \pm 1$. In the spinless isotropic limit, there is a $U(2) \times U(2)$ symmetry. At neutrality for a generalized ferromagnet with net $C = 0$, one can define pseudospins $\boldsymbol{n}_\pm$, which are coupled by the symmetry-breaking anisotropies J, λ (wiggly lines). b) NLSM parameters $E_J = JA_{\mathrm{UC}}, E_\lambda = \lambda A_{\mathrm{UC}}$ as a function of twist angle θ and interlayer hopping parameter w_{AA}. The pseudospin stiffness $\rho_{\mathrm{ps}} \simeq 1.5\,\mathrm{meV}$, calculated in the isotropic limit, does not depend on w_{AA} and subtraction scheme, and is largely insensitive to θ. c) Strong-coupling energy scales $U_{\mathrm{S}}, U_{\mathrm{A}}, t_{\mathrm{S}}, t_{\mathrm{A}}$ as a function of θ and w_{AA}. All quantities calculated using the average subtraction scheme.

expand to infinite size to minimize the Coulomb term.

Reintroducing dispersion leads to an effective AFM coupling J, constraining the parent ground state $\boldsymbol{n}_+^0 = -\boldsymbol{n}_-^0$ which now belongs to an $SO(3)$ manifold. A skyrmion of radius R_{s} in say $\boldsymbol{n}_+$ now experiences a Zeeman penalty $\propto R_{\mathrm{s}}^2$ arising from misalignment with $\boldsymbol{n}_-^0$. The skyrmion becomes finite with a size determined from the competition between J and the interaction term. (Note that in order to avoid divergences with system size, the tails of the skyrmion profile must decay faster in space than the Polyakov ansatz [56, 172, 183].) For large enough J, the skyrmion shrinks and crosses over to an ordinary particle-like excitation. Having instead a finite λ leads to similar conclusions, except with a different residual $SU(2)$ manifold. Including both perturbations restricts the insulator to a KIVC parameterized by a $U(1)$ valley angle.

Adding instead a net charge of $|Q| = 2e$ to the system leads to substantially different conclusions. In the scenario with non-zero J, the AFM interaction leads to the pairing of a

skyrmion in $\boldsymbol{n}_+$ with an antiskyrmion in $\boldsymbol{n}_-$ (the total charge is $2e$, a crucial consequence of the opposite assignment of Chern numbers). To see this, note that the AFM inter-Chern coupling is completely satisfied if the two textures are centered at the same position with exactly the same profile such that $\boldsymbol{n}_{\text{pair}}(\boldsymbol{r}) \equiv \boldsymbol{n}_+(\boldsymbol{r}) = -\boldsymbol{n}_-(\boldsymbol{r})$. In this case the resulting 'paired $2e$-skyrmion' dilates without limit to avoid the Coulomb self-energy. Hence an $\boldsymbol{n}_+$-skyrmion and an $\boldsymbol{n}_-$-antiskyrmion will bind for any positive value of J, even though the underlying electron-electron interaction is purely repulsive. A paired skyrmion configuration preserves $\hat{\mathcal{T}}'$-symmetry, which is a useful numerical diagnostic.

In the presence of an additional λ term, the paired skyrmion experiences an energy penalty $\propto R_{\text{s}}^2$ from regions where $\boldsymbol{n}_{\text{pair}}(\boldsymbol{r})$ is not lying in-plane. This not only leads to a finite size, but also elongates the texture somewhat to reduce the area spent pointing out-of-plane. When λ is comparable to J, the texture deforms to resemble the topologically equivalent configuration of two paired $1e$-merons separated by a finite distance. This can be understood as the λ-term shrinking the costly $\boldsymbol{n}_{\text{pair}} \parallel \hat{z}$ regions such that they become the cores of the merons. If λ/J is sufficiently large, pairing is no longer favorable.

5.1.3 Skyrmion superconductivity

We now assume that the microscopic parameters are chosen such that charges enter as skyrmions rather than particles. $1e$-skyrmions from opposite Chern sectors attract to form paired skyrmions. Even if particle excitations are slightly lower in energy, this typically occurs in a small region of the mBZ centered at Γ_{M}. Hence above a critical doping, additional charges are expected to form skyrmions [56].

A non-zero superconducting T_c requires a finite boson effective mass M_{pair}, which can be motivated within the phenomenological picture of a pair of coupled quantum Hall ferromagnets [56] in equal and opposite magnetic fields. A single $1e$-skyrmion feels a net magnetic field and hence has a flat-band dispersion. On the other hand, the magnetic fields experienced by a paired skyrmion cancel out. To understand the generation of an effective mass in this case, imagine a paired skyrmion propagating at some velocity v. The Lorentz forces in the two sectors act to push the constituent $1e$-skyrmions in opposite directions, which is counteracted by a restoring force depending linearly on J

and the separation (λ is assumed small). By balancing the two, one can deduce that M_{pair} is inversely proportional to J. Therefore the paired skyrmions condense with a finite superfluid stiffness and associated Berezenskii-Kosterlitz-Thouless (BKT) transition temperature [184]

$$T_c = \frac{\nu\pi\hbar^2}{2k_B A_{\text{UC}} M_{\text{pair}}} = \frac{\nu J A_{\text{UC}}}{2k_B}. \tag{5.3}$$

We define a corresponding filling-independent energy scale $E_c = k_B T_c/\nu$, which equals $E_J/2$ in this framework. Above, ν should be taken to be the doping relative to the integer filling of interest.

Note the sensitive dependence on the superexchange J, which potentially provides a litmus test for the applicability of this mechanism to realistic samples of TBG. Namely, experiments observe a superconducting dome in T_c as a function of twist angle, which peaks around $\theta = 1.08°$ [20]. The value of J, and indeed the effective mass as computed independently in Sec. 5.2, are also affected by θ through the evolution of the bandwidth and character of the BM bands. However as we discuss later, the precise relationship is subtle and differs based on the choice of interaction subtraction. In particular, while the nature of the ordered normal state at $\nu = 0$ is unambiguous, depending only on the signs of J and λ, finer details such as skyrmion effective masses are susceptible to the specifics of the subtraction scheme.

5.1.4 Numerical methods

Underpinning the discussion in the following sections are explicit mean-field solutions $|\phi\rangle$ for the (pseudo)spin skyrmions, constructed using self-consistent HF calculations. Since such configurations break translation symmetry and flavor rotation symmetries, the HF density matrix takes the most general form

$$P_{\boldsymbol{k}\tau s\sigma;\boldsymbol{k}'\tau' s'\sigma'} = \langle \hat{d}^\dagger_{\boldsymbol{k}\tau s\sigma} \hat{d}_{\boldsymbol{k}'\tau' s'\sigma'} \rangle. \tag{5.4}$$

We take system sizes $L = N_1 = N_2$ throughout so that a non-degenerate moiré band can accommodate L^2 electrons. The filling is fixed by the constraint $\text{Tr}P = (4+\nu)L^2 = (4+\nu_0)L^2 + N$, where ν_0 is the parent integer filling factor and N represents the number

of additional doped electrons. Near $\nu = 0$, we neglect spin for simplicity and hence omit the index s when calculating both skyrmion and particle excitations.

We map real-space images of the pseudospin textures with the 'diagonal' Chern-filtered pseudospin density

$$\boldsymbol{n}_C^{\text{diag}}(\boldsymbol{r}) = \sum_I \langle \hat{\boldsymbol{\psi}}_I^\dagger(\boldsymbol{r}) \frac{1 + C\tau_z\sigma_z}{2} \boldsymbol{\eta} \hat{\boldsymbol{\psi}}_I(\boldsymbol{r}) \rangle \tag{5.5}$$

where $\boldsymbol{\eta}$ is defined in (2.28) and I runs over microscopic sublattice and layer. The net global Chern polarization is defined by the difference in fractional occupation in each Chern sector. Above, the Chern band-filtered real-space creation operator is

$$\left[\hat{\psi}_I^\dagger(\boldsymbol{r})\right]_{\tau\sigma} = \sum_{\boldsymbol{k}} \langle \psi_{\tau\sigma}(\boldsymbol{k}) | \boldsymbol{r}; I \rangle \, \hat{d}_{\tau\sigma}^\dagger(\boldsymbol{k}). \tag{5.6}$$

where $\tau\sigma$ labels the Chern band. However, the in-plane components of (5.5) identically vanish in the chiral limit $\kappa = 0$, where the Chern basis becomes completely sublattice polarized. For example, for the $C = +1$ Chern sector, $n_{+,x}$ and $n_{+,y}$ should measure coherence between the KA and $K'B$ bands, but $[\hat{\psi}_I^\dagger]_{KA}$ ($[\hat{\psi}_I^\dagger]_{K'B}$) is non-zero only when $I = 1A, 2A$ ($1B, 2B$).

To remedy this, we occasionally consider an alternative definition that includes off-diagonal terms in the layer/sublattice degrees of freedom

$$\boldsymbol{n}_C^{\text{off}}(\boldsymbol{r}) = \sum_{II'} \langle \hat{\boldsymbol{\psi}}_I^\dagger(\boldsymbol{r}) \frac{1 + C\tau_z\sigma_z}{2} \boldsymbol{\eta} \hat{\boldsymbol{\psi}}_{I'}(\boldsymbol{r}) \rangle. \tag{5.7}$$

To address the question of the effective mass, we perform variational calculations in the space of states obtained by translating a localized paired skyrmion $|\phi_{\boldsymbol{0}}\rangle$ by all possible moiré lattice vectors $\boldsymbol{R}$ to obtain $|\phi_{\boldsymbol{R}}\rangle$. This defines an effective skyrmion hopping model through the overlaps and Hamiltonian matrix elements of the localized skyrmions

$$\begin{aligned} |\psi\rangle = \sum_{\boldsymbol{R}} c_{\boldsymbol{R}} \, |\phi_{\boldsymbol{R}}\rangle \,, \quad \sum_{\boldsymbol{R}'} [S^{-1}H]_{\boldsymbol{R},\boldsymbol{R}'} c_{\boldsymbol{R}'} = E c_{\boldsymbol{R}} \\ S_{\boldsymbol{R},\boldsymbol{R}'} = \langle \phi_{\boldsymbol{R}} | \phi_{\boldsymbol{R}'} \rangle \,, \quad H_{\boldsymbol{R},\boldsymbol{R}'} = \langle \phi_{\boldsymbol{R}} | \, \hat{H} \, | \phi_{\boldsymbol{R}'} \rangle \,. \end{aligned} \tag{5.8}$$

Due to moiré translation invariance, this is essentially a variational calculation of delo-

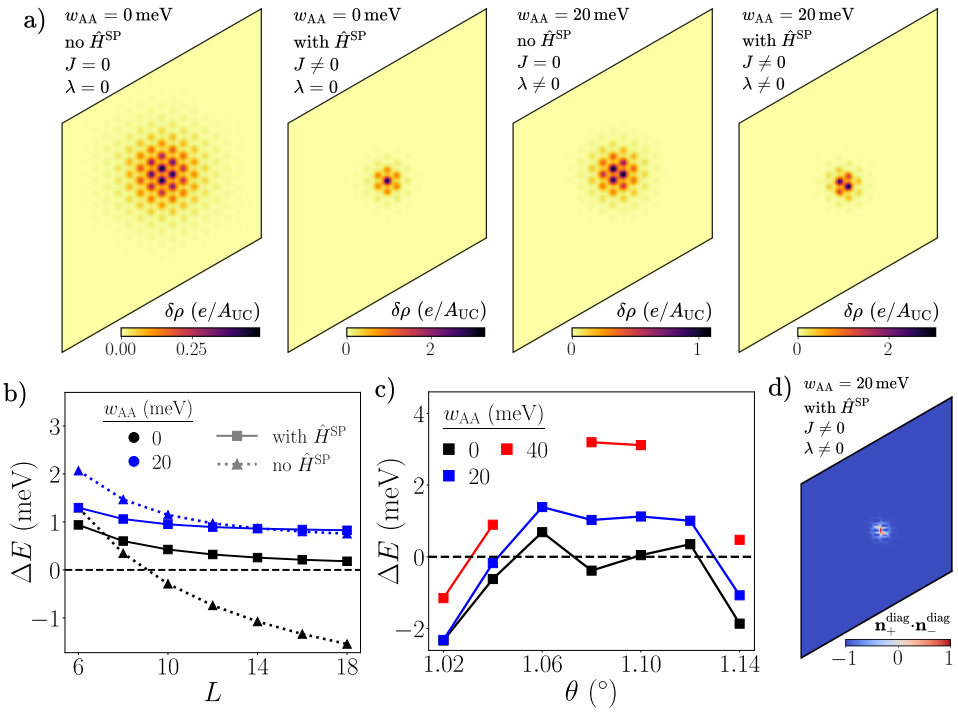

Figure 5.2: a) Charge density $\delta\rho(\boldsymbol{r})$ of $1e$-skyrmions in the entire simulation cell relative to $\nu = 0$ ground state. Panels show different combinations of turning on/off dispersion and achirality, which determine J and λ. Calculations performed on 18×18 systems at $\theta = 1.05°$. Textures manually translated to the center for clarity. b) Relative energy $\Delta E = E_{1e\text{-skyr}} - E_{1e}$ of $1e$-skyrmions (compared to particle excitations) as a function of system size. Apart from the isotropic limit (black triangles), $1e$-skyrmions are not favored. c) ΔE for different θ and w_{AA}. Dispersion is always included. System size is 11×11. Missing data points indicate parameters where HF was unable to find skyrmion solutions. d) Local alignment of Chern pseudospins corresponding to the rightmost panel of a). All calculations used the average scheme.

calized 'Bloch skyrmions' $|\psi_{\boldsymbol{q}}\rangle = \frac{1}{L}\sum_{\boldsymbol{R}} e^{i\boldsymbol{q}\cdot\boldsymbol{R}}\hat{T}_{\boldsymbol{R}}|\phi_{\boldsymbol{0}}\rangle$, with an ideal pseudospin structure at mean-field level. M_{pair} can be extracted from the minimum of the paired skyrmion dispersion $E(\boldsymbol{q})$ in the mBZ. Note that this way of calculating the paired skyrmion mass, which goes beyond mean-field theory, is completely different from the classical calculation of M_{pair} used to obtain the second equality of (5.3).

5.2 Pseudospin skyrmions at neutrality

5.2.1 1e-skyrmions

Fig. 5.2a shows the charge density of a 1e-skyrmion relative to the translation-invariant $\nu = 0$ ground state. The Chern couplings J and λ can be controlled by tuning the effective one-body term[4] and the chiral ratio respectively. Since the Hamiltonian obeys PHS, adding holes instead of electrons leads to analogous results.

In the isotropic limit with $J = \lambda = 0$, the ground state can be any member of the $U(2) \times U(2)$ manifold[5] described by independent choices of $\boldsymbol{n}_+, \boldsymbol{n}_-$. As verified numerically, the extra charge enters as a delocalized skyrmion solely in one of the Chern sectors, while the other sector remains unchanged. Hence its properties are qualitatively the same as for spin skyrmions about the $\nu = +3$ QAH insulator (see Sec. 5.3). Consistent with the absence of anisotropies, the skyrmion expands as much as possible and is only limited by the finite simulation cell. This explains the slow convergence in Fig. 5.2b of the 1e-skyrmion energy $E_{\text{1e-skyr}}$ (measured with respect to the translation invariant 1e-particle excitation energy E_{1e}) with the linear system dimension L compared with other cases. Note that both $E_{\text{1e-skyr}}$ and E_{1e} are many-body energies that are computed self-consistently, and hence account for possible reorganizations of the original $\nu = 0$ insulator induced by the added electron. Fitting to a power law $\Delta E(L) = \Delta E(\infty) + \alpha L^{-\gamma}$, we obtain $\Delta E(\infty) = -4.1\,\text{meV}$, $\alpha = 18.3\,\text{meV}$ and $\gamma = 0.68$. Note that the band gap at $\nu = 0$ depends only weakly on L since there is a direct gap at Γ_{M}. In the NLSM picture, the L dependence is expected to predominantly arise from the system size constraint on R_{s} which controls the interaction contribution to (5.1). Given that the gate screening length is comparable to the moiré length $d_{\text{sc}} \simeq a_{\text{M}}$, one expects $\gamma > 1$ in the continuum limit for $R_{\text{s}} \gg a_{\text{M}}$. The discrepancy suggests that lattice corrections (the dotted patterns in Fig. 5.2a denote the AA-stacking regions) and finite size effects have a quantitative impact here. We find that the centres of the lowest energy skyrmions pin to AB/BA sites. This is reasonable since such a configuration distributes the charge at the core more evenly compared to an AA-centred skyrmion, thereby reducing the Coulomb cost.

[4] In the average scheme, this corresponds to artificially switching off the BM dispersion.

[5] Strictly speaking the $|C| = 2$ ferromagnets are also ground states, but these do not allow for textures.

In the presence of anisotropies, the $1e$-skyrmions become finite-sized. For example in the chiral-nonflat limit with $J \neq 0, \lambda = 0$, the charge density is localized to within a few moiré lengths, leading to faster energy convergence with system size. This is consistent with the intuition from the NSLM, and the energetics of the skyrmion becomes significantly less favourable. The parent insulator is a member of the $SU(2)$ family containing the KIVC and the valley Hall state (e.g. polarizing into KA and $K'A$ bands). The global net Chern polarization is less than $1/L^2$, consistent with the fact that the superexchange tunnels between opposite Chern sectors. The skyrmion is now pinned to the AA sites. This makes sense since the skyrmion is penalized by violations of the J-term at the core, and this centering reduces the number of AA sites which have to pay this cost.

A similar story holds for the nonchiral-flat limit with $J = 0, \lambda \neq 0$, except the $\nu = 0$ insulator now interpolates between the KIVC and the valley-polarized state. This time, the added skyrmion is perfectly Chern polarized. Furthermore, the energy penalty from the anisotropies now occurs away from the skyrmion core, such that the skyrmion returns to AB/BA pinning to reduce the Coulomb energy.

Including both perturbations, which is the case for realistic TBG, the symmetry reduces to the $U(1)$ family of KIVC insulators, and the Chern polarization of the skyrmion is imperfect again. Fig. 5.2d illustrates that the localized violation of Chern anti-alignment occurs at the same position as the charge density modulation, confirming the skyrmionic nature of the added charge. In Fig. 5.2c, we chart the relative energy of the skyrmions as a function of θ for different chiral ratios. For the average scheme, the $1e$-skyrmions are actually most costly near the magic angle where J is suppressed (compare with Fig. 5.1b). This is despite the fact that artificially turning off J while keeping other parameters fixed improves the skyrmion energy significantly (Fig. 5.2b). On the other hand, λ is largely constant as a function of θ. This suggests that the continuum description in terms of a small number of coupling parameters is not completely adequate.

The numerical results for ΔE in any plot such as Fig. 5.2c are generally expected to represent upper bounds for two reasons. First, our calculations are performed on finite system sizes L. In the thermodynamic limit $L \to \infty$, the skyrmions will have some ideal radius $R_{\mathrm{s}}(\infty)$ set by the intrinsic properties of the BM model and interaction potential.

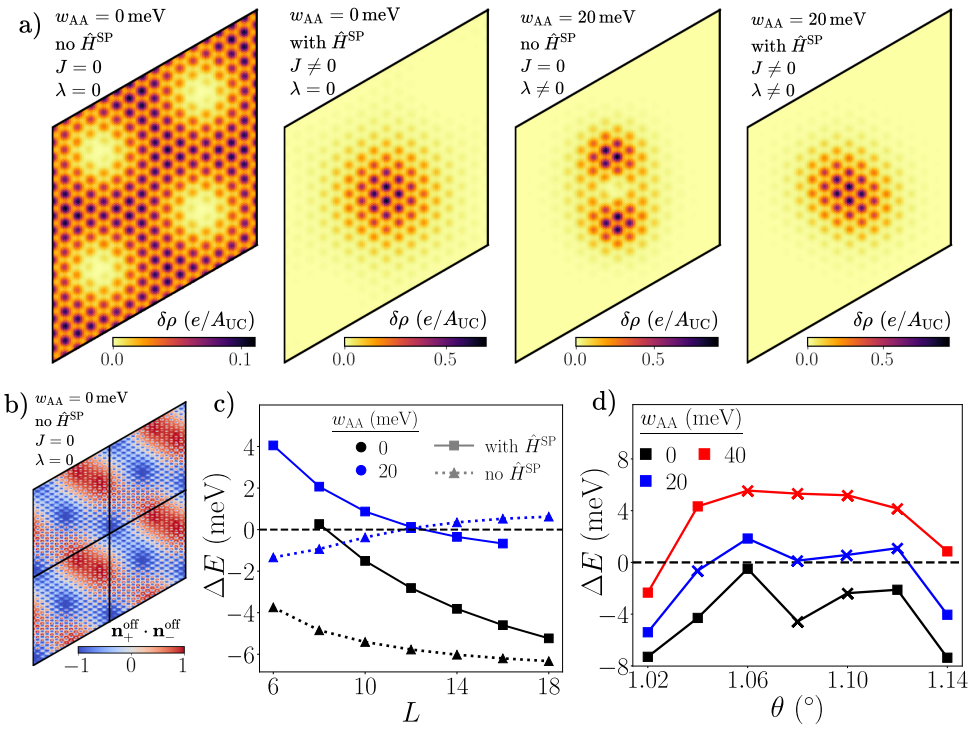

Figure 5.3: a) Charge density $\delta\rho(\boldsymbol{r})$ of $2e$-skyrmions in the entire simulation cell relative to $\nu = 0$ ground state. Panels show different combinations of turning on/off dispersion and achirality, which determine J and λ. Calculations performed on 16×16 systems at $\theta = 1.05°$. Textures manually translated to the center for clarity. b) Local alignment of Chern pseudospins corresponding to the leftmost panel of a). The system cell has been duplicated three times for presentation. c) Relative energy $\Delta E = E_{2e\text{-skyr}} - E_{2e}$ of $2e$-skyrmions (compared to adding two particle excitations) as a function of system size. Both $E_{2e\text{-skyr}}$ and E_{2e} are computed self-consistently. d) ΔE for different θ and w_{AA}. Dispersion is always included. Note that some of the solutions (indicated with crosses rather than squares) for $1.05° < \theta < 1.13°$ are not $\hat{\mathcal{T}}'$-symmetric paired skyrmions. System size is 11×11. All calculations used the average scheme.

Unless $L \gg R_s(\infty)$, the pseudospins in our calculation will experience some degree of frustration from the finite simulation cell, leading to an energy penalty. In addition, a larger L introduces a greater number of basis Bloch states which allows for smoother pseudospin rotations. Second, the restriction to single Slater determinants in HF likely impacts skyrmions more than particle-like excitations. As shown in Sec. 5.2.3, skyrmions can gain a small delocalization energy by going beyond mean-field and restoring the translation symmetry.

5.2.2 $2e$-skyrmions

Fig. 5.3a shows the textured configurations when two electrons are added to the translation-invariant $\nu = 0$ ground state. As before, the Chern couplings J, λ can be controlled through the effective one-body term and the chiral ratio respectively.

For $J = \lambda = 0$, the texture breaks moiré translation symmetry completely, but the charge density appears to spread throughout the system without a clear identification of one or two well-defined objects. Interestingly, the lowest energy solution consists of both additional charges entering the same Chern sector, meaning that from a symmetry standpoint the situation will again be qualitatively similar to adding two charges to the spinful QAH state. As shown in Fig. 5.3b, the pseudospin alignment (note that one Chern sector has a constant pseudospin) rotates in a complicated fashion without reconstructing a new superlattice periodicity. However in analogy to the case of $SU(2)$-invariant spin textures in Sec. 5.3, the inclusion of more doped electrons can result in a so-called 'double-tetarton lattice' [185] with emergent periodicity if they all Chern polarize.

In the chiral non-flat limit with $J \neq 0, \lambda = 0$, the charge density consists of a single smooth modulation with approximate circular symmetry. This is precisely an explicit realization of a *paired* $2e$*-skyrmion*: a skyrmion and an antiskyrmion with identical spatial profiles in the two Chern sectors exactly overlapping. This binding is induced by the superexchange J, as evidenced by the perfect anti-alignment of Chern pseudospins (and hence $\hat{\mathcal{T}}'$-symmetry). In the absence of other perturbations, the paired skyrmion spreads out and is limited only by the system size, leading to slow convergence in Fig. 5.3c. Hence the resulting physics controlling the texture is similar to that of the $1e$-skyrmion in the isotropic limit, and the skyrmions tend to be centred at AB/BA regions.

In the nonchiral-flat limit with $J = 0, \lambda \neq 0$, one may naïvely expect a similar paired skyrmion where the pseudospins are locked instead as $n_{+,z} = n_{-,z}$ and $\boldsymbol{n}_{+,xy} = -\boldsymbol{n}_{-,xy}$. However this does not work as it leads to an electrically neutral object. The numerics reveal that both charges predominantly go into the same Chern sector. For small system sizes, the state closely resembles the double-tetarton lattice of the isotropic limit, which is reflected in the energetic trends in Fig. 5.3c for small L. For larger sizes, the lattice deforms such that the texture is better described by a nearby pair of $1e$-skyrmions. While

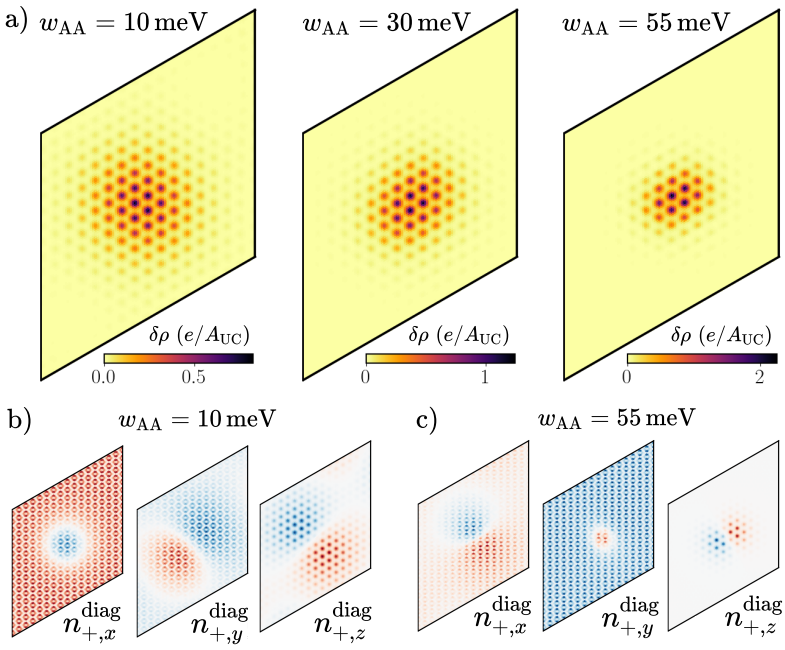

Figure 5.4: a) Charge density $\delta\rho(\boldsymbol{r})$ of paried skyrmions for different w_{AA}. b,c) Local pseudospin orientation in one Chern sector corresponding to first and third panels of a). System size is 16×16 with average scheme.

this may be considered pairing (actually since $\Delta E > 0$, it is a metastable bound state that is unstable towards decaying into two particles), we reserve the term 'paired skyrmion' for the $\hat{\mathcal{T}}'$-symmetric cases where a skyrmion and an antiskyrmion from opposite Chern sectors bind. It is noteworthy that ΔE increases as a function of L, bucking the trends of all other types of $1e$- and $2e$-skyrmions. This occurs because for $L \lesssim R_s(\infty)$, the constituent skyrmions are forced to strongly interact with each other in the confined system area, and may therefore form a delocalized configuration with better energetics.

It is clear from Fig. 5.3c that reintroducing dispersion to the achiral-flat limit is favourable to the textures, which are once again paired skyrmions. The faster convergence of the relative energy with L is a hint that these paired skyrmions are now finite in size. This is clear from Fig. 5.4a, which illustrates that increasing the chiral ratio not only reduces the skyrmion area, but also leads to an elliptical shape. As discussed in Sec. 5.1.2, this could be anticipated from the NLSM analysis which predicts that the λ-term penalizes the pseudospins when they anti-align out-of-plane. This anisotropy is apparent in Fig. 5.4b,c, where $n_{+,z}(\boldsymbol{r})$ has a much tighter profile than $n_{+,xy}(\boldsymbol{r})$. At mean-field level, the orientation of the n_z lobes is very soft, with distinct HF solutions differing

by $\lesssim 10\,\mu$eV. The n_z lobes seem to be pinned at AB/BA regions.

The energetic trends of the $2e$-skyrmions as a function of θ and w_{AA} are shown in Fig. 5.3d. Note that specific to the average scheme, λ significantly exceeds J for a finite region of θ around the flat-band point. Consequently in the range $\sim 1.05°$ to $\sim 1.13°$, the best textured solution has finite Chern polarization and breaks $\hat{\mathcal{T}}'$, and hence is not a paired skyrmion.

5.2.3 Effective mass of paired skyrmions

A key prediction of the NLSM analysis is that paired skyrmions have a finite dispersion [56], which is crucial for generating a finite BKT energy scale E_c for superconductivity. In the NLSM framework, this generation of a finite mass is non-trivial, arising from the interplay between the superexchange J and the contrasting magnetic fields. An important question is how this picture holds up in the periodic moiré setting, where magnetic fields and flat bands are replaced by inhomogeneous Berry curavtures and interaction-renormalized dispersions. We address these issues using the effective hopping model described in Sec. 5.1.4, paying close attention to the dependence on the twist angle θ and subtraction scheme.

In Fig. 5.5a,b, we show the resulting band structure of $1e$-skyrmions and paired skyrmions, measured relative to the energy of the starting texture. The $1e$-skyrmion is characterized by a sharp peak at Γ_{M} and shallow minima near the zone boundaries (the positions of these features may change for larger w_{AA}, but the overall structure remains the same). Usually a large number of overlaps and matrix elements beyond nearest neighbours needs to be computed to converge for a fixed set of parameters.

On the other hand, the paired skyrmions are robustly associated with a broad energy minimum at Γ_{M} and peaks at the zone corners. Typically only matrix elements for distances $\lesssim 2a_{\mathrm{M}}$ need to be computed to accurately describe the properties of the full hopping model. The skyrmion mass M_{pair}, and hence the BKT energy scale E_c, can be estimated by fitting a parabola to the band minimum. This typically leads to T_c of order 1 K. Fig. 5.5c plots the convergence of E_c with system size L, which implies that the finite-size calculations here will typically underestimate the $L \to \infty$ results.

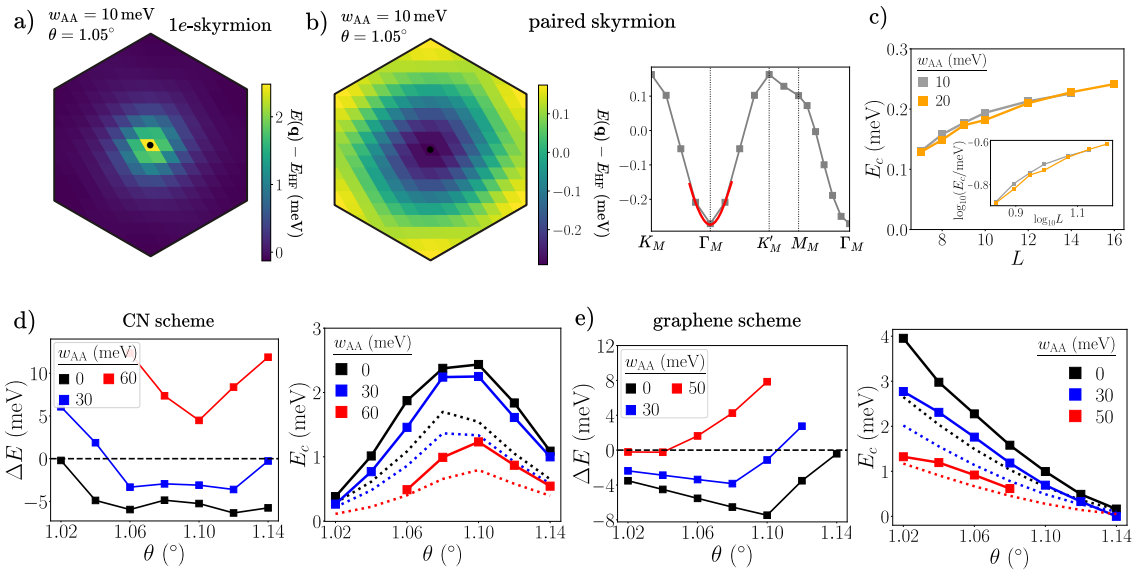

Figure 5.5: a,b) Dispersion of 1e-skyrmion and paired skyrmion respectively in the mBZ, obtained using an effective hopping model. Energy is measured relative to the localized HF solution. Black dot indicates Γ_{M}. For the paired skyrmion, we also show its band structure along a cut in the mBZ. Red line indicates the extraction of the effective mass. System size is 14×14 with average scheme. c) Convergence of the superconducting BKT scale $E_c = \frac{\pi\hbar^2}{2A_{\text{UC}}M_{\text{pair}}}$ for the paired skyrmion with system size, in the average scheme. The effective mass M_{pair} is fitted to the minimum of the skyrmion dispersion. Inset shows log-log plot. d) Left: Paired-skyrmion energy $\Delta E = E_{2e\text{-skyr}} - E_{2e}$ relative to particle excitation as function of θ for different w_{AA} in the CN scheme. System size is 11×11. Right: E_c (solid) extracted from the skyrmion dispersion, compared with the superexchange scale $E_J/2$ (dotted) computed directly from the properties of $\hat{H}$. e) Same as d) except using the graphene scheme.

Having established the basic properties of the hopping model for paired skyrmions, we now turn to details of the dependence of E_c on various parameters. The main motivation is to touch base with experiments which have observed a T_c dome as a function of twist angle [20]. However as noted in Sec. 5.2.2, there is a large window of θ centred at the magic angle where paired skyrmions cannot be found in the average scheme. The utility of this scheme is that J can be easily toggled by artificially turning off the kinetic Hamiltonian, but the drawback is that J therefore becomes substantially smaller than λ when the BM bands are flat, leading to a different type of 2e-skyrmion. To address this issue, we consider now two alternative schemes which are not fine-tuned to have a vanishing superexchange.

Fig. 5.5d charts the relative energy of the paired skyrmion as a function of θ and w_{AA}

for the 'charge neutrality' (CN) scheme. In contrast to Fig. 5.3d, the paired skyrmions are energetically favored in an energy window centered around the magic angle. Again, ΔE has an inverted relation compared to J, which is plotted with dotted lines in the right panel. Note that paired skyrmions can be found up to $w_{\mathrm{AA}} = 60\,\mathrm{meV}$ for $L = 11$, which should improve with increasing system size. Looking at the hopping model results, E_c appears to qualitatively follow the same trends as J for the whole range of twist angles investigated, suggesting that the physical intuition from the NLSM maintains some level of validity in the lattice case. Notably, the CN scheme suggests that a skyrmion superconductor would have a T_c dome around the magic angle.

The graphene scheme in Fig. 5.5e paints a somewhat different picture—E_c monotonically increases in concert with J for decreasing twist angle. For smaller angles the applicability of this calculation will be cut off by the fact that the parent insulator is no longer the ground state. Similarly the paired skyrmions, at least for small chiral ratios, become less favourable compared to particle excitations. Hence it is still possible for the hopping model results in the graphene scheme to be consistent with a T_c dome.

The stability of paired skyrmions in the CN, graphene and average schemes is summarized in Fig. 5.6. Energetically favorable skyrmions can be found up to $w_{\mathrm{AA}} \simeq 50\,\mathrm{meV}$ for the right twist angles in the CN and graphene schemes (this is likely an underestimate when accounting for skyrmion delocalization and finite system size). Beyond this, metastable solutions are obtained for chiral ratios as large as $w_{\mathrm{AA}} \simeq 65\,\mathrm{meV}$. Closer to the upper bound of the realistic values of $w_{\mathrm{AA}} \simeq 80\,\mathrm{meV}$, we find that HF is not able to converge to any paired skyrmion states. In the average scheme, the paired skyrmions are energetically unfavourable close to the magic angle.

It is notable that different subtraction schemes lead to radically different behaviors in E_c[6]. Indeed we believe that this is one of the few cases where such a choice impacts a physical quantity in a qualitative way. Many theoretical studies focus primarily on the type of symmetry-breaking order [58, 77, 78, 81, 83, 85, 86, 92, 95, 96, 186–191]—all the schemes studied here lead to the KIVC which only requires that $J, \lambda > 0$. On the other hand, we are interested in the θ-dependence of E_c which depends sensitively on the value

[6]The origin of this discrepancy can be traced by examining the effective dispersion $\hat{H}^{\mathrm{SP}}$ in more detail [57].

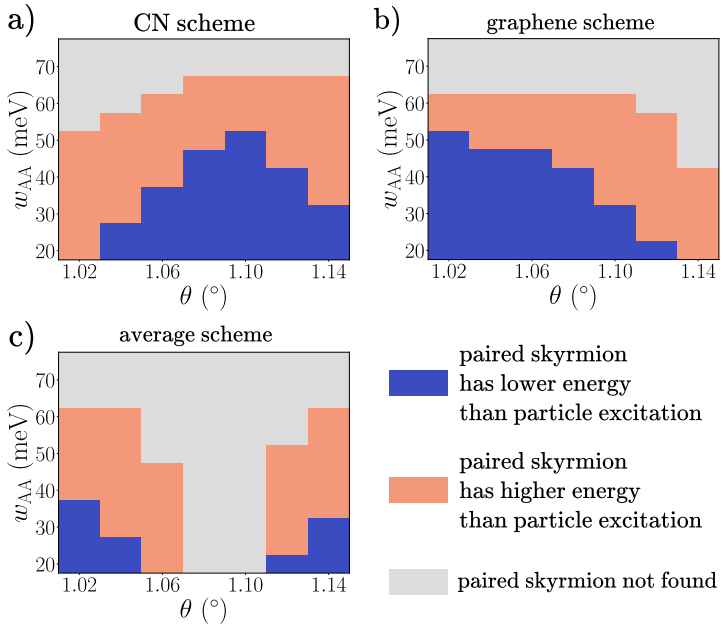

Figure 5.6: a) Phase diagram in the θ vs w_{AA} plane showing where paired skyrmions are energetically favorable (blue) or unfavorable (orange) compared to 2 particle-like excitations about the spinless $\nu = 0$ insulator. Grey indicates regions where HF fails to find a metastable paired skyrmion solution. System size is 14×14 with CN scheme. b,c) Same as a) but with graphene and average schemes.

of J itself.

We reserve judgment on the matter of which scheme is most appropriate for capturing the physics in experimental TBG. Each choice has its own merits and justifications. The average scheme is the simplest and puts the strong coupling hierarchy front and center. The graphene scheme aims to prevent additional renormalizations of the Dirac cones that have already been accounted for in the input value for the bare Dirac velocity. The CN scheme provides a basepoint (i.e. charge neutrality of the BM model) at which the BM kinetic energy is precisely the mean-field band structure. However it is known to lead to incommensurate Kekulé spiral order at extremely small strains for non-zero integer ν [58]. The microscopically correct answer is likely complicated and may differ based on the twist angle itself.

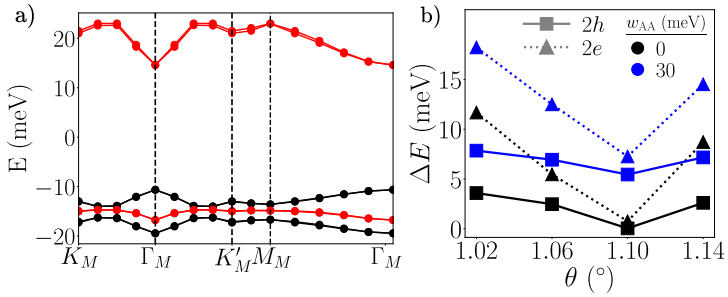

Figure 5.7: a) HF dispersion of spin-polarized KIVC insulator at $\nu = +2$. Red (black) indicates minority (majority) spin carrier. System size is 24×24 with $\theta = 1.06°$. b) Relative energy $\Delta E = E_{2e(h)\text{-skyr}} - E_{2e(h)}$ of $\hat{\mathcal{T}}'$-symmetric paired $2e$- and $2h$- skyrmions about $\nu = +2$. Note sharp minimum of unfilled band at Γ_M. System size is 11×11 with CN scheme.

5.3 Extensions and discussion

5.3.1 Other fillings

We now reintroduce spin and turn to filling factors near $|\nu| = 2$ where the mean-field ground state is also a KIVC insulator (we only show results for $\nu = +2$, but the situation at $\nu = -2$ can be inferred from PHS). A representative member of the spin-degenerate manifold of states, arising from the approximate $SU(2)_K \times SU(2)_{K'}$ symmetry, consists of fully filling the spin-↑ flat bands while forming a spinless KIVC in the (minority) spin-↓ subspace. We concentrate on pseudospin skyrmions by enforcing collinear spins.

Paired skyrmions can be constructed as before by treating the majority spin bands as spectator bands and performing non-trivial pseudospin rotations in the half-filled minority spin bands, but there are complications compared with the spinless neutrality case. First, the NLSM parameters J, λ reflect the relevant energy scales at the neutrality point of the strong-coupling Hamiltonian. However the starting insulator now contains additional majority carriers, which impacts the effective energetics of the minority subspace. Second, this additional interaction renormalization enters in a particle-hole asymmetric way. Generally the bands away from neutrality have a significantly enhanced bandwidth with a prominent extremum at Γ_M [35, 87–90, 192] (Fig. 5.7a), which disfavors skyrmions because they are built from momentum states throughout the mBZ. Third, the edge of the majority spin bands can lie inside the minority band gap which reduces the gap to particle-hole excitations. On the other hand, a pseudospin skyrmion cannot be formed

by adding holes to a completely filled spin sector. This is reflected in the HF calculations in Fig. 5.7b at $\nu = +2$, showing that paired $2e$-skyrmions on the electron-doped side are more expensive than paired $2h$-skyrmions on the hole-doped side. Overall the relative energies ΔE are less favorable than the results at charge neutrality.

We also briefly discuss spin textures near $\nu = +3$ that arise from doping the Chern-, spin-, and valley-polarized QAH. The situation here is significantly simpler because of the $SU(2)_S$ spin-rotation symmetry that holds independent of the presence of dispersion or deviation from the chiral limit. The low-energy charged topological excitations are expected to be spin skyrmions [175, 179, 185] in the partially filled Chern sector without any texturing in the fully filled Chern sector. In the HF numerics, there is again a clear preference for skyrmion formation when doping towards instead of away from neutrality due to the interaction renormalization of the band structure. The $1h$- and $2h$-skyrmions look similar to the pseudospin skyrmions in the chiral flat limit (Fig. 5.2a and 5.3a), since the relevant Goldstone manifolds are $SU(2)$ without anisotropies. Doping additional charges can lead to skyrmion crystals with a new superlattice periodicity [57, 185].

Motivated by the particular physics and questions relevant to TBG, we have so far imposed restrictions on the directions in flavor space that the skyrmions are allowed to rotate in. The strong-coupling insulators at different integer ν are all Chern ferromagnets, and starting from the fully symmetric limit, one can consider more general skyrmions where the only constraint is that locally the state is polarized within the Chern sectors. For instance, starting from the $\nu = +3$ QAH, it is possible to form a texture in both spin and pseudospin to create an 'entangled' skyrmion, akin to what happens at $|\nu| = 1$ in the zeroth LL of monolayer graphene [193]. With the full Hamiltonian, pseudospin rotations will be gapped since the QAH is easy-axis, while spin rotations remain low-energy due to the $SU(2)_S$-symmetry.

These considerations can be generalized to any integer filling. Starting from a generalized ferromagnetic insulator with $\tilde{\nu}_C$ filled bands in Chern sector C, the local flavor configuration is parameterized by two matrix spinors $f_C(\boldsymbol{r})$ living in Grassmannian projective spaces [194]

$$f_C(\boldsymbol{r}) \in \frac{SU(4)}{SU(\tilde{\nu}_C) \times SU(4 - \tilde{\nu}_C) \times U(1)} \tag{5.9}$$

where $\tilde{\nu}_+ + \tilde{\nu}_- = \nu$. The factors in the normal subgroup represent unitary rotations within the filled bands, unfilled bands, and the phase difference between the filled and unfilled bands respectively. The presence of four flavors and two spinors leads to a large manifold of skyrmions. The leading corrections from the $U(4) \times U(4)$ limit will be anistropic *couplings* between the spinors, while additional single-particle perturbations such as substrate coupling may manifest as anisotropic *fields*. The relevant space of textures will be dictated by the energetics at a given filling.

5.3.2 Detecting skyrmions

The presence of spin textures about the QAH at $\nu = +3$ could be detected by measuring the degradation of magnetization for small dopings, e.g. through NMR measurements [195], NV center magnetometry, or using a SQUID [169]. However there is an orbital contribution from the spontaneous Chern polarization which is likely larger than the spin contribution [169]. A more direct probe would be spin-resolved STM near impurity sites that could pin a localized skyrmion.

Measuring pseudospin textures at even integer filling is trickier since experimental techniques are not able to directly couple to the valley degree of freedom. IVC generally leads to $\sqrt{3} \times \sqrt{3}$ spatial order at the microscopic graphene scale, but the $\hat{\mathcal{T}}'$-symmetry of the KIVC insulator means that it does not exhibit a Kekulé *density* distortion (KD) [196, 197]. Paired skyrmions preserve $\hat{\mathcal{T}}'$ and hence do not give rise to KD [197]. They may still leave a dipole-shaped fingerprint in sublattice polarization within regions where the state is locally in the valley Hall configuration, i.e. pseudospins anti-aligned and pointing along the z-axis (Fig. 5.4c), but this is likely a faint signature since away from the chiral limit the Chern basis is only partially sublattice polarized. On the other hand, $1e$-skyrmions are tightly localized within a few moiré lengths and give rise to a spatially varying KD when pinned by charged impurities. KD has been observed in the related context of QHFM within the lowest LL of monolayer graphene [198–200], including the imaging of an individual valley skyrmion [199]. We caution that KD in TBG has also been predicted for incommensurate Kekulé spiral order in the presence of a small amount of strain [58, 197] (see Chapter 6).

5.3.3 Skyrmion superconductivity

We finally turn to the implications of our results for skyrmion superconductivity. First, note that two important factors controlling the feasibility of this proposed mechanism are the stability of paired skyrmions (i.e. relative energy ΔE compared to particle excitations) and their effective masses. In general, we can conclude that paired skyrmions are especially favored close to the strongly-interacting isotropic limit. The realistic value of w_{AA} lies in the range $55-90\,\mathrm{meV}$ (i.e. $\kappa \simeq 0.5-0.8$) and we only find paired skyrmions in the lower range of these values (Fig. 5.6). A mechanism has been proposed that might drive a downward renormalization of the chiral ratio κ [74]. We note also that large skyrmions, which are relatively classical and relevant for small w_{AA}, are likely to be well captured in our mean-field treatment. However, for larger w_{AA}, the paired skyrmions become smaller and quantization effects are more important, and fluctuations can be more significant. In this regime the mean-field result is really only an upper bound on the skyrmion energy, which could be lowered by fluctuations that are not expected to substantially affect the single-particle excitations.

Our numerics find that enhancing interactions by suppressing screening, either through increasing the gate distance d_{sc} or decreasing the permittivity ϵ_r, also favours skyrmions. However, this observation makes the superconducting domes that persist in Refs. [18, 23–25] upon reducing the interaction strength difficult to reconcile with a topological mechanism. In these experiments, the insulators at integer ν, from which the skyrmions would be seeded, disappear with increasing screening. The superconducting region can also straddle the integers where the BKT transition temperature from (5.3) seemingly vanishes. We find that substrate coupling rapidly destroys pseudospin skyrmions, consistent with the absence of superconductivity in aligned samples [27, 28]. This topological mechanism would not be effective in other moiré platforms that lack $\hat{C}_{2z}$-symmetry [56, 143, 145–147]. Heterostrain takes the system away from the strong-coupling regime[7] and similarly disfavors skyrmions in numerics: for instance, the parent insulator has been predicted to give way to a symmetric semimetal at charge neutrality or an incommensurate Kekulé spiral at non-zero integer fillings [58, 97]. Hence the general expectation from our work

[7] The effects of strain will be comprehensively studied in Chapter 6.

and from these experimental observations is that skyrmion superconductivity is most likely to emerge in 'pristine' samples with minimal screening.

The question of effective masses (and hence T_c via (5.3)) is more subtle. We have demonstrated that the dependence of the BKT transition scale E_c on θ is rather sensitive to precise details of how electron interactions are incorporated. Without further external inputs, e.g. from detailed *ab initio* studies or spectroscopic probes of the band structure over a range of twist angles, it is difficult to make quantitative contact with experiments such as Ref. [20] which show a dome in T_c near the magic angle. Any comparison would also inevitably be complicated by the presence of confounding variables such as twist angle disorder [30] which are difficult to fully characterize, let alone control. However, what we *can* reliably distill from our numerical study is that paired skyrmions can in principle emerge with a sufficient mass to support an estimate of $T_c \lesssim 5\,\mathrm{K}$ that is comparable to experimentally observed values. Both the CN and graphene schemes are able to support a non-vanishing superfluid velocity at the magic angle, and the fragility of the parent correlated insulators to deviations of θ will tend to also reduce the strength of skyrmion superconductivity away from this regime.

Another potential challenge to the applicability of the skyrmion mechanism to TBG lies in the fact that superconductivity is most frequently observed near $\nu = -2$ on the side *away* from charge neutrality. On the other hand, our numerics show that paired skyrmions are relatively harder to stabilize at $|\nu| = 2$ compared to $\nu = 0$ (Fig. 5.7b). Furthermore, the skyrmions are more disfavoured when doping in the direction away from charge neutrality. This latter observation can be explained by the increased dispersion due to the interaction renormalization from the extra filled bands (Fig. 5.7a), and has been argued to be consistent with the asymmetry of the Landau fans [87].

5.4 Outlook

In this chapter, guided by intuition from QHFM and the NLSM [56], we have investigated (generalized) skyrmions of the strong coupling insulators using microscopic HF calculations of the interacting BM model [57]. Of special focus was the pairing of pseudospin skyrmions at even integer filling. Our analysis provides clear evidence that skyrmion pair-

ing can indeed occur in microscopically faithful treatments of TBG, thereby illustrating that a purely electronic "topological" Cooper pairing mechanism can operate away from the exactly-solvable limit without leveraging any approximate sigma-model description. However, despite this in-principle demonstration of the feasibility of a novel pairing mechanism, we cannot on the basis of present evidence definitively attribute superconductivity in TBG to this mechanism. This is highlighted by the difficulty in reconciling the deleterious effect of variations in strain, interaction screening, and deviation from the chiral limit on the stability of skyrmions with the apparent robustness of superconductivity to such effects.

Despite this, the uncertainty of various microscopic parameters and the mean-field nature of our study leave open a real possibility that a skyrmionic mechanism may ultimately survive these challenges. We cannot rule out a scenario where skyrmion superconductivity is operative in only a subset of samples, for instance the device studied in Ref. [26] which is nominally non-aligned with hBN and exhibits an remarkably large number of correlated insulators and superconducting domes, including near neutrality. Another moiré material where the skyrmion mechanism may be a plausible explanation of superconductivity is mirror-symmetric magic-angle TTG, which is closely related to TBG but has a somewhat larger value for the magic-angle [201]. Interestingly, the superconductor in TTG is observed to have a very short coherence length [202], and an associated pseudogap regime [19]. Partly because of this, Refs. [19, 202] suggested that part of the TTG superconducting dome is in the BEC regime. Skyrmion pairing is a natural way to get preformed charge-2e bosons, and is at least known to give rise to superconductivity in the chiral limit of TBG [80]. It is therefore worthwhile to investigate whether this mechanism can explain at least a subset of the experimental observations in TTG.

We remark on the qualitative agreement of the paired skyrmion mass (Fig. 5.5d,e) between our effective hopping model and the NLSM, which is surprising given the stark differences in the two approaches. The NLSM utilizes a semiclassical picture that involves relative deformations in the two Chern sectors. On the other hand, our variational Bloch skyrmions maintain perfect pseudospin anti-alignment even for non-zero $\boldsymbol{q}$, owing to the $\hat{\mathcal{T}}'$-symmetry of the mean-field solution $|\phi\rangle$. It is possible that introducing deformations to the input localized skyrmion will improve the energetics and further renormalize the ef-

fective mass. One can consider the following generalization of our calculation that would account for this. The Bloch skyrmions $|\psi_{\boldsymbol{q}}\rangle = \frac{1}{L}\sum_{\boldsymbol{R}} e^{i\boldsymbol{q}\cdot\boldsymbol{R}}\hat{T}_{\boldsymbol{R}}\,|\phi_{\boldsymbol{q}}\rangle$ are still constructed as plane-wave superpositions of a Slater determinant. However, the energetic optimization is performed on the final Bloch skyrmion energy. Hence the intermediate localized state $|\phi_{\boldsymbol{q}}\rangle$ is generally $\boldsymbol{q}$-dependent and not a self-consistent mean-field solution. This procedure is significantly more challenging to carry out since there is no self-consistency property to exploit, and $|\phi_{\boldsymbol{q}}\rangle$ generally involves a many-body reconstruction of the starting insulator. In the absence of such a computation, we believe that the effective hopping model currently provides the most concrete estimate of the effective mass. This is especially true in the physically relevant regime of intermediate chiral ratios κ, where the semiclassical intuition leveraged in the NLSM approach loses its justifcation due to factors like the increased band dispersion and Berry curvature modulation.

Part II

From strong to intermediate coupling

Chapter 6

Incommensurate Kekulé spiral

The popular strong coupling picture of TBG is conceptually appealing, and forms the basis of the various topological excitations presented in the previous chapters. While this framework provides candidate explanations for many empirical observations, there are inconsistencies with many aspects of the experimental phenomenology. This is not surprising given the heterogeneous collection of experimental results on this material—no single theory could possibly account for the often contrasting behaviours across different samples. The most salient example of sample-to-sample variations is the nature of the ground state at charge neutrality, which is predicted to be a robust insulating KIVC within the strong coupling persepctive [78, 83]. While some groups indeed detect a clear gap [15, 23, 26–28, 32, 35, 48], most observe semimetallic or metallic behaviour [4, 5, 16, 20, 22, 24, 25, 29–31, 34, 50], a conflict which cannot be fully resolved by considering alignment with the hBN substrate.

Motivated in part by the conundrum above, we return to the question of the parent correlated states of TBG in this chapter. In particular, we focus on the candidate normal states at integer fillings. While the scope may seem rather restrictive, the nature of the commensurate states is expected to provide insights into other regions of the phase diagram. The cascade transitions and Landau fans suggest that the integer orders control the properties of the Fermi surface and its quasiparticles at non-integer doping. Furthermore, the proximity of correlated insulators and superconducting domes hints at their possible relationship. A better handle of the correlated normal states would provide guidelines as to the mechanisms that aid, or perhaps hinder, superconductivity in TBG.

At the very least, it would be useful to consolidate our understanding of the connections between theory, which has much to say about correlated insulators, and experiments.

In our quest to go beyond the well-established boundaries of the strong coupling framework, we turn to heterostrain, an unintentional perturbation which has been experimentally demonstrated to be ubiquitous across TBG samples [38, 41–43], and theoretically proposed as the key ingredient in recovering a semimetallic state at neutrality [97]. We perform a comprehensive mean-field analysis of TBG at all integer ν, and find that strain dramatically alters the phase diagram by stabilizing an incommensurate Kekulé spiral (IKS) order at non-integer fillings. The defining feature of the IKS is translation symmetry breaking (TSB) that manifests at both the moiré and the microscopic graphene scale. In contrast to the strong coupling insulators, the IKS is driven by momentum-resolved features of the (interaction-renormalized) dispersion, and is more appropriately described as belonging to the *intermediate coupling* regime. We argue that the IKS complements the properties of the strong coupling ferromagnets in several ways, and helps bridge the gap between theory and experiments.

In Sec. 6.1, we elaborate on the motivation and prior theory regarding the integer states. We also flesh out the role of strain and its implementation within the continuum model. To help orient the reader in later sections, we provide an overview of the numerical phase diagram. Sec. 6.2 presents a detailed exposition of the properties of the IKS at $|\nu| = 2$. Sec. 6.3 deals with the analogous states at odd integer fillings. We briefly cover some subsidiary topics, such as disorder and non-integer dopings in Sec. 6.4, and discuss strain and the IKS within the backdrop of experiments. We close with an outlook in Sec. 6.5. The work in this chapter is based on Ref. [58].

6.1 Background

6.1.1 Motivation

At first sight, the phase diagram of TBG resembles that of the cuprate high-temperature superconductors, with electrostatic gating playing the role of chemical doping. This prompted initial attempts to model correlation effects within a single-band Hubbard

model for electronic states localized to a triangular moiré superlattice. Although this approach has proven fruitful in studying moiré heterostructures of MoS_2 and other transition-metal dichalcogenides [203], its applicability to TBG is limited by the fragile topology of the BM bands [44–46]. The latter requires that the simplest tight-binding model that faithfully captures the symmetries of TBG involves a pair of crystallographically-inequivalent Wannier orbitals centered on sites of a honeycomb lattice, but with their charge densities peaked on a triangular lattice formed by the centers of its hexagons [44, 65, 72]. A corollary of this Wannier representation is that it implies extended interactions and a higher degree of itineracy than can be captured via a minimal honeycomb lattice Hubbard model with on-site repulsion and nearest-neighbor hopping.

The utility of a Hubbard description is further challenged by the early experimental observation of a QAH resistance in hBN-TBG at $\nu = +3$. One explanation of this phenomenon invokes a compelling analogy to the *other* paradigmatic setting for strong correlations: the celebrated LLs of an electron in a magnetic field. By fully polarizing in spin and valley, the system minimizes its interaction energy by virtue of Pauli exclusion, and opens a topological charge gap due to the non-trivial topology (made explicit by the sublattice coupling to the substrate) of the underlying bands. A similar QAH state was also observed at $\nu = 1$ [48]. While the formation of such orbital Chern insulator states can in principle be captured within a Hubbard description [204], the close parallels to quantum QHFM [131, 172, 205] has motivated a distinct perspective, where TBG is viewed as a generalized multicomponent quantum Hall system. This naturally explains both the observed QAH response as well the propensity for insulating states at commensurate filling, and motivates a sigma model description based on a hierarchy of perturbations around a hidden limit with $U(4) \times U(4)$ symmetry [78, 83, 92]. The picture, which we have referred to as the strong coupling approach throughout this thesis, receives further experimental support by the observed stabilization of QAH insulators[1] with Chern numbers $C = \pm 3, \pm 2, \pm 1$ at $\nu = \pm 1, \pm 2, \pm 3$ on applying a small out-of-plane magnetic field, even in the absence of substrate alignment [32, 33, 48–50].

However, the TBG bands nevertheless retain features absent in LLs. For instance,

[1] Strictly speaking, these are not anomalous since they only emerge in a finite magnetic field. However the small fields required (significantly smaller than $\sim 10\,\mathrm{T}$ corresponding to one flux per unit cell) suggest that these Chern states remain competitive at zero field.

their dispersion (though small) remains nonzero, and is enhanced when perturbations such as strain are included. Such effects are likely important in giving an accurate description of experimental samples. As a case in point, even at commensurate fillings some experiments report insulators with Chern numbers that cannot be captured in the QHFM picture [35, 48]. Moreover, in contrast to the predictions of the strong coupling framework, most experiments only observe robust correlated insulators at $|\nu| = 2$ and 3, while at neutrality and $|\nu| = 1$ they usually see evidence of a semimetallic or metallic state. This suggests that departures from the flat band/QHFM limit are non-negligible and that the competition between itineracy and localization characteristic of Hubbard physics remains relevant to TBG.

Given its enticing position at the intersection of two dominant themes of strong correlations, it is natural to conjecture that orders that are natural from both perspectives could be particularly robust candidate ground states in TBG. One example (and our focus here) is furnished by states with TSB, which emerge in relatively well-understood limits of both the Hubbard and quantum Hall settings. The formation of charge and/or spin stripe order is believed to be a near-universal consequence of hole-doping the cuprates away from commensurate filling: while purely on-site Hubbard repulsion favors phase separation, the inevitably present further-neighbour interactions frustrate this in favor of spatially-ordered phases [206–218]. For similar energetic reasons a variety of stripe and bubble phases are known to be competitive ground states in high Landau levels [219–222]: phase separation is driven by exchange physics and frustrated by Hartree contributions. As noted above, any Hubbard description of TBG must involve substantial further-neighbour interactions. Meanwhile, single-particle corrections and Hartree renoralization can significantly perturb the flat band limit, penalizing full occupation of the mBZ. Since exchange interactions still favor insulating behaviour, one resolution is to reconstruct the bands via finite-wavevector ordering. Thus, from both points of view, it appears that conditions in TBG might favour TSB states over their competitors.

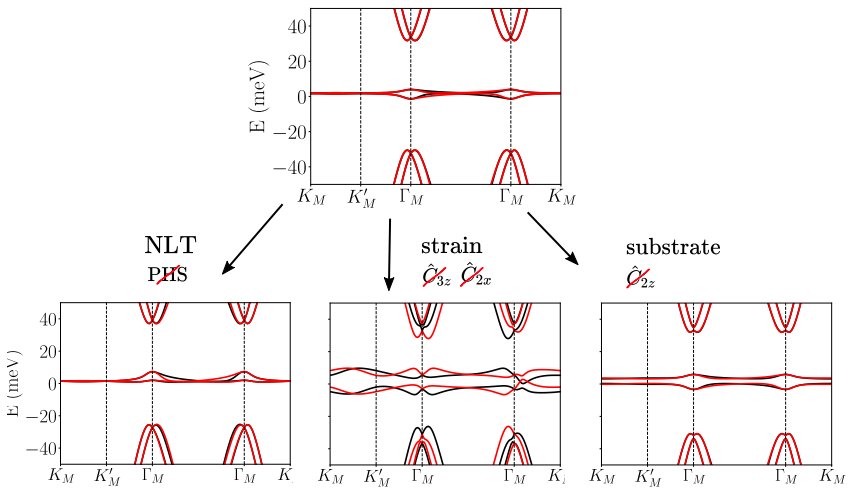

Figure 6.1: The presence of non-local tunneling, strain and substrate potential breaks various symmetries and affects the BM dispersion.

6.1.2 Strain and numerical modelling

In this chapter, we explore TSB order at commensurate integer fillings in TBG. The fundamentals of our numerical method[2]—completely general self-consistent Hartree-Fock analysis of the (spinful) interacting BM model—have already been discussed in previous chapters (see Sections 2.3, 4.2.1, and 5.1.4). Our analysis here incorporates three experimentally important deviations from the original version of the BM model: a $\hat{C}_{2z}$-breaking substrate potential (extensively discussed in Chapters 3 and 4), $\hat{C}_{3z}$-breaking strain, and non-local tunneling.

6.1.2.1 Heterostrain

Uniaxial strain of strength $\epsilon = 0.1 - 0.7\%$ is observed in many TBG samples using STM/STS [41–43, 223]. At charge neutrality, this small strain is believed to be an important driving force behind the weakening of symmetry-broken insulators found in numerics at zero strain in favour of semimetallic phases [77, 97, 187]. In the context of van der Waals homobilayers, it is useful to distinguish between homostrain, where strain is applied identically to both layers, and heterostrain, where the layers are strained oppositely. Since homostrain, to first order, does not account for the experimentally

[2]For most calcuations, we use the parameters $w_{\mathrm{AA}} = 82.5\,\mathrm{meV}$, $w_{\mathrm{AB}} = 110\,\mathrm{meV}$, $\theta = 1.08°$, $\epsilon_r = 10$, and dual gate screening length $d_{\mathrm{sc}} = 25\,\mathrm{nm}$. Interactions are incorporated using the graphene scheme.

observed distortion of the moiré lattice, and has a substantially smaller impact on the electronic structure [224], we focus on heterostrain [97, 225], which is believed to be experimentally relevant.

The moiré geometry is deformed depending on the value of the strain ratio ϵ and strain angle φ with respect to the x-axis. The orthogonal direction is also stretched/compressed due to the Poisson ratio $\nu_{\mathrm{P}} \simeq 0.16$ [226]. Following Refs. [97, 225], the effect of uniaxial strain on the unstrained graphene lattice vectors $\boldsymbol{r}$ and RLVs $\boldsymbol{g}$ is expressed through layer-dependent transformation matrices M_l

$$\begin{gathered}
\boldsymbol{r}_l = M_l^T \boldsymbol{r}, \quad \boldsymbol{g}_l = M_l^{-1} \boldsymbol{g} \\
M_l \simeq 1 + \mathcal{E}_l^T \\
\mathcal{E} \simeq R(\theta) - 1 + S(\epsilon, \varphi) \simeq \begin{pmatrix} \epsilon_{xx} & \epsilon_{xy} - \theta \\ \epsilon_{xy} + \theta & \epsilon_{yy} \end{pmatrix}, \\
S(\epsilon, \varphi) = R^{-1}(\varphi) \begin{pmatrix} -\epsilon & 0 \\ 0 & \nu_{\mathrm{P}} \epsilon \end{pmatrix} R(\varphi)
\end{gathered} \tag{6.1}$$

where $R(\theta)$ is a rotation matrix. Heterostrain constrains the parameters to satisfy $\theta_1 = -\theta_2 = \theta/2$, $\varphi_1 = \varphi_2 = \varphi$, and $\epsilon_1 = -\epsilon_2 = \epsilon/2$. To first order in ϵ and θ, the twist angle is unaffected. In analogy with the pure twist case (2.14), the new moiré RLVs are, in terms of the monolayer RLVs[3],

$$\boldsymbol{b}_1 = (M_1^{-1} - M_2^{-1})(\boldsymbol{b}_{G2} - \boldsymbol{b}_{G1}), \quad \boldsymbol{b}_2 = (M_1^{-1} - M_2^{-1}) \boldsymbol{b}_{G1}. \tag{6.2}$$

This will affect the sampling of the long-range interaction on the momentum grid.

The strained and rotated intralayer kinetic term in valley τ becomes

$$\langle \boldsymbol{k}, l | \, H_{\mathrm{BM}} \, | \boldsymbol{k}', l \rangle = \hbar v_F \left[M_l(\boldsymbol{k} - \tau \boldsymbol{A}_l) - \boldsymbol{K}_\tau \right] \cdot \begin{pmatrix} \tau \sigma_x \\ -\sigma_y \end{pmatrix} \delta_{\boldsymbol{k}\boldsymbol{k}'} \tag{6.3}$$

$$\boldsymbol{A} = \frac{\beta}{2a} (\epsilon_{xx} - \epsilon_{yy}, -2\epsilon_{xy}) \tag{6.4}$$

where $\beta = 3.14$, and a is the C-C bond length. Note that $\boldsymbol{k}$ above is measured with

[3]The geometrical deformation of the mBZ will not be shown explicitly in the figures.

respect to the global momentum origin, and $\boldsymbol{K}_\tau = \tau \boldsymbol{K}_D$ is the original Dirac momentum in valley τ. $\boldsymbol{A}_l$ acts as an effective layer-dependent vector potential in a similar fashion to the orbital effect of an in-plane magnetic field [227] (except for the contrasting valley dependence).

Strain preserves $\hat{C}_{2z}$ but breaks $\hat{C}_{3z}$ and $\hat{C}_{2x}$. Hence the Dirac points which are protected by $\hat{C}_{2z}\hat{\mathcal{T}}$ remain intact, but are unpinned from the K_{M} and K'_{M} points and migrate towards the mBZ center. The Dirac points also separate in energy leading to compensated Fermi pockets at CN, and the overall bandwidth of the central bands increases dramatically (Fig. 6.1).

6.1.2.2 Non-local tunneling

The standard BM Hamiltonian obeys PHS very well—the only violations come from small twists in the Dirac cone kinetic terms which are suppressed in θ [45, 228]. However, many experiments show pronounced electron-hole asymmetry [5, 20, 22, 26–28, 35], with stronger superconductors on the hole side and more robust insulators on the electron side. We model this PHS-breaking by augmenting the BM model with a non-local interlayer tunneling (NLT) term [71, 186, 229, 230], which for valley K is

$$\begin{aligned}
\langle \boldsymbol{k}, 1 | \, H_{\mathrm{NLT}} \, | \boldsymbol{k}', 2 \rangle &= \tilde{T}_1(\boldsymbol{k}, \boldsymbol{k}')\delta_{\boldsymbol{k}-\boldsymbol{k}',\boldsymbol{0}} + \tilde{T}_2(\boldsymbol{k}, \boldsymbol{k}')\delta_{\boldsymbol{k}-\boldsymbol{k}',\boldsymbol{G}_1+\boldsymbol{G}_2} + \tilde{T}_3(\boldsymbol{k}, \boldsymbol{k}')\delta_{\boldsymbol{k}-\boldsymbol{k}',\boldsymbol{G}_2} \\
\tilde{T}_1(\boldsymbol{k}, \boldsymbol{k}') &= -\frac{1}{2}\left[\begin{pmatrix} \lambda_1 & \lambda_2 \\ \lambda_3 & \lambda_1 \end{pmatrix} (p_x - ip_y) + \begin{pmatrix} \lambda_1 & \lambda_3 \\ \lambda_2 & \lambda_1 \end{pmatrix} (p_x + ip_y) \right] \\
\tilde{T}_2(\boldsymbol{k}, \boldsymbol{k}') &= -\frac{1}{2}\left[\begin{pmatrix} \lambda_1 e^{i\phi} & \lambda_2 e^{-i\phi} \\ \lambda_3 & \lambda_1 e^{i\phi} \end{pmatrix} (p_x - ip_y) + \begin{pmatrix} \lambda_1 e^{-i\phi} & \lambda_3 \\ \lambda_2 e^{i\phi} & \lambda_1 e^{-i\phi} \end{pmatrix} (p_x + ip_y) \right] \\
\tilde{T}_3(\boldsymbol{k}, \boldsymbol{k}') &= -\frac{1}{2}\left[\begin{pmatrix} \lambda_1 e^{-i\phi} & \lambda_2 e^{i\phi} \\ \lambda_3 & \lambda_1 e^{-i\phi} \end{pmatrix} (p_x - ip_y) + \begin{pmatrix} \lambda_1 e^{i\phi} & \lambda_3 \\ \lambda_2 e^{-i\phi} & \lambda_1 e^{i\phi} \end{pmatrix} (p_x + ip_y) \right],
\end{aligned} \tag{6.5}$$

with $\lambda_2 = 2\lambda_1 = 0.18\,\mathrm{eV\AA}$, $\lambda_3 = 0$. The above form can be shown to hold even in the presence of heterostrain. This correction respects all the symmetries of the original BM Hamiltonian, and can be thought of as the next order in the Taylor expansion of the interlayer hopping. Note that $\boldsymbol{p}$ defined above is simply the sum of the two momenta of $|\boldsymbol{k}, 1\rangle$, $|\boldsymbol{k}', 2\rangle$, but each measured with respect to the respective $\boldsymbol{K}_+^l = M_l^{-1}\boldsymbol{K}_+$ of the

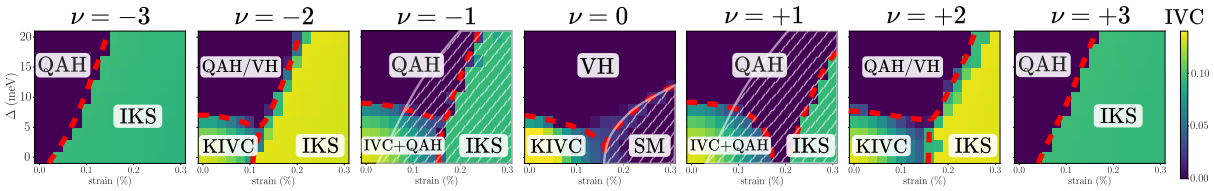

Figure 6.2: Summary of phases found in self-consistent HF at all integer fillings ν for different heterostrains and substrate potentials Δ, with NLT included. Color plot diagnoses IVC order (dark blue indicates unbroken $U(1)_V$ symmetry). Dashed red lines indicate approximate phase boundaries, and hatched areas denote absence of a charge gap. Properties of each phase are tabulated in Table 6.1. [IKS: incommensurate Kekulé spiral, QAH: quantized anomalous Hall state, KIVC: Kramers intervalley coherent state, VH: valley Hall state, IVC: intervalley coherence, SM: semi-metal]

layers. Consistent with density functional theory calculations, the effect of this term is to make the conduction bands more dispersive than the valence bands (Fig. 6.1).

6.1.3 Phase diagram

The phases obtained from our HF study are summarized in Fig. 6.2 and Table 6.1. The phase diagrams are obtained in the presence of NLT as a function of both strain (horizontal axis) and substrate potential (vertical axis). The colour scale diagnoses the magnitude of $U(1)_V$-breaking, which is sufficient to distinguish the different phases.

We now briefly describe the topology of the phase diagrams, beginning at even integer fillings. At $\nu = 0$, we recover previous results from the literature. The $\mathcal{T}'$-symmetric spin singlet KIVC [78, 83] is the ground state at zero strain and substrate. It consists of a filled intervalley coherent band in each Chern sector (duplicated in each spin sector), and can be succinctly described by ordering of $\tau_{x,y}\sigma_y$. The absence of coherence between opposite Chern sectors sidesteps the energy penalty induced by vortices in the order parameter that would be topologically required for other IVC candidates. It gives way to a symmetric semimetal (SM) at finite strains well within experimental bounds [97] (gaplessness is indicated with white hatching). For a strong enough sublattice potential, the system becomes a valley Hall (VH) insulator due to the splitting of the valence and conduction bands.

At $\nu = \pm 2$ in the absence of symmetry-breaking perturbations, the lowest energy state

Phase	$\lvert\nu\rvert$	spin pol.	valley pol.	$U(1)_V$	$\hat{\mathcal{T}} = \tau_x\hat{\mathcal{K}}$	$\hat{\mathcal{T}}' = \tau_y\hat{\mathcal{K}}$	$\hat{T}_{\boldsymbol{a}_i}$	$\hat{T}_{\boldsymbol{a}_i}e^{i\boldsymbol{q}\cdot\boldsymbol{a}_i\tau_z/2}$	$\lvert C\rvert$
IKS	1	*	0	✗	✓	✗	✗	✓	0
	2	0	0	✗	✓	✗	✗	✓	0
	3	*	0	✗	✓	✗	✗	✓	0
QAH	1	1	1	✓	✗	✗	✓		1
	2	0	2	✓	✗	✗	✓		2
	3	1	1	✓	✗	✗	✓		1
KIVC	0	0	0	✗	✗	✓	✓		0
	2	*	0	✗	✗	✓	✓		0
VH	0	0	0	✓	✓	✓	✓		0
	2	*	0	✓	✓	✓	✓		0
IVC+QAH	1	1	1	✗	✗	✗	✓		1
SM	0	0	0	✓	✓	✓	✓		0

Table 6.1: Symmetries and order parameters of HF phases at integer fillings ν that appear in Fig. 6.2. Spin (valley) polarization indicates the number imbalance of $\uparrow$ vs $\downarrow$ (K vs K') electrons per moiré unit cell. The spin quantization axis is arbitrary due to $SU(2)_S$-symmetry, and an asterisk indicates a degenerate manifold obtained by performing a valley-dependent spin-rotation. τ_μ are Pauli matrices in valley space, and $\hat{\mathcal{K}}$ is complex conjugation. IKS phases break a subset of moiré translations $\hat{T}_{\boldsymbol{a}_i}$, but preserve the combined valley-rotation + translation symmetry $\hat{T}_{\boldsymbol{a}_i}e^{i\boldsymbol{q}\cdot\boldsymbol{a}_i\tau_z/2}$, where $\boldsymbol{q}$ is the IKS wavevector.

is the spin-polarized version of the KIVC[4]. At a finite substrate potential strength, the optimal state becomes a sublattice-polarized $U(1)_V$-symmetric generalized ferromagnet, which can either be the QAH $\sim \sigma_z\tau_z$ or the VH $\sim \sigma_z$. These are exactly degenerate at HF level since the VH state is obtained by applying $\hat{\mathcal{T}}$ on one spin component of the QAH.

Along the strain axis, we find a first-order transition to a novel phase, which we dub the incommensurate Kekulé spiral, at an experimentally relevant strain ratio of $\epsilon \sim 0.1 - 0.2\%$. The main characteristic of the IKS is the breaking of moiré translation symmetry at a single wavevector $\boldsymbol{q}$, as explained in detail in Sec. 6.2. Since the spins within each valley are unpolarized, inclusion of intervalley Hund's coupling does not lead to qualitative changes.

The IKS order persists for fairly large substrate potential strengths. This means that the ordering is flexible enough to polarize onto one sublattice, as evidenced from the

[4]Actually, each valley has perfect spin polarization which is free to rotate under the $SU(2)_K \times SU(2)_{K'}$ symmetry. Depending on its sign, intervalley Hund's coupling will resolve this into either a spin ferromagnet or spin-valley locked antiferromagnet.

fairly constant magnitude of IVC throughout the phase. On the other hand, the KIVC is progressively weakened under increasing sublattice potential, and gives way to $U(1)_V$-preserving ferromagnets since its mechanism relies on inter-sublattice coherence[5] [79]. The strong PHS-breaking effect of NLT manifests in the shifted phase boundaries between $\nu = -2$ and $+2$. Furthermore, the zero-substrate band gaps (of order 10 meV) of both the KIVC and IKS phases are larger on the electron side than the hole side by $10 - 30\%$, which is consistent with the experimental trend of more robust insulators at positive fillings.

For $\nu = \pm 3$, a significantly smaller strain ($\epsilon \sim 0.02 - 0.05\%$) is able to destabilize the QAH. Typically we find a direct transition from the QAH to the IKS under increasing strain. The IKS at $\nu = \pm 3$ has the same symmetry properties as the one at $\nu = \pm 2$ (including TRS since we consider the spinless version), except that it can carry a spin polarization at $U(2)_K \times U(2)_{K'}$ level (of maximum $1\mu_B$ per moiré cell). For (anti-)ferromagnetic Hund's coupling, the spin moments carried by the two valleys will (anti-)align. Given the tiny strains required for the IKS to beat the QAH at $\nu = \pm 3$, a natural question that arises is whether the IKS can in principle be the ground state at zero strain. We emphasize that there is no fundamental reason that prohibits this scenario from occurring; for strong enough perturbations about the $U(4) \times U(4)$ limit, the strong-coupling insulators can be superseded by states outside the QHFM paradigm. While our HF calculations suggest this is not the case for our choice of parameters, the fact that the IKS can be obtained self-consistently without strain is a strong indication that the IKS remains a highly competitive state.

At $\nu = \pm 1$, the weak substrate potential region of the QAH phase has non-zero IVC. The transition from the QAH and QAH+IVC to the IKS now occurs at a larger strain ($\epsilon \sim 0.15 - 0.2\%$). The effect of intervalley-Hund's terms is similar to that at $\nu = \pm 3$, i.e. a net spin polarization of (0) 1 for (anti-)ferromagnetic coupling. In contrast to the other integer fillings, at $\nu = \pm 1$ the IKS state never develops a charge gap.

The phase diagrams are very similar in the average subtraction scheme, with only quantitative changes in the phase boundaries[6]. While the topologies of the CN scheme

[5] Recall the intertwining of sublattice and valley in each Chern sector $C = \tau_z \sigma_z$.

[6] In addition, the gaps of the QAH state at $|\nu| = 3$ are significantly smaller than those of the graphene scheme used for the figures in this chapter.

phase diagrams are unchanged, the strain scales involved are unphysically smaller by roughly two orders of magnitude, even in the presence of sublattice coupling. Given the heightened fragility of the $\nu = +3$ QAH against tiny amounts of strain, we believe that this scheme is not an appropriate choice (at least for finite strains).

6.2 Spin-unpolarized Kekulé spirals at $\nu = \pm 2$

The emergence of the IKS at all non-zero integer fillings, and its relative stability against sublattice alignment, points to its ubiquity in the presence of moderate levels of strain. In this section, we dissect the properties and anatomy of IKS order, and show how they contribute to its robustness. We focus on $\nu = \pm 2$, though most of the statements made below apply equally well to the IKS at $\nu = \pm 3$ (and even metallic IKS states at $\nu = \pm 1$ and non-integer fillings).

6.2.1 Symmetries and generalized Bloch theorem

We begin by discussing its non-translational symmetries. The IKS preserves a spinless version of TRS $\hat{\mathcal{T}} = \tau_x \mathcal{K}$[7]. The colouring on the phase diagrams indicates that it possesses non-zero IVC and breaks $U(1)_V$. As $\hat{C}_{2x}$ does not commute with valley rotations, it is generally broken. However there always exists a combination of $\hat{C}_{2x}$ and valley rotation, $\hat{C}'_{2x}$, which depends on the intervalley phase and remains a good symmetry. As we will see, this is linked to the fact that $U(1)_V$ rotation manifests as a translation of the IKS order.

An important feature of the IKS that sets it apart from the strong coupling insulators is its breaking of moiré translation symmetry $\hat{T}_{\boldsymbol{a}_i}$. However, distinct from other candidate TSB orders such as stripes [35, 187, 204, 231], it continues to satisfy a modified translation symmetry $\hat{T}'_{\boldsymbol{a}_i} = \hat{T}_{\boldsymbol{a}_i} e^{i\boldsymbol{q}\cdot\boldsymbol{a}_i \tau_z/2}$, which is simply the usual translation augmented with a valley rotation. The generally non-zero wavevector $\boldsymbol{q}$, which lives in the mBZ, depends on the particular IKS realization under consideration. At the level of HF projectors, this

[7] This continues to be true even at non-integer fillings [59].

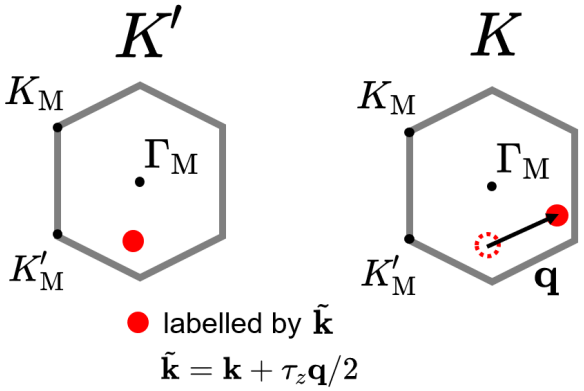

Figure 6.3: In the IKS, the graphene valleys hybridize at a finite wavevector $\boldsymbol{q}$. This is in contrast to $\boldsymbol{q} = 0$ strong coupling ferromagnets with IVC, such as the KIVC, which would hybridize the red dot in valley K' with the dotted circle in K.

is realized as the following structure of intervalley density matrix elements

$$\langle \hat{c}^\dagger_{\boldsymbol{k}+\boldsymbol{p},\tau=+} \hat{c}_{\boldsymbol{k},\tau'=-} \rangle \sim f(\boldsymbol{k}) \delta_{\boldsymbol{p},\boldsymbol{q}}, \tag{6.6}$$

where the band/sublattice and spin indices are left implicit. In short, the valleys hybridize at a finite wavevector $\boldsymbol{q}$, as sketched in Fig. 6.3. Crucially the IVC occurs at a single $\boldsymbol{q}$, leading to a circular IVC spiral of definite handedness, as there is no symmetry relating the spiral to the analogous spiral at $-\boldsymbol{q}$.

In fact for the parameters studied, we find a whole family of spirals which differ only in $\boldsymbol{q}$ and are close in energy, as shown in Fig. 6.4. The ideal wavevector $\boldsymbol{q}_0$ is slightly greater than 1/3 of the mBZ, and evolves weakly with strain magnitude. The ideal spiral ordering appears to occur at an incommensurate $\boldsymbol{q}_0$ since there aren't any noticeable energetic features at commensurate wavevectors. The energy density of the IKS can be fitted to the form $\frac{\rho_s}{2}(\boldsymbol{q} - \boldsymbol{q}_0)^2$, from which we estimate the wavevector stiffness to be $\rho_s \sim 0.4\,\text{meV}$, without strong spatial anisotropy. Fig. 6.4 shows that as the strain angle φ rotates, $\boldsymbol{q}_0$ also changes, but appears to have roughly constant magnitude and predominantly lies near a moiré crystallographic axis. NLT does not affect the qualitative features of these plots.

$\hat{T}'$-symmetry implies a generalized Bloch theorem, which stipulates that the single-

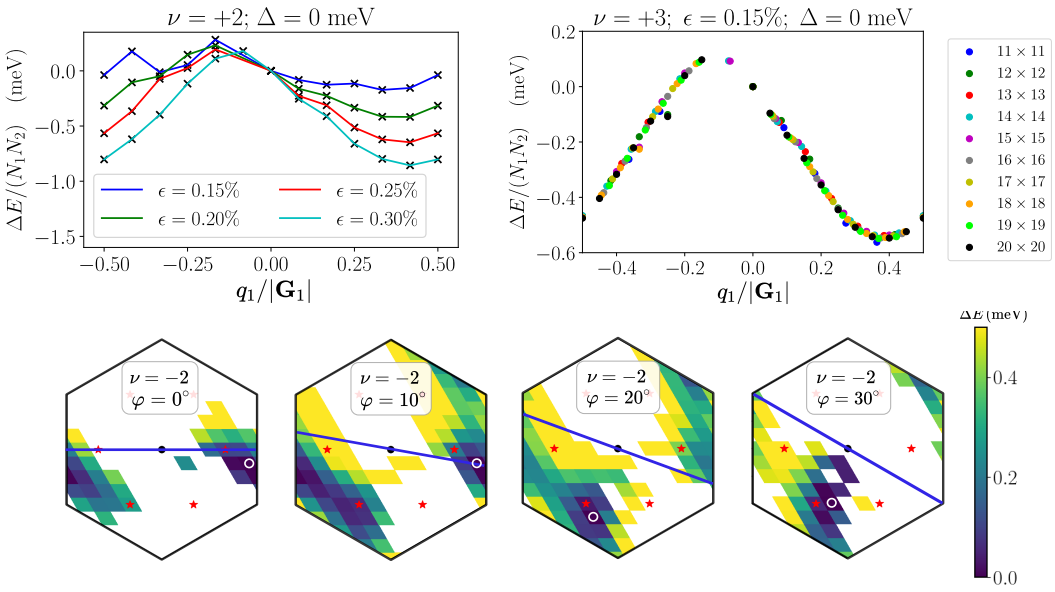

Figure 6.4: Top: IKS energy relative to the lowest translation-symmetric state for different strains, fillings, system sizes, and spiral wavectors $\boldsymbol{q}$ along $\boldsymbol{b}_1$. Bottom: Relative energies of IKS states for different strain angles φ (blue axis) and enforced IKS wavevectors $\boldsymbol{q}$. Red stars denote $\boldsymbol{q}$'s corresponding to period-tripling along the moiré axes, and white circles denote minimum energy wavevectors $\boldsymbol{q}_0$. Non-IKS states that converged to higher energies were discarded. Strain is 0.2%.

particle wavefunctions satisfy

$$\psi_{\tilde{\boldsymbol{k}}}(\boldsymbol{r} + \boldsymbol{a}_i) = e^{i\tilde{\boldsymbol{k}}\cdot\boldsymbol{a}_i} e^{-i\boldsymbol{q}\cdot\boldsymbol{a}_i\,\tau_z/2} \psi_{\tilde{\boldsymbol{k}}}(\boldsymbol{r}). \tag{6.7}$$

Here, $\tilde{\boldsymbol{k}}$ is a new momentum label restricted to the first mBZ, which differs from the conventional crystal momentum. In particular, $\tilde{\boldsymbol{k}}$ labels real, physical momenta $\tilde{\boldsymbol{k}} + \tau_z \boldsymbol{q}/2$ in the two valleys $\tau_z = \pm$. From (6.7), it follows that we can write the single-particle wavefunctions as

$$\psi_{\tilde{\boldsymbol{k}}}(\boldsymbol{r}) = e^{i\boldsymbol{r}\cdot(\tilde{\boldsymbol{k}} - \tau_z \boldsymbol{q}/2)} u_{\tilde{\boldsymbol{k}}}(\boldsymbol{r})\,, \tag{6.8}$$

where $u_{\tilde{\boldsymbol{k}}}(\boldsymbol{r})$ is the periodic part satisfying $u_{\tilde{\boldsymbol{k}}}(\boldsymbol{r} + \boldsymbol{a}_i) = u_{\tilde{\boldsymbol{k}}}(\boldsymbol{r})$[8]. As a result, we can define a HF band structure in the mBZ for general IKS, even if the order wavevector $\boldsymbol{q}$ is incommensurate with the moiré lattice. We note that a similar observation has previously

[8]A corollary is that if we are interested in obtaining IKS states of a particular $\boldsymbol{q}$, we can reduce the numerical cost by performing translation invariant HF, except that the valleys are boosted in momentum space by a relative shift $\boldsymbol{q}$ (as done in Fig. 6.4). Of course to obtain the lowest energy IKS, we would have to minimize over all values of $\boldsymbol{q}$. Note that even without enforcing a particular $\boldsymbol{q}$, HF still only converges to a single-$\boldsymbol{q}$ state.

been made for incommensurate circular spin spiral states [232, 233].

Another, but closely related, consequence of the $\hat{T}'_{\boldsymbol{a}_i}$ symmetry is that the IKS can only have a non-zero energy gap (ignoring the Goldstone modes[9]) at integer fillings, unless it breaks additional symmetries or develops non-trivial topological order. To understand this, we first add the following small perturbation to the Hamiltonian at $\nu = \pm 2$

$$\hat{V} = h \int \mathrm{d}^2\boldsymbol{r} \left[\cos(\boldsymbol{q}\cdot\boldsymbol{r} + \alpha)\hat{\psi}^\dagger(\boldsymbol{r})\tau_x\sigma_x\hat{\psi}(\boldsymbol{r}) + \sin(\boldsymbol{q}\cdot\boldsymbol{r} + \alpha)\hat{\psi}^\dagger(\boldsymbol{r})\tau_y\sigma_x\hat{\psi}(\boldsymbol{r}) \right]. \tag{6.9}$$

This preserves $\hat{T}'_{\boldsymbol{a}_i}$ but explicitly breaks $U(1)_V$, thereby inducing a gap $\propto |h|$ in the Goldstone modes. Then, we invoke a generalized Lieb-Schulz-Mattis theorem which states that the IKS with gapped Goldstone modes can have a unique ground state on the cylinder geometry which is separated by a non-zero energy gap from all other states in the spectrum only if the charge per unit cell is an integer. To show that such a theorem indeed holds, we can employ the standard adiabatic flux-insertion arguments by Oshikawa. [234, 235]. The extra factor $e^{i\boldsymbol{q}\cdot\boldsymbol{a}_i\tau_z/2}$ in the translation operator does not affect this argument, as it commutes with the charge $U(1)$ symmetry. This explains why, despite involving a *modulation* that is incommensurate with the moiré lattice, the IKS insulator is tied to *densities* that are commensurate with it.

Microscopically, the $\hat{\mathcal{T}}$-invariant IVC order of the IKS induces a Kekulé-like pattern on the graphene scale, with orientation determined by the local IVC angle θ_{IVC}[10] (see Fig. 6.5). Since the symmetry-breaking occurs predominantly within the central bands[11], the Kekulé or $\sqrt{3}\times\sqrt{3}$ pattern, which triples the graphene unit cell, is strongest in the AA regions where the flat band wave functions are spatially localized. However, the finite-$\boldsymbol{q}$ character of the IKS state means that the microscopic Kekulé-like patterns differ between different AA regions, as dictated by the combined moiré lattice translation and valley-$U(1)$ rotation symmetry $\hat{T}'_{\boldsymbol{a}_i}$. Regions lying along a strip perpendicular to $\boldsymbol{q}$ will have the same local Kekulé distortion, while the Kekulé phase along $\boldsymbol{q}$ will rotate with

[9] At $|\nu| = 2$, the spin singlet IKS has four linear Goldstone modes from the broken generators $\{\tau_z, \tau_z s_i\}$. At $|\nu| = 3$, the ferromagnetic IKS (spin-polarized along $\hat{s}_z$) has one linear type-A mode from $\{\tau_z\}$ and two quadratic type-B modes from $\{s_x, s_y\}$ and $\{\tau_z s_x, \tau_z s_y\}$ [114, 115].

[10] Explicit real-space images of the microscopic bond/site ordering have been computed in Ref [197].

[11] This can be surmised by increasing the number of active bands from 8 to 24, and checking that the new active remote bands do not possess substantial IVC.

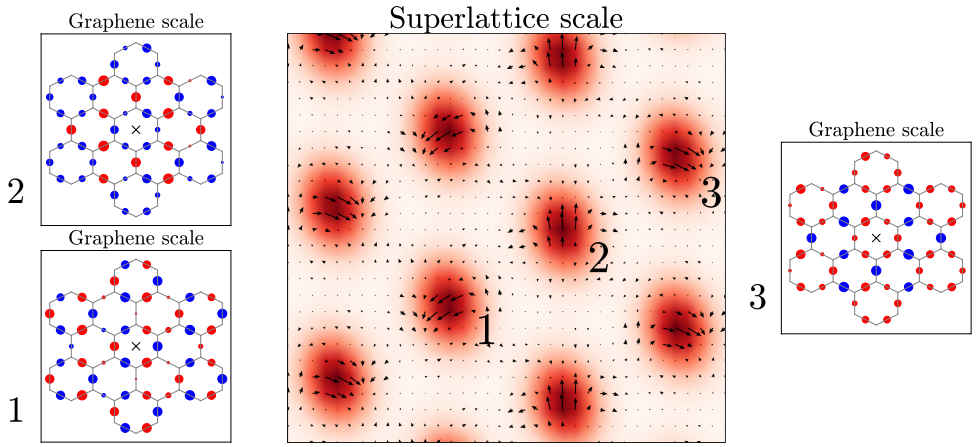

Figure 6.5: Real-space picture of an IKS with $\boldsymbol{q} = \boldsymbol{b}_1/3$. The colorplot on the superlattice scale shows the charge density, with darks spots corresponding to AA regions. Black arrows represent the complex IVC order parameter $\sim \langle \tau_x \sigma_x \rangle + i \langle \tau_y \sigma_x \rangle$. For each of the three inequivalent AA regions, the expectation value of $c_{\mathrm{A}}^\dagger c_{\mathrm{B}} + c_{\mathrm{B}}^\dagger c_{\mathrm{A}}$ on the microscopic graphene bonds is shown. Blue (red) dots correspond to positive (negative) expectation values, and the center of the AA region is marked with a black cross. The different inequivalent AA regions have different approximate $\sqrt{3} \times \sqrt{3}$ Kekulé-like patterns on the graphene scale.

spatial period $2\pi/|\boldsymbol{q}|$. Since the TSB is purely IVC, with no $-\boldsymbol{q}$ or higher harmonic components, there is no additional charge reconstruction at the moiré scale.

Before concluding the discussion of TSB, we point out the following subtlety. In the absence of $\hat{C}_{3z}$ symmetry (which is broken by strain), Γ_{M} in the single-valley BM model is no longer a high symmetry point. From this one might conclude that the choice of Γ_{M} in one of the two valleys becomes arbitrary (Γ_{M} in the other valley is still fixed by either $\hat{C}_{2z}$ or $\hat{\mathcal{T}}$). Making a different choice for Γ_{M} does not go without consequences for the IKS, as this changes the wavevector $\boldsymbol{q}$ at which the intervalley coherence occurs. For commensurate twist angles, however, there is a preferred Γ_{M}-point in the mBZ even in the absence of $\hat{C}_{3z}$—namely, it is the point that should fold on top of the Γ-point of the monolayer graphene BZ (which is fixed by $\hat{C}_{2z}$ or $\hat{\mathcal{T}}$). From this it is clear that the wavevector $\boldsymbol{q}$ is well-defined for commensurate twist angles, and that the corresponding superlattice translation symmetry is unambiguously broken. In our numerical simulations at incommensurate twist angles, we have always used the same choice for Γ_{M} as in the commensurate twist angle case, such that the location of Γ_{M} varies continuously as a function of θ. However, for incommensurate twist angles a

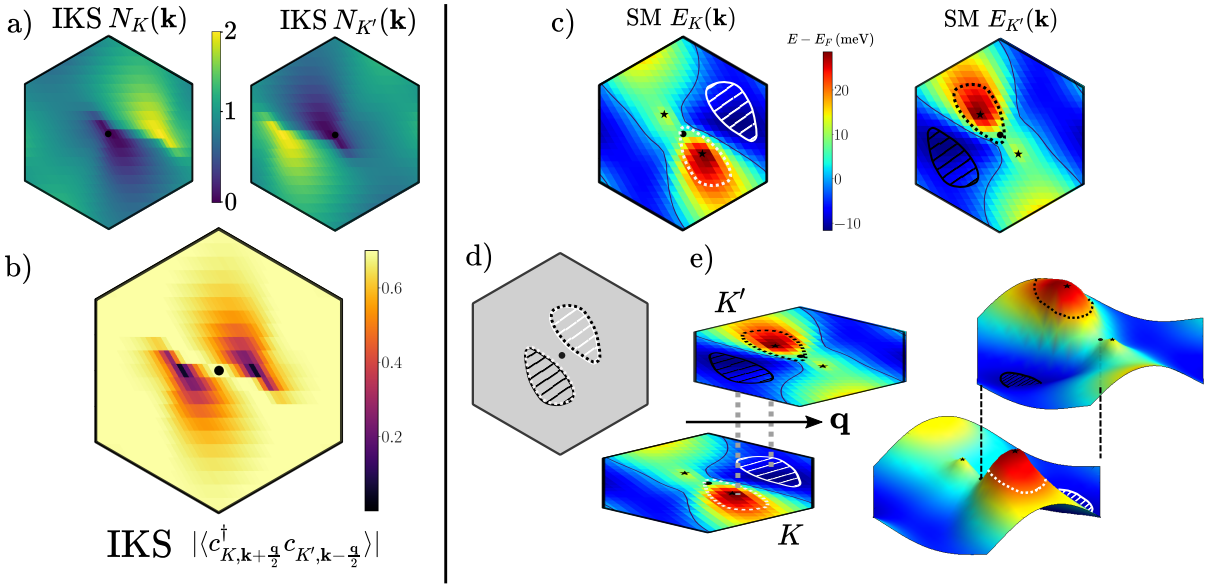

Figure 6.6: mBZ-resolved properties of the IKS at $\nu = -2$. a) Valley populations of the IKS. b) Frobenius norm of the IVC at wavevector $\boldsymbol{q} = \boldsymbol{G}_1/3$. System size is 48×16, strain is 0.2%, substrate is $\Delta = 0\,\text{meV}$, and NLT is not included. c) Dispersions of the lower band for the metastable symmetry-preserving self-consistent SM. Hatched (dotted) lobes, situated near low (high) energy regions, will be predominantly filled (empty) in the IKS. Black lines indicate the Fermi surface, and black stars mark Dirac point locations. d,e) Schematic construction of the IKS—a relative momentum boost of the valleys by $\boldsymbol{q}$ allows the lobes to overlap each other. Regions not within the lobes participate strongly in IVC.

different choice for Γ_M is possible in principle, and thus the wavevector $\boldsymbol{q}$ of the IKS state becomes 'gauge dependent'. This is consistent with the fact that for incommensurate twist angles, there is strictly speaking no superlattice translation symmetry.

6.2.2 Structure and energetics of the IKS

Insight into the properties of the IKS can be gained by analyzing its momentum-resolved single-particle density matrix in more detail. Fig. 6.6b plots the strength of IVC at $\nu = -2$ in momentum space, showing that it is close to the maximum value of $1/\sqrt{2}$ throughout most of the mBZ. The exceptions are at two lobes in the mBZ, where the electron populations $N_\tau(\boldsymbol{k})$ in the two valleys (Fig. 6.6a) are close to 0 or 2. The total occupation at each $\boldsymbol{k}$ is 2 consistent with an insulating state. The strong momentum-dependence of the IKS state sets it apart from previously studied strong coupling phases [79, 83]. From our numerics we find that the same coherence structure is repeated for

both spin species. Therefore, we henceforth consider spin to simply be a spectator degree of freedom, an assumption which is further validated by the 'basis spiral' analysis in Sec. 6.3.

The locations of IVC-depletion provide strong clues as to the mechanism underlying IKS formation. In Fig. 6.6c, we calculate for each valley the HF spectrum of the lower band of the self-consistent symmetry-preserving SM. This captures the major momentum-dependent effects that strain and interactions have on the band structure. The dispersions of the two valleys are related by TRS. All Dirac points lie above E_F at $\nu = -2$. Near Γ_{M}, there is a region of very high energy (red) that coincides with one of the Dirac points. There is also a region of low energy (dark blue) lying in some other region of the mBZ. Because of TRS, the low/high energy lobes (indicated by hatched/dotted regions) in the two valleys are related by $\boldsymbol{k} \to -\boldsymbol{k}$.

We now sketch an intuitive picture for how these dispersion features influence the parameters of the IKS order. Fig. 6.6d,e demonstrates that coupling the two valleys at a finite $\boldsymbol{q}$ can pairwise align a high energy lobe with a corresponding low energy lobe in the other valley. In these momentum regions, the system will choose to polarize into the energetically favorable valley. Elsewhere, substantial valley hybridization is induced, such that the valley order rotates smoothly in momentum space and maintains good exchange energy. In this way, the IKS is able to maximize IVC while respecting the prominent characteristics of the band dispersion. Each $\tilde{\boldsymbol{k}}$ is equally populated, allowing for an insulating state. Note that attempting to induce IVC at $\boldsymbol{q} = 0$ instead runs into issues—a large portion ($\sim 4\times$lobe area) of the mBZ would be unable to participate in the IVC since the lobes have small overlap. Furthermore, the total electron occupations would vary as a function of $\tilde{\boldsymbol{k}}$, meaning the state cannot be insulating.

This perspective naturally explains the strong $\boldsymbol{k}$-dependence of IVC and the slow variation of the IKS energy with $\boldsymbol{q}$. The somewhat diffuse features of renormalized dispersion mean that for nearby $\boldsymbol{q}$, the locations/shapes of the lobes only change slightly, leading to a small and roughly isotropic wavevector stiffness. A simple estimate for the ideal wavevector $\boldsymbol{q}_0$ can be made by connecting the minimum energy momentum in valley K' with the maximum energy peak in valley K. The predicted $\boldsymbol{q}_0$ is broadly consistent with HF results of the IKS for a range of strain angles φ.

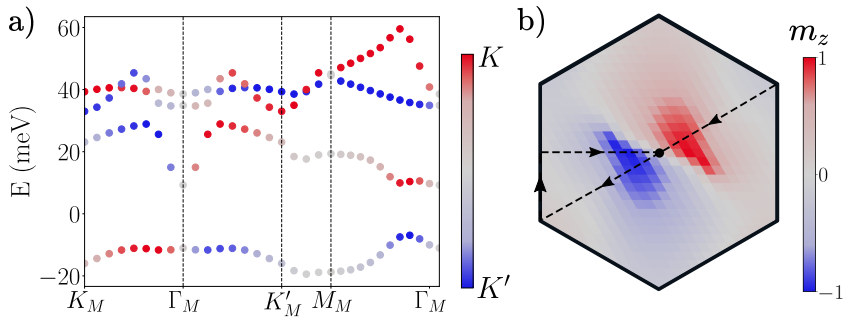

Figure 6.7: a) Band structure of the IKS at $\nu = -2$, with color indicating the valley polarization of the HF orbitals. b) z-component of the vector $\boldsymbol{m}(\tilde{\boldsymbol{k}})$ in the parameterization of (6.10). Dashed lines indicate mBZ path in a). In both plots, $\tilde{\boldsymbol{k}}$ refers to the valley-dependent boosted momentum $\boldsymbol{k} + \tau_z \boldsymbol{q}/2$.

We emphasize that this scenario opens a gap at E_F but, unlike most of the translation-invariant insulators, does not rely on gapping out the Dirac points, which remain high in energy above E_F. Instead the $\boldsymbol{k}$-dependent IVC hybridizes the two valleys at finite $\boldsymbol{q}$ and pulls the occupied band below the rest of the states (Fig. 6.7a).

We can construct a simple *ansatz* for the IKS projector in the absence of substrate alignment, which matches the HF numerics extremely well. We partially fix the Chern basis gauge by requiring that $\hat{C}_{2z}$ acts as $\tau_x\sigma_x$ and $\hat{\mathcal{T}}$ as $\tau_x\hat{\mathcal{K}}$—the remaining gauge freedom acts as $e^{i\varphi_{\boldsymbol{k}}\tau_z\sigma_z}$. The spin-singlet IKS state at $\nu = -2$ can then be parameterized by the projector

$$P_{\nu=-2}(\tilde{\boldsymbol{k}}) = \frac{1}{4}(\mathbb{1} + \boldsymbol{n}_{\tilde{\boldsymbol{k}}} \cdot \boldsymbol{\gamma})(\mathbb{1} + \boldsymbol{m}_{\tilde{\boldsymbol{k}}} \cdot \boldsymbol{\eta})\,, \tag{6.10}$$

where the $\boldsymbol{\gamma}$ and $\boldsymbol{\eta}$ matrices are defined in (2.28), the gauge-variant $\boldsymbol{n}_{\tilde{\boldsymbol{k}}}$ is entirely in the $x-y$ plane, and an identity matrix in spin space is implicit. Across most of the mBZ, the vector $\boldsymbol{m}_{\tilde{\boldsymbol{k}}}$ lies in-plane with a constant angle that can be changed by a global $U(1)_V$-rotation. At the lobes, $\boldsymbol{m}_{\tilde{\boldsymbol{k}}}$ orients towards the poles, reflecting the valley polarization in these momentum regions (recall that $\eta_z = \tau_z$) (Fig. 6.7b). Since γ_x, γ_y in (6.10) anticommute with the Chern number γ_z, there is both inter-Chern and intra-Chern IVC in the IKS with equal magnitude. This implies that the IVC significantly entangles bands with opposite Chern number, in contrast to the $U(4) \times U(4)$ strong coupling ferromagnets. Importantly, this distinguishes the type of IVC order found here from the uniform $\mathcal{T}$IVC state of Ref. [78] (which also preserves TRS at even integer fillings). In terms of symmetries, the only differences between the $\mathcal{T}$IVC and IKS states are that

the former is translationally invariant and cannot be made spin singlet by opposite spin rotations in the two valleys. Both states can be made $\hat{C}_{2z}\hat{\mathcal{T}}$-symmetric by a suitable global valley-$U(1)$ rotation. The IKS projector at $\nu = +2$ can be approximately found by particle-hole conjugation.

The construction outlined above, involving the nesting of features of a parent symmetry-preserving band structure, is suggestive of a weak-coupling instability. However the $U(1)_V$-breaking coherence occurs nearly everywhere in the mBZ, instead of just the lobe boundaries. Furthermore, the Fermi surfaces of the SM or the non-interacting BM model generically bear little relation to the momentum structure in the IKS state. Indeed, both strain and interactions play a vital role in renormalizing the central bands and setting the stage for symmetry-breaking phases—the non-interacting BM bands have a total bandwidth $\sim 5\,\text{meV}$, which broaden to $\sim 15\,\text{meV}$ in the presence of strain (breaking $\hat{C}_{3z}$ and shifting the Dirac points up/down), and finally $\gtrsim 50\,\text{meV}$ with the inclusion of interactions. We find that strengthening the Coulomb interaction (by reducing ϵ_r) favours the strong coupling states. Strain thus effectively tunes the system from strong coupling, where Chern-diagonal ferromagnetic states dominate, to *intermediate* coupling where other phases (such as the IKS) emerge that violate the $U(4) \times U(4)$ hierarchy. In other words, strain substantially increases the dispersion, which undermines the perturbative stability of the strong coupling ferromagnets and allows the IKS to undercut them in energy. On the other hand, twist angle, which weakly influences the non-interacting central band dispersion, does not have a significant impact on the phase diagram.

This strong- to weak-coupling crossover can also be viewed through the lens of direct versus exchange energy [88]. The intra-Chern states at small strain are stabilized by exchange, in analogy with QHFM. At larger strains, including just the Hartree piece of the interaction already recreates the key features of the band renormalization. As evidenced in Fig. 6.2, the IKS is more competitive farther away from charge neutrality, in harmony with the larger Hartree peak (dip) expected for increasing hole (electron) doping [35]. All particles will feel this increased Hartree potential, while exchange effects are only applicable between electrons of the same flavor. We caution though that this direct-exchange dichotomy is not so clear-cut in practice—separation of the IKS energy into its components reveals that both Hartree and Fock contributions change significantly

with comparable magnitude as a function of $\boldsymbol{q}$. Also, exchange does significantly perturb the band structure of the self-consistent SM, and its inclusion is necessary to obtain reasonable predictions for $\boldsymbol{q}_0$. This implies that a proper treatment of both terms is required to adequately capture the physics of TBG for realistic parameters.

6.3 Kekulé spirals at odd integer filling

All numerically obtained IKS states preserve spinless TRS $\mathcal{T}$, implying that the Chern number C vanishes. This fact is remarkable for the odd fillings, since the strong coupling ferromagnets can only accommodate phases with odd C. However, recent experiments have shown the existence of even-C gapped phases extending down to zero magnetic field at odd fillings [35]. One possible route to achieving this is by folding the mBZ in half and forming period-2 charge order, as theoretically argued by some authors [35]. Each Chern band (a finite sublattice splitting was considered) splits into a $|C| = 1$ and 0 mini-band, and a variety of different C states can be obtained by selectively polarizing these. Our work proposes a fundamentally distinct scenario, relying instead on IVC to produce the requisite $C = 0$ bands, and on 'modified' moiré translation breaking to minimize the energy. The IKS is agnostic to the presence of substrate alignment, and is a natural robust insulating candidate for experiments where strain is often an external confounding factor. Characterizations of the moiré charge order or strain in the sample of Ref. [35] would help determine which theoretical scenario is operative there.

Since the IKS states have similar properties at all non-zero integer fillings, we expect them to be closely related. To make the connection explicit, we consider the $|\nu| = 3$ IKS as a 'basis spiral'. We start with the $\nu = -3$ IKS with total spin-polarization enforced for simplicity. In order to construct a $\nu = -2$ IKS, we take two copies of the $\nu = -3$ basis spiral in order to obtain a spin-unpolarized IKS. The same construction is possible at positive filling by particle-hole conjugation. The notion of the $|\nu| = 2$ IKS as two copies of the $|\nu| = 3$ IKS is consistent with the relative factor of $\sqrt{2}$ of the $U(1)_V$-breaking order parameter in Fig. 6.2.

For the $\nu = -1$ IKS, we note that TSB is entirely in one spin sector, whereas the other spin sector has the same symmetries as the VH state at $\nu = -2$. This motivates

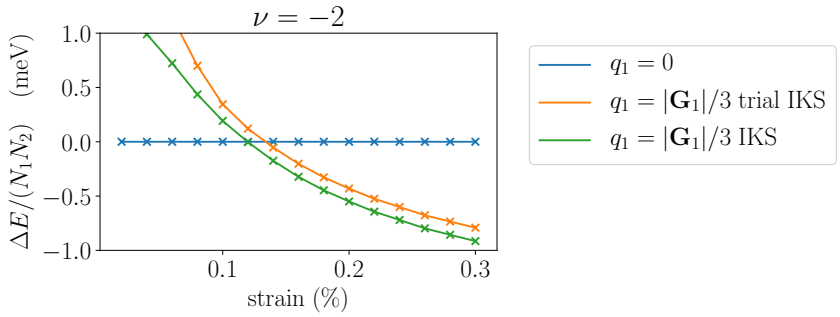

Figure 6.8: Comparison of the energies of the translationally invariant state, the ideal IKS and the IKS trial state at $\nu = -2$. The IKS trial state is obtained by combining two copies of the IKS HF solution at $\nu = -3$. System size is 12×12, $\Delta = 0\,\text{meV}$ and NLT is included.

the following construction: We start with the spin-polarized VH state at $\nu = -2$ and add to it the $\nu = -3$ IKS in the opposite spin sector. Consistent with this fact, the $U(1)_V$-breaking order parameter has the same magnitude in the IKS phases at $|\nu| = 1$ and 3.

We show in Fig. 6.8 that the trial states for the $\nu = -2$ IKS based on this construction have energies that are very close to the self-consistent HF solution at those fillings. We also find that HF simulations using these trial states as initial inputs converge very quickly to the self-consistent IKS ground state at that filling, demonstrating that the trial states have the correct correlations. For $\nu = -1$ the trial state energies are not as close to those of the self-consistent IKS due to the fact the IKS is not insulating at this filling.

6.4 Discussion

6.4.1 Quenched disorder and finite temperature

For the KIVC, which occurs at very small strain, quenched disorder is relatively innocuous. The reason is that this state breaks TRS, while physical impurities in graphene are time-reversal symmetric, which implies that they cannot couple as random-field disorder to the KIVC order. The IKS, on the other hand, preserves TRS and is consequently less protected against disorder. For example, because the IKS state has a Kekulé pattern on every AA region, graphene-scale bond disorder couples to the IVC order as a random field. A Schrieffer-Wolff analysis suggests that actually long-wavelength disorder is most

important. This is due to the large gap to the remote bands, and the fact that the flat band wave functions vary slowly on the moiré scale [58].

IKS order breaks the valley-charge conservation symmetry and superlattice translation. Ignoring the explicit symmetry-breaking effects of strain, it also breaks $\hat{C}_3$ via a non-zero $\boldsymbol{q}$. Because the IKS is invariant under a combination of superlattice translation and valley $U(1)$ rotation, only local operators with a non-zero valley charge can detect the TSB. A corollary of this observation is that the TSB order is replaced by quasi-long range order at non-zero temperature, and is completely lost once vortices of the IVC order proliferate at $T_{\mathrm{BKT}} \lesssim \pi\rho_s/2 \sim 7$ K. The rotational symmetry breaking, on the other hand, can be detected by operators which have zero valley charge. This means that the nematic order, can persist as true long-range order at non-zero temperatures. However, because TBG is a two-dimensional material, reintroducing quenched moiré disorder will, strictly speaking, destroy all ordered phases (breaking both discrete and continuous symmetries). For sufficiently weak disorder, the Imry-Ma domains of the discrete $\hat{C}_3$-breaking order is expected to be much larger than the relatively small TBG devices currently being used in experiment. In this case, nematicity will survive the presence of quenched disorder as vestigial order of the IVC spiral state.

6.4.2 Experiments

We have demonstrated that IKS order is ubiquitous at nonzero integer fillings in the presence of small amounts of heterostrain, largely independent of substrate or fine details of twist angle. This fact, combined with the absence of IKS order at charge neutrality in favour of a gapless SM, potentially provides a unified explanation of several recent experiments. This picture requires the assumption that small heterostrain is inveitably present in typical experimental samples; this is not unreasonable, particularly given the modest heterostrain needed to stabilize IKS order (which is comparable to experimentally observed strains [41–43]).

Before discussing the connection of our integer results to experiments, we note that the mean-field analysis above has been extended to non-integer dopings throughout the central band range in the presence of strain in Ref. [59]. IKS order persists for a finite

range of ν about the integers, and is interleaved with other types of flavour-polarized orders. Interestingly, the ideal wavevector $\boldsymbol{q}_0$ can change rapidly as the density is tuned. By computing the density-dependent chemical potential $\mu(\nu)$, we find that the characteristic sawtooth pattern in the experimentally measured inverse compressibility can be reproduced both in the zero and intermediate strain regime. This suggests that this 'cascade physics' cannot discriminate between the strong coupling [87], intermediate coupling, and 'Dirac revivals' [29] scenarios. The calculated Fermi surface degeneracies in the strained regime are also consistent with the experimental Landau fans[12].

The global properties of the phase diagrams (Fig. 6.2) in the strained regime are broadly in agreement with many transport experiments. At neutrality, moderated strained TBG is semimetallic, while at $\nu = \pm 1$, it is metallic but with a significantly lower carrier density than the non-interacting BM model due to strong IKS order. At $\nu = \pm 2, \pm 3$, it becomes an IKS insulator. While no single experiment matches all of these characteristics at once, the IKS and heterostrain present an alternative regime to the weak and strong coupling limits, so that theory is better equipped to interpret the myriad of experiments.

At even integer fillings, the IKS can be distinguished from the KIVC by probing the spin physics. In particular, in a small magnetic field the KIVC at $\nu = \pm 2$ has a local spin moment of $\lesssim 2\mu_B$ per moiŕe unit cell[13], whereas the IKS at $\nu = \pm 2$ has a vanishing local moment. It follows that in samples with negligible strain, which would have a strong KIVC gap at neutrality (assuming there is also negligible hBN alignment), the insulators at $\nu = \pm 2$ should have a non-zero local spin moment, whereas strained samples with semi-metallic behaviour at neutrality should have no (spin or orbital) magnetic moment at $\nu = \pm 2$. By applying a small strain to an initially unstrained sample, one should therefore observe a strong first order transition associated with an abrupt disappearance of the local moment as one enters the IKS phase. If the strain in experiment can both be slowly increased and decreased, hysteretic behaviour should be observed for the local spin moment around the KIVC–IKS transition. We note that Ref. [22] indeed found evidence

[12] Experiments typically see Landau fans emanating from $|\nu| = 0, 2, 3$ with slopes corresponding to $4, 2, 1$ degenerate Fermi surfaces respectively.

[13] Adding a ferromagnetic intervalley Hund's coupling to the Hamiltonian would induce a magnetic moment of $2\mu_B$ per unit cell for the KIVC at $\nu = \pm 2$, even in the absence of a magnetic field. If, as was argued in Refs. [236, 237], the intervalley Hund's coupling is anti-ferromagnetic as a result of e.g. phonon scattering [80], then a small magnetic field will cause the spins in the two valleys to cant, producing a magnetic moment per unit cell which is smaller than $2\mu_B$.

for spin-unpolarized insulators at $\nu = \pm 2$ in a sample which is semi-metallic at neutrality, which is consistent with the IKS/nematic SM scenario under the assumption that their samples are heterostrained at the $\sim 0.1 - 0.2\%$ level.

At $\nu = \pm 3$, the IKS also has a smaller local magnetic moment than the QAH which occurs in the absence of strain. As both states are spin polarized in a small field, this difference is now due to the large orbital moment of the QAH, which is absent in the IKS owing to $\mathcal{T}$-symmetry. However, the easiest way to distinguish the IKS from the QAH is via the transverse or Hall resistance R_{xy}. This quantity is zero in the IKS as dictated by the spinless TRS, but takes on a quantized non-zero value in the QAH. In Refs. [22, 48], insulating states were observed at $\nu = +3$ which show Landau fans in magnetotransport measurements that are consistent with a zero Chern number. Given the semi-metallic behaviour at charge neutrality, we thus expect such samples to be strained and therefore the insulators at $\nu = +3$ to have IKS order.

Given that the nematic order of the IKS survives at finite temperature, we anticipate that the IKS insulators at $\nu = \pm 2, \pm 3$ should show strong interaction-induced nematicity, much stronger than what one would naively expect from the small strain present in the sample. This prediction is in harmony with the experimental observations of Ref. [20, 21], where nematicity was observed in the superconducting dome between $\nu = -3$ and $\nu = -2$. Indeed, unless the insulators at integer fillings are separated from the superconducting dome by a strong first order transition, one would generally expect the insulators and the superconductors to either both be isotropic or both be nematic. Ref. [59] shows that IKS order persists for a finite range of doping around the integers and survives to temperatures[14] much greater than the experimental T_c, suggesting that the superconducting dome could indeed inherit physics from the IKS. Furthermore, the ideal ordering wavevector $\boldsymbol{q}$ (which is naturally soft as illustrated in Fig. 6.4) changes continuously as a function of density, analogous to the evolution of the nematic axis of the superconductor [20]. Such behavior is harder to rationalize for other rotation symmetry-breaking parent states such as stripes. So even without making any assumptions about the nature of the superconducting state, we can interpret the observations of Ref. [20] as

[14] This refers to the mean-field transition temperature $T_{\mathrm{MF}} \sim 50$ K which is related to exciton binding energies. There is a lower energy scale $T_{\mathrm{BKT}} \sim 7$ K controlled by the stiffness, above which the phase of the IKS is disordered (though likely still nematic).

indirect evidence for the IKS.

While the above evidence is reasonable, it remains to a degree circumstantial. $\hat{C}_{2x}$-like and $\hat{\mathcal{T}}$ symmetries preclude observable signatures like second harmonic generation and orbital magnetization. A more direct and definitive diagnostic for IKS order is possible in principle by detecting the Kekulé pattern at the AA regions directly using STM/STS. Kekulé order in monolayer graphene induced by mobile adatoms or substrate vacancies [238, 239] has been measured in Ref. [240], whereas Kekulé order induced by large (isotropic) strain [241, 242] has been observed in Ref. [243]. However, only a very small fraction of the total number of electrons, i.e. those occupying the central bands, participate in the IKS order. As a result, the signal coming from the graphene-scale $\sqrt{3} \times \sqrt{3}$ Kekulé pattern in the IKS will be significantly smaller than that seen in the above-mentioned monolayer experiments. On the other hand, the STM studies of Ref. [198, 199] were able to detect a Kekulé distortion in monolayer graphene in a high magnetic field at densities that are comparable to those of TBG. The theory here is based on the approximate $SU(4)$ symmetry of the zeroth Landau level, which is close in spirit to the $U(4) \times U(4)$ limit of TBG, but the anisotropies and associated mechanisms are different [244].

6.5 Outlook

By combining the results obtained in this chapter at non-zero integer fillings with the findings of Ref. [97] at neutrality, we conclude that by adding a small amount of uniaxial heterostrain to the interacting BM model, one obtains from self-consistent HF a global picture of the normal state TBG phase diagram that is compatible with many experimental observations at integer fillings. Furthermore as shown in Ref. [59], the doped descendants of the finite-strain integer orders examined here exhibit Landau fans and compressibility signatures that are consistent with those measured experimentally. A key player in the strained regime is IKS order which is associated with multiscale TSB. Together with strong coupling (QHFM-like) and weak coupling (BM dispersion dominated) treatments, this intermediate coupling perspective should form an important part of the umbrella of theoretical regimes used to understand the experimental phenomenology.

While the present analysis has predominantly relied on HF, the overall picture of the IKS in this chapter should be robust to fluctuations beyond mean-field theory. For instance, the strong coupling ferromagnetic ground states obtained in more sophisticated treatments are known to be remarkably close to single Slater determinants. On the other hand, the IKS has a soft ordering wavevector $\boldsymbol{q}$ and its projector has significant variations across the mBZ, suggesting it may benefit comparatively more from beyond-HF corrections. Therefore, adding fluctuations to the phase diagrams of Fig. 6.2 would only shift the IKS phase boundaries to the left. While this is a qualitative argument, we note that Ref. [245] has confirmed that the IKS is the ground state in DMRG at $|\nu| = 3$, and remains competitive even in the absence of strain.

Our results open up several interesting directions for future work. For example, a generalized Pomeranchuk effect has been observed in TBG [31, 34], which causes high-entropy insulators to win over metallic states with increasing temperature. It would be useful to analyze the finite-temperature properties and the collective mode spectrum of the IKS, and see if it can be fit into this Pomeranchuk scenario.

Arguably the most interesting direction for future work is to investigate the relation between the IKS and superconductivity. For example, the KIVC has recently been argued to be a natural parent state for superconductivity in Refs. [56]. As summarized in Chapter 5, that is a strong coupling scenario in which the topological structure of the bands facilitates the generation of preformed bosons. A future direction would be to adapt this mechanism to the IKS, or investigate whether local KIVC correlations are strong enough to allow the same mechanism to be operative. It would also be interesting to consider if a similar approach to coupling superconductivity via topological terms in Ref. [246, 247] could be generalized to the 'dominant lobe' physics of the IKS. Given the intermediate coupling nature of the IKS, a better approach may be to take a more Fermi surface oriented approach where details of the $\boldsymbol{q}$-dependent strain- and interaction-renormalized dispersion near E_F are important.

Chapter 7

Conclusions

In this thesis, we studied how the unique combination of topology and correlations in TBG can lead to a profusion of novel electronic phenomena. In Part I, we focused on three classes of excitations of the strong coupling correlated insulators at integer ν, where theoretical intuition can be gained via the close connections to QHFM, with the crucial generalization that narrow Chern bands of both $C = \pm 1$ are involved.

The first two classes arise from the $\nu = +3$ spin- and valley-polarized QAH insulator in hBN-aligned TBG. We demonstrated that for certain parameter regimes, the intervalley excitons in this system have a nearly flat dispersion and a non-trivial excitonic Chern number. In the Landau level limit, we proposed a new type of quantum Hall state, which can be understood as a Laughlin state of topological excitons constructed on top of the spontaneous QAH insulator. We also studied domain wall defects in the flavour and Chern polarization of the orbital ordering and their interplay with spatial variations in the sublattice potential. The topological structure of the underlying bands gives rise to different types of domain walls with distinct properties, and we showed that there can be close energetic competition between valley and Chern walls, which affects the global transport properties of the sample.

The third class of excitations is skyrmions, which can appear at other integer fillings and involve rotations in both spin and pseudospin space. Our focus was on even integer fillings, where singly-charged pseudospin skyrmions in opposite Chern sectors have previously been proposed to form charge-2e bound states, which can then condense to induce skyrmion-based superconductivity. We analyzed such paired skyrmions using HF

numerics, establishing that such binding in a microscopically realistic model is in principle possible. We also investigated the limitations of this mechanism, in particular the reliance on a moderately low chiral ratio, the filling factor dependence, and the sensitivity to details of the modelling.

In Part II, we uncovered an alternative paradigm for the integer orders, operative for moderate strain ratios well within experimental bounds, that is physically decoupled from the strong coupling perspective, yet distinct from weak coupling treatments of the BM model. At neutrality, the KIVC insulator gives way to the symmetric SM. However, at all non-zero integer fillings, we found the emergence of the IKS, whose defining characteristic is translational symmetry breaking at the graphene scale (Kekulé distortion) and the moiré scale (rotation of the Kekulé phase). We identified a 'lobe' mechanism in which the ordering wavevector $\boldsymbol{q}$ is selected by momentum-space details of the strain- and interaction-normalized dispersion. Hence, the strained phase diagrams can be understood as products of an intermediate coupling regime. We argued that the this picture is consistent with many experimental observations, and should be considered, along with the other prevailing theoretical approaches, when interpreting the experimental phenomenology.

A recurring theme throughout this thesis is the variability of TBG samples. Many factors could be at play—to name a few: twist angle, strain, substrate alignment, gate-screening distance, and impurities. Some are experimentally tunable, at least at an averaged level, while others, such as strain, are still beyond precise control. The upside is that TBG can be considered highly tunable, such that a plethora of vastly different phenomena can be obtained in a single material. On the other hand, there are plenty of confounding variables that could qualitatively influence physical signatures, and obfuscate the key underlying correlations and physics. A persistent issue, which is difficult to tame both theoretically and experimentally, is the often invisible spatial inhomogeneity in twist angle and strain. A successful program to understand the correlated phenomena in TBG would likely require careful synthesis of the smorgasbord of experimental and theoretical results accumulated so far, and future progress in disentangling the myriad of external factors.

While this thesis has concentrated on TBG, we must not forget that this material is part of a larger family of heterostructures whose members may have nominally different

phase diagrams, but are interlinked by the common thread of moiré physics. The ability for TBG to host such a diversity of correlated and topological phenomena is remarkable in its own right. However, more broadly, TBG can inspire novel phenomena, which may be relevant for other platforms. Examples briefly mentioned in this thesis include paired skyrmions in TTG, and topological excitons and many-body excitonic physics in QAH platforms with a richer layer structure.

Ultimately, the holy grail of TBG is an understanding of the mechanism(s) behind the (numerous) superconducting domes, which will undoubtedly continue to drive research efforts for a long time. Apart from the chapter on paired skyrmions, this thesis does not directly address this question, instead focusing on the topic of the integer normal orders and their properties and excitations, which is of course a worthy research area in its own right. However, we believe an improved understanding of the proximate correlated phases will also help guide and constrain interpretations of the superconducting phases, as has been the case for the high-T_c cuprates. Whether or not the similarities between the cuprate and TBG phase diagrams are physically significant remains to be seen.

Appendix A

$C_{\mathbf{exc}}$ in the Landau level limit

In the language of the magnetic Bloch basis, we can analytically compute the Berry curvature of the valley-flip exciton in the LLL in the absence of perturbations, since we know the analytical form of the envelope wavefunction. Recall the the form of the exciton creation operator $\gamma^\dagger_{q,m}$ for the m-th degenerate exciton level in the Landau gauge

$$\gamma^\dagger_{q,m} = \int dk\, \psi_{q,m}(k) b^\dagger(k,q) \tag{A.1}$$

$$b^\dagger(k,q) = c^\dagger_{k+q,-} c_{k,+} \tag{A.2}$$

$$\psi_{q,m}(k) \propto H_m\big[\sqrt{2}(k+\frac{q}{2})\big] e^{-(k+\frac{q}{2})^2} = \tilde{\psi}_m(k+\frac{q}{2}) \tag{A.3}$$

where H_m is the m-th Hermite polynomial. $\tilde{\psi}(k)$ is centered at the origin with mean zero. Now consider following magnetic Bloch operator for the exciton

$$\Gamma^\dagger_{\boldsymbol{q},m} \equiv \frac{1}{\sqrt{N_x}} \sum_n \gamma^\dagger_{q_y+2nQ,m} e^{-\frac{iq_x}{2}(q_y+2nQ)} \tag{A.4}$$

whose wavefunction is (after performing a PH transformation in the $\tau = +$ band)

$$\psi^{\text{exc}}_{\boldsymbol{q},m}(\boldsymbol{r}_e, \boldsymbol{r}_h) = \frac{1}{\sqrt{N_x}} \sum_n \int dk\, \tilde{\psi}_m(k)\, e^{-\frac{iq_x}{2}(q_y+2nQ)} \phi_{k+\frac{q_y}{2}+nQ,-}(\boldsymbol{r}_e) \phi^*_{k-\frac{q_y}{2}-nQ,+}(\boldsymbol{r}_h). \tag{A.5}$$

To verify that this is the right candidate, we check the magnetic Bloch theorem by shifting the exciton COM coordinate $\boldsymbol{R} = \frac{\boldsymbol{r}_e+\boldsymbol{r}_h}{2}$

$$\psi^{\text{exc}}_{\boldsymbol{q},m}(\boldsymbol{r}_e + a\hat{x}, \boldsymbol{r}_h + a\hat{x}) = e^{-i(2Q)\frac{y_e+y_h}{2}} e^{iq_x a}\psi^{\text{exc}}_{\boldsymbol{q},m}(\boldsymbol{r}_e, \boldsymbol{r}_h) \tag{A.6}$$

$$\psi^{\text{exc}}_{\boldsymbol{q},m}(\boldsymbol{r}_e + \frac{a}{2}\hat{y}, \boldsymbol{r}_h + \frac{a}{2}\hat{y}) = e^{iq_y\frac{a}{2}}\psi^{\text{exc}}_{\boldsymbol{q},m}(\boldsymbol{r}_e, \boldsymbol{r}_h). \tag{A.7}$$

In the first line, the factor of two in the phase $e^{-i(2Q)\frac{y_e+y_h}{2}}$ reflects the fact that the exciton has twice the coupling to the magnetic field. Therefore, the magnetic unit cell shrinks by a factor of two in the y-direction, so that the magnetic BZ of the exciton doubles in area.

The 'cell-periodic' part of the Bloch function is $u^{\text{exc}}_{\boldsymbol{q}}(\boldsymbol{r}_e, \boldsymbol{r}_h) = \exp\big(-i\boldsymbol{q}\cdot\frac{\boldsymbol{r}_e+\boldsymbol{r}_h}{2}\big)\psi^{\text{exc}}_{\boldsymbol{q}}(\boldsymbol{r}_e, \boldsymbol{r}_h)$, and we can straightforwardly compute the Berry connections

$$-i\langle u_{\boldsymbol{q}}|\,\partial_{q_x}|u_{\boldsymbol{q}}\rangle = 0, \quad -i\langle u_{\boldsymbol{q}}|\,\partial_{q_y}|u_{\boldsymbol{q}}\rangle = -\frac{q_x}{2} \tag{A.8}$$

leading to a curvature $f_{xy} = -\frac{1}{2}$. Integrated over the doubled magnetic BZ, this leads to $C_{\text{exc}} = -1$.

Appendix B

TDHFA for TBG

We describe the equations for computing the spin-flip and valley-flip exciton bands in TBG. Our approach is equivalent to diagonalizing in the subspace of single PH pairs in the relevant symmetry sector. We do not consider 'inter-band' excitons that are not charged under valley or spin.

We begin with a set of self-consistent HF band operators $d^\dagger_{\boldsymbol{k},\tau s a}$ associated with a QAH state $|\mathrm{HF}\rangle$ at $\nu = +3$, where τ, s refer to valley and spin. Since our 'active' subspace of the continuum model comprises the eight central bands, the HF band index takes values $a = +, -$. Without loss of generality, we assume that $|\mathrm{HF}\rangle$ is flavor polarized such that $d^\dagger_{\boldsymbol{k},K'\downarrow+}$ is the operator for the single unfilled band.

We first focus on intervalley excitons. Following the notation of Ref [121], we parameterize the exciton creation operator at momentum $\boldsymbol{q}$ as

$$Q^\dagger_\nu(\boldsymbol{q}) = \sum_{\boldsymbol{k}a} X^\nu_{\boldsymbol{k}a}(\boldsymbol{q}) d^\dagger_{\boldsymbol{k}+\boldsymbol{q},K'\downarrow+} d_{\boldsymbol{k},K\downarrow a}, \tag{B.1}$$

where ν labels the exciton branch. The exciton envelopes $X^\nu_{\boldsymbol{k}a}(\boldsymbol{q})$ and energies $\omega_\nu(\boldsymbol{q})$ are obtained by solving the eigenvalue equation

$$\sum_{\boldsymbol{k}'a'} A_{\boldsymbol{k}a;\boldsymbol{k}'a'}(\boldsymbol{q}) X^\nu_{\boldsymbol{k}'a}(\boldsymbol{q}) = \omega_\nu(\boldsymbol{q}) X^\nu_{\boldsymbol{k}a}(\boldsymbol{q}). \tag{B.2}$$

The matrix $A_{\boldsymbol{k}x;\boldsymbol{k}'y}(\boldsymbol{q})$ can be split into a 'single-particle' and an interaction piece.

The single-particle contribution is

$$A^{\mathrm{SP}}_{\boldsymbol{k}x;\boldsymbol{k'}y}(\boldsymbol{q}) = \delta_{\boldsymbol{k}\boldsymbol{k'}}(H^{\mathrm{SP}}_{\boldsymbol{k}+\boldsymbol{q},K'\downarrow;++}\delta_{xy} - H^{\mathrm{SP}}_{\boldsymbol{k},K\downarrow;yx}) \tag{B.3}$$

where the effective single-particle Hamiltonian H^{SP} is off-diagonal only in HF band index. This includes the BM term, the external sublattice potential, as well as the interaction subtraction term.

The interaction piece is

$$A^{\mathrm{int}}_{\boldsymbol{k}x;\boldsymbol{k'}y}(\boldsymbol{q}) = \delta_{\boldsymbol{k}\boldsymbol{k'}}\sum_{\boldsymbol{p}a} V^{\boldsymbol{p}K\downarrow a;\boldsymbol{k}K\downarrow y}_{\boldsymbol{p}K\downarrow a;\boldsymbol{k}K\downarrow x} - \delta_{\boldsymbol{k}\boldsymbol{k'}}\delta_{xy}\sum_{\boldsymbol{p}} V^{\boldsymbol{k}+\boldsymbol{q},K'\downarrow+;\boldsymbol{p}K'\downarrow-}_{\boldsymbol{k}+\boldsymbol{q},K'\downarrow+;\boldsymbol{p}K'\downarrow-} \tag{B.4}$$

$$+ \delta_{\boldsymbol{k}\boldsymbol{k'}}\sum_{\boldsymbol{p}\tau sa}\left(\delta_{xy}V^{\boldsymbol{k}+\boldsymbol{q},K'\downarrow+;\boldsymbol{p}\tau sa}_{\boldsymbol{p}\tau sa;\boldsymbol{k}+\boldsymbol{q},K'\downarrow+} - V^{\boldsymbol{k}K\downarrow y;\boldsymbol{p}\tau sa}_{\boldsymbol{p}\tau sa;\boldsymbol{k}K\downarrow x}\right) n_{\tau sa} \tag{B.5}$$

$$- V^{\boldsymbol{k}+\boldsymbol{q},K'\downarrow+;\boldsymbol{k'}K\downarrow y}_{\boldsymbol{k}K\downarrow x;\boldsymbol{k'}+\boldsymbol{q},K'\downarrow+} \tag{B.6}$$

where $V^{\alpha;\beta}_{\gamma;\delta} = \langle\alpha;\beta|\,\hat{V}\,|\delta;\gamma\rangle$ is the interaction matrix element and $n_{\tau sa}$ is 1 if the band is filled and 0 otherwise. The first line above reflects the loss of exchange energy of the created hole and the gain of exchange energy of the added electron. The second line accounts for the interaction of the PH pair with the filled active bands. The third line describes the mutual interaction of the electron and the hole.

The corresponding expressions for the spin-flip exciton are

$$Q^{\dagger}_{\nu}(\boldsymbol{q}) = \sum_{\boldsymbol{k}a} X^{\nu}_{\boldsymbol{k}a}(\boldsymbol{q})d^{\dagger}_{\boldsymbol{k}+\boldsymbol{q},K'\downarrow+}d_{\boldsymbol{k},K'\uparrow a} \tag{B.7}$$

$$A^{\mathrm{SP}}_{\boldsymbol{k}x;\boldsymbol{k'}y}(\boldsymbol{q}) = \delta_{\boldsymbol{k}\boldsymbol{k'}}(H^{\mathrm{SP}}_{\boldsymbol{k}+\boldsymbol{q},K'\downarrow;++}\delta_{xy} - H^{\mathrm{SP}}_{\boldsymbol{k},K'\uparrow;yx}) \tag{B.8}$$

$$A^{\mathrm{int}}_{\boldsymbol{k}x;\boldsymbol{k'}y}(\boldsymbol{q}) = \delta_{\boldsymbol{k}\boldsymbol{k'}}\sum_{\boldsymbol{p}a} V^{\boldsymbol{p}K'\uparrow a;\boldsymbol{k}K'\uparrow y}_{\boldsymbol{p}K'\uparrow a;\boldsymbol{k}K'\uparrow x} - \delta_{\boldsymbol{k}\boldsymbol{k'}}\delta_{xy}\sum_{\boldsymbol{p}} V^{\boldsymbol{k}+\boldsymbol{q},K'\downarrow+;\boldsymbol{p}K'\downarrow-}_{\boldsymbol{k}+\boldsymbol{q},K'\downarrow+;\boldsymbol{p}K'\downarrow-} \tag{B.9}$$

$$+ \delta_{\boldsymbol{k}\boldsymbol{k'}}\sum_{\boldsymbol{p}\tau sa}\left(\delta_{xy}V^{\boldsymbol{k}+\boldsymbol{q},K'\downarrow+;\boldsymbol{p}\tau sa}_{\boldsymbol{p}\tau sa;\boldsymbol{k}+\boldsymbol{q},K'\downarrow+} - V^{\boldsymbol{k}K'\uparrow y;\boldsymbol{p}\tau sa}_{\boldsymbol{p}\tau sa;\boldsymbol{k}K'\uparrow x}\right) n_{\tau sa} \tag{B.10}$$

$$- V^{\boldsymbol{k}+\boldsymbol{q},K'\downarrow+;\boldsymbol{k'}K'\uparrow y}_{\boldsymbol{k}K'\uparrow x;\boldsymbol{k'}+\boldsymbol{q},K'\downarrow+}. \tag{B.11}$$

Appendix C

Domain wall Ginzburg-Landau theory

The effective strong-coupling NLSM is described in terms of a basis of eight states corresponding to sublattice ($\sigma = A, B$), valley ($\tau = K, K'$), and spin ($s =\uparrow, \downarrow$) degrees of freedom. We let α, β be combined indices. The states are naturally divided into Chern sectors $C = \sigma_z\tau_z$. Consider starting from a uniform insulating/semimetallic Slater determinant state at filling ν described by projector $P(\boldsymbol{k})$. The energy of long-wavelength fluctuations of this state can be described using the following energy functional derived in Refs. [56, 160] in terms of the matrix-valued field $Q = 2P - 1$

$$\begin{aligned} E\left[\tilde{Q}(\boldsymbol{r})\right] =& \frac{\rho}{8}\mathrm{tr}(\nabla\tilde{Q})^2 - \frac{\alpha}{4}\mathrm{tr}(\tilde{Q}\gamma_z)^2 - \frac{\Delta(\boldsymbol{r})}{2}\mathrm{tr}(\tilde{Q}\gamma_z\eta_z) \\ &+ \frac{J}{8}\mathrm{tr}[(\tilde{Q}\gamma_x)^2 + (\tilde{Q}\gamma_y)^2] - \frac{\lambda}{8}\mathrm{tr}[(\tilde{Q}\gamma_x\eta_z)^2 + (\tilde{Q}\gamma_y\eta_z)^2] \\ Q_{\alpha\beta}(\boldsymbol{k}) &= \langle[c^\dagger_{\boldsymbol{k}\beta}, c_{\boldsymbol{k}\alpha}]\rangle, \quad Q(\boldsymbol{k})^2 = 1, \quad \mathrm{tr}Q(\boldsymbol{k}) = 2\nu. \end{aligned} \tag{C.1}$$

The dynamical term has been omitted above. $\tilde{Q}$ is related to Q by a $\boldsymbol{k}$-dependent transformation, which accounts for the momentum-space vortices when performing inter-Chern rotations [160]. Ground states therefore involve a $\boldsymbol{k}$-independent uniform $\tilde{Q}$. The first term is a gradient cost derived in the $U(8)$-symmetric limit (this can be done exactly if the Berry curvature is concentrated at a point). The non-symmetric terms in the Hamiltonian are incorporated primarily as mass terms, but they can also make the stiffness

Basis State	$\sigma_z = \gamma_z\eta_z$	$\tau_z = \eta_z$	$C = \gamma_z$	CP^3 field w
KA	$+1$	$+1$	$+1$	$(1,0,0,0)$
$K'A$	$+1$	-1	-1	$(0,1,0,0)$
KB	-1	$+1$	-1	$(0,0,1,0)$
$K'B$	-1	-1	$+1$	$(0,0,0,1)$

Table C.1: Basis states relevant for domain walls.

anisotropic in the $\tilde{Q}$-manifold. The α-term reflects the energetic penalty of inter-Chern coherence due to the vortex lattice [79, 160]. To account for the external sublattice potential, we have added a linear term with coefficient $\Delta(\boldsymbol{r})$, which acts as an effective sublattice mass.

We consider the spinless problem for simplicity, and work at $\nu = -1$ (this corresponds to one filled central band—the discussion for $\nu = 1$ is analogous since it involves specifying one empty band). This allows us to define a CP^3 field via $d^\dagger_{\boldsymbol{k}} = \sum_\alpha w_\alpha c^\dagger_{\boldsymbol{k}\alpha}$ where d is the operator for the filled band. This leads to $Q_{\alpha\beta} = 2w_\alpha w^*_\beta - \delta_{\alpha\beta}$.

We now show how the NLSM may reduce to a CP^1 theory when discussing domain walls in the large α limit. Table C shows the properties of the basis states. We consider each configuration in turn. While α may not actually be much larger than J, λ, considering a dominant α-term is a useful organizing principle since it emphasizes the (spinless) $U(2) \times U(2)$ division into Chern sectors.

1. **Uniform solution**: Consider first the case of zero sublattice mass. The α-term forces us to choose a Chern sector $\gamma_z = \pm 1$ to place our filled band in. Within a given Chern sector, we are left with an effective CP^1 field. This reflects the fact that $CP^1_{\gamma_z=1} \times CP^1_{\gamma_z=-1}$ can be embedded into CP^3. For instance for $\gamma_z = 1$, we have $w = (\cos\frac{\theta}{2}, 0, 0, e^{i\phi}\sin\frac{\theta}{2})$. The J, λ terms vanish for this set of states. Hence at this order in the field theory, the uniform QAH ($\theta = 0, \pi$) and intervalley coherent states (in-plane) are degenerate. A finite sublattice mass will break this degeneracy by selecting the state with the correct sublattice polarization[1]. Hence there are two degenerate ground states labelled by the Chern number γ_z.

2. **Valley wall**: A sign-changing substrate $\sim \sigma_z$ means that we are forced to rotate

[1] Considering even smaller terms in perturbation theory, such as those arising from the antisymmetric tunneling t_A, reveals that the valley polarized state is energetically preferred [83] even in the absence of an external Δ.

from $\{KA, K'A\}$ to $\{KB, K'B\}$ between the bulks. To satisfy the α-term, we should only rotate within the same Chern sector γ_z—this automatically means we switch valley across the wall. Hence we are again left with an effective CP^1 field (with the same $CP^1_{\gamma_z=1} \times CP^1_{\gamma_z=-1}$ embedding as in the discussion for the uniform solution). The J, λ terms do not contribute. Therefore the CP^1 theory (which can be recast into a unit 3-vector $\boldsymbol{n} = \langle \boldsymbol{\eta} \rangle$) involves just the stiffness term and the out-of-plane sublattice term

$$E[\boldsymbol{n}(\boldsymbol{r})] = \frac{\rho_v}{4}(\nabla \boldsymbol{n})^2 - \alpha - \gamma_z \Delta(\boldsymbol{r}) n_z. \tag{C.2}$$

3. **Chern wall**: A sign-changing substrate $\sim \sigma_z$ means that we are forced to rotate from $\{KA, K'A\}$ to $\{KB, K'B\}$ between the bulks. This time the α-term cannot be fully satisfied because by definition the Chern wall rotates between Chern sectors. Consider for concreteness that the left and right bulks are in KA and KB respectively. The most natural rotation is within the $\{KA, KB\}$ subspace, which would allow for a CP^1 description. In principle nothing stops the system from rotating into the other valley as well. However this would be energetically disadvantageous due to the stiffness term—if the J, λ are small then the minimal configuration should involve traversing the shortest path between KA and KB to reduce the gradient cost. In this case, $\tilde{Q}$ commutes with η_z, so that the J and λ terms act to largely cancel each other out. In this limit, the CP^1 theory (which can be recast into a unit 3-vector $\boldsymbol{m} = \langle \boldsymbol{\gamma} \rangle$) involves the stiffness term, the easy axis α-term, and the substrate term

$$E[\boldsymbol{m}(\boldsymbol{r})] = \frac{\rho_s}{4}(\nabla \boldsymbol{m})^2 - \alpha m_z^2 + \frac{\lambda - J}{2}(m_z^2 - 1) - \eta_z \Delta(\boldsymbol{r}) m_z. \tag{C.3}$$

Note that this involves a different $CP^1_{\eta_z=1} \times CP^1_{\eta_z=-1}$ embedding than the valley wall. We have used a different stiffness ρ_s than the valley wall since this is generically allowed by the symmetries.

Comparing the effective CP^1 theories for the Chern wall and the valley wall, the only difference (ignoring the $J - \lambda$ contribution) is that the easy-axis anisotropy

term of the Chern wall is frustrated with the stiffness term, while the anistropy term of the valley wall is always satisfied. This would seem to suggest that the valley wall should always be energetically better than the Chern wall. However what this simple analysis does not capture is that the Chern wall does not actually rotate from complete A to B sublattice polarization. If it did, then the exchange physics would be the same as the valley wall (since the interaction is density-density in layer, sublattice, spin and valley space). But the actual HF bulks for the Chern wall have finite overlap due to partial sublattice polarization, and hence finite inter-domain exchange. This counteracts the anisotropy cost, and helps facilitate Chern-valley DW competition.

4. **Intertwined wall**: Since the sublattice mass is of constant sign, the bulks have the same fixed value of σ_z. However for this class of solutions, we require the system to rotate between valleys. Similar considerations to the Chern wall lead to yet another $CP^1_{\sigma_z=1} \times CP^1_{\sigma_z=-1}$ embedding, where here each CP^1 is restricted to a fixed sublattice, so that the 3-vector can be given by $\boldsymbol{t} = \langle \boldsymbol{\tau} \rangle$

$$E[\boldsymbol{t}(\boldsymbol{r})] = \frac{\rho_t}{4}(\nabla \boldsymbol{t})^2 - \alpha t_z^2 - \sigma_z \Delta(\boldsymbol{r}). \tag{C.4}$$

While the different CP^1 theories provide adequate descriptions of each individual DW, it is instructive to construct an approximate Ginzburg-Landau theory that can incorporate multiple DWs into a single formulation. We focus on the valley and Chern walls that were described by $O(3)$ vectors $\langle \boldsymbol{\eta} \rangle$ and $\langle \boldsymbol{\gamma} \rangle$. Consider a sign-changing substrate that flips sign at $x = 0$. Starting in KA for $x \to -\infty$, the valley wall wants to end up in $K'B$ while the Chern wall wants to end up in KB. The intra-Chern rotation of the valley wall can again be described by the vector $\boldsymbol{n} \sim \langle \boldsymbol{\eta} \rangle$, which has the interpretation of a Chern-filtered valley polarization. However due to the strong α-term, the field $\langle \boldsymbol{\gamma} \rangle$, which involves inter-Chern rotations, can be approximated as an Ising field m_z. This can be roughly thought of as the order parameter corresponding to the Chern number. The substrate term can then be summarized as the coupling $\Delta(\boldsymbol{r}) n_z m_z$ between the order parameters. A phenomenological Ginzburg-Landau free energy density that accounts for

the stiffnesses, easy-axis anisotropy, and substrate coupling is

$$f \sim \rho_s \left[(\nabla m_z)^2 + \frac{(m_z^2 - 1)^2}{\beta^2 a_{\mathrm{M}}^2} \right] + \rho_v (\nabla \boldsymbol{n})^2 - \frac{\Delta(\vec{r})}{a_{\mathrm{M}}^2} m_z n_z. \tag{C.5}$$

Various parameters have been rescaled by the moiré length.

Bibliography

[1] A. K. Geim and I. V. Grigorieva. Van der Waals heterostructures. *Nature*, 499(7459):419–425, July 2013. doi:10.1038/nature12385.

[2] K. S. Novoselov, A. Mishchenko, A. Carvalho, and A. H. Castro Neto. 2D materials and van der Waals heterostructures. *Science*, 353(6298), July 2016. doi:10.1126/science.aac9439.

[3] K. S. Novoselov, D. Jiang, F. Schedin, T. J. Booth, V. V. Khotkevich, S. V. Morozov, and A. K. Geim. Two-dimensional atomic crystals. *Proceedings of the National Academy of Sciences*, 102(30):10451–10453, July 2005. doi:10.1073/pnas.0502848102.

[4] Yuan Cao, Valla Fatemi, Ahmet Demir, Shiang Fang, Spencer L. Tomarken, Jason Y. Luo, Javier D. Sanchez-Yamagishi, Kenji Watanabe, Takashi Taniguchi, Efthimios Kaxiras, Ray C. Ashoori, and Pablo Jarillo-Herrero. Correlated insulator behaviour at half-filling in magic-angle graphene superlattices. *Nature*, 556(7699):80–84, March 2018. doi:10.1038/nature26154.

[5] Yuan Cao, Valla Fatemi, Shiang Fang, Kenji Watanabe, Takashi Taniguchi, Efthimios Kaxiras, and Pablo Jarillo-Herrero. Unconventional superconductivity in magic-angle graphene superlattices. *Nature*, 556(7699):43–50, March 2018. doi:10.1038/nature26160.

[6] A. H. Castro Neto, F. Guinea, N. M. R. Peres, K. S. Novoselov, and A. K. Geim. The electronic properties of graphene. *Reviews of Modern Physics*, 81(1):109–162, January 2009. doi:10.1103/revmodphys.81.109.

[7] J. M. B. Lopes dos Santos, N. M. R. Peres, and A. H. Castro Neto. Graphene bilayer with a twist: Electronic structure. *Physical Review Letters*, 99(25), December 2007. doi:10.1103/physrevlett.99.256802.

[8] G. Trambly de Laissardière, D. Mayou, and L. Magaud. Localization of Dirac electrons in rotated graphene bilayers. *Nano Letters*, 10(3):804–808, February 2010. doi:10.1021/nl902948m.

[9] Rafi Bistritzer and Allan H. MacDonald. Moiré bands in twisted double-layer graphene. *Proceedings of the National Academy of Sciences*, 108(30):12233–12237, July 2011. doi:10.1073/pnas.1108174108.

[10] J. M. B. Lopes dos Santos, N. M. R. Peres, and A. H. Castro Neto. Continuum model of the twisted graphene bilayer. *Physical Review B*, 86(15), October 2012. doi:10.1103/physrevb.86.155449.

[11] Guohong Li, A. Luican, J. M. B. Lopes dos Santos, A. H. Castro Neto, A. Reina, J. Kong, and E. Y. Andrei. Observation of Van Hove singularities in twisted graphene layers. *Nature Physics*, 6(2):109–113, November 2009. doi:10.1038/nphys1463.

[12] A. Luican, Guohong Li, A. Reina, J. Kong, R. R. Nair, K. S. Novoselov, A. K. Geim, and E. Y. Andrei. Single-layer behavior and its breakdown in twisted graphene layers. *Physical Review Letters*, 106(12), March 2011. doi:10.1103/physrevlett.106.126802.

[13] I. Brihuega, P. Mallet, H. González-Herrero, G. Trambly de Laissardière, M. M. Ugeda, L. Magaud, J. M. Gómez-Rodríguez, F. Ynduráin, and J.-Y. Veuillen. Unraveling the intrinsic and robust nature of van Hove singularities in twisted bilayer graphene by scanning tunneling microscopy and theoretical analysis. *Physical Review Letters*, 109(19), November 2012. doi:10.1103/physrevlett.109.196802.

[14] Yuan Cao, Debanjan Chowdhury, Daniel Rodan-Legrain, Oriol Rubies-Bigorda, Kenji Watanabe, Takashi Taniguchi, T. Senthil, and Pablo Jarillo-Herrero. Strange metal in magic-angle graphene with near Planckian dissipation. *Physical Review Letters*, 124(7), February 2020. doi:10.1103/physrevlett.124.076801.

[15] Hryhoriy Polshyn, Matthew Yankowitz, Shaowen Chen, Yuxuan Zhang, K. Watanabe, T. Taniguchi, Cory R. Dean, and Andrea F. Young. Large linear-in-temperature resistivity in twisted bilayer graphene. *Nature Physics*, 15(10):1011–1016, August 2019. doi:10.1038/s41567-019-0596-3.

[16] Jeong Min Park, Yuan Cao, Kenji Watanabe, Takashi Taniguchi, and Pablo Jarillo-Herrero. Flavour hund's coupling, Chern gaps and charge diffusivity in moiré graphene. *Nature*, 592(7852):43–48, March 2021. doi:10.1038/s41586-021-03366-w.

[17] Alexandre Jaoui, Ipsita Das, Giorgio Di Battista, Jaime Díez-Mérida, Xiaobo Lu, Kenji Watanabe, Takashi Taniguchi, Hiroaki Ishizuka, Leonid Levitov, and Dmitri K. Efetov. Quantum critical behavior in magic-angle twisted bilayer graphene, 2021. URL: https://arxiv.org/abs/2108.07753, doi:10.48550/ARXIV.2108.07753.

[18] Myungchul Oh, Kevin P. Nuckolls, Dillon Wong, Ryan L. Lee, Xiaomeng Liu, Kenji Watanabe, Takashi Taniguchi, and Ali Yazdani. Evidence for unconventional superconductivity in twisted bilayer graphene. *Nature*, 600(7888):240–245, October 2021. doi:10.1038/s41586-021-04121-x.

[19] Hyunjin Kim, Youngjoon Choi, Cyprian Lewandowski, Alex Thomson, Yiran Zhang, Robert Polski, Kenji Watanabe, Takashi Taniguchi, Jason Alicea, and Stevan Nadj-Perge. Spectroscopic signatures of strong correlations and unconventional superconductivity in twisted trilayer graphene, 2021. URL: https://arxiv.org/abs/2109.12127, doi:10.48550/ARXIV.2109.12127.

[20] Yuan Cao, Daniel Rodan-Legrain, Jeong Min Park, Noah F. Q. Yuan, Kenji Watanabe, Takashi Taniguchi, Rafael M. Fernandes, Liang Fu, and Pablo Jarillo-Herrero. Nematicity and competing orders in superconducting magic-angle graphene. *Science*, 372(6539):264–271, April 2021. doi:10.1126/science.abc2836.

[21] Jeong Min Park, Yuan Cao, Liqiao Xia, Shuwen Sun, Kenji Watanabe, Takashi Taniguchi, and Pablo Jarillo-Herrero. Magic-angle multilayer graphene: A robust family of moiré superconductors, 2021. URL: https://arxiv.org/abs/2112.10760, doi:10.48550/ARXIV.2112.10760.

[22] Matthew Yankowitz, Shaowen Chen, Hryhoriy Polshyn, Yuxuan Zhang, K. Watanabe, T. Taniguchi, David Graf, Andrea F. Young, and Cory R. Dean. Tuning superconductivity in twisted bilayer graphene. *Science*, 363(6431):1059–1064, March 2019. doi:10.1126/science.aav1910.

[23] Petr Stepanov, Ipsita Das, Xiaobo Lu, Ali Fahimniya, Kenji Watanabe, Takashi Taniguchi, Frank H. L. Koppens, Johannes Lischner, Leonid Levitov, and Dmitri K. Efetov. Untying the insulating and superconducting orders in magic-angle graphene. *Nature*, 583(7816):375–378, July 2020. doi:10.1038/s41586-020-2459-6.

[24] Yu Saito, Jingyuan Ge, Kenji Watanabe, Takashi Taniguchi, and Andrea F. Young. Independent superconductors and correlated insulators in twisted bilayer graphene. *Nature Physics*, 16(9):926–930, June 2020. doi:10.1038/s41567-020-0928-3.

[25] Xiaoxue Liu, Zhi Wang, K. Watanabe, T. Taniguchi, Oskar Vafek, and J. I. A. Li. Tuning electron correlation in magic-angle twisted bilayer graphene using Coulomb screening. *Science*, 371(6535):1261–1265, March 2021. doi:10.1126/science.abb8754.

[26] Xiaobo Lu, Petr Stepanov, Wei Yang, Ming Xie, Mohammed Ali Aamir, Ipsita Das, Carles Urgell, Kenji Watanabe, Takashi Taniguchi, Guangyu Zhang, Adrian Bachtold, Allan H. MacDonald, and Dmitri K. Efetov. Superconductors, orbital magnets and correlated states in magic-angle bilayer graphene. *Nature*, 574(7780):653–657, October 2019. doi:10.1038/s41586-019-1695-0.

[27] Aaron L. Sharpe, Eli J. Fox, Arthur W. Barnard, Joe Finney, Kenji Watanabe, Takashi Taniguchi, M. A. Kastner, and David Goldhaber-Gordon. Emergent ferromagnetism near three-quarters filling in twisted bilayer graphene. *Science*, 365(6453):605–608, August 2019. doi:10.1126/science.aaw3780.

[28] M. Serlin, C. L. Tschirhart, H. Polshyn, Y. Zhang, J. Zhu, K. Watanabe, T. Taniguchi, L. Balents, and A. F. Young. Intrinsic quantized anomalous Hall effect in a moiré heterostructure. *Science*, 367(6480):900–903, February 2020. doi:10.1126/science.aay5533.

[29] U. Zondiner, A. Rozen, D. Rodan-Legrain, Y. Cao, R. Queiroz, T. Taniguchi, K. Watanabe, Y. Oreg, F. von Oppen, Ady Stern, E. Berg, P. Jarillo-Herrero, and S. Ilani. Cascade of phase transitions and Dirac revivals in magic-angle graphene. *Nature*, 582(7811):203–208, June 2020. doi:10.1038/s41586-020-2373-y.

[30] A. Uri, S. Grover, Y. Cao, J. A. Crosse, K. Bagani, D. Rodan-Legrain, Y. Myasoedov, K. Watanabe, T. Taniguchi, P. Moon, M. Koshino, P. Jarillo-Herrero, and E. Zeldov. Mapping the twist-angle disorder and Landau levels in magic-angle graphene. *Nature*, 581(7806):47–52, May 2020. doi:10.1038/s41586-020-2255-3.

[31] Yu Saito, Fangyuan Yang, Jingyuan Ge, Xiaoxue Liu, Takashi Taniguchi, Kenji Watanabe, J. I. A. Li, Erez Berg, and Andrea F. Young. Isospin Pomeranchuk effect in twisted bilayer graphene. *Nature*, 592(7853):220–224, April 2021. doi:10.1038/s41586-021-03409-2.

[32] Shuang Wu, Zhenyuan Zhang, K. Watanabe, T. Taniguchi, and Eva Y. Andrei. Chern insulators, van Hove singularities and topological flat bands in magic-angle twisted bilayer graphene. *Nature Materials*, 20(4):488–494, February 2021. doi:10.1038/s41563-020-00911-2.

[33] Yu Saito, Jingyuan Ge, Louk Rademaker, Kenji Watanabe, Takashi Taniguchi, Dmitry A. Abanin, and Andrea F. Young. Hofstadter subband ferromagnetism and symmetry-broken Chern insulators in twisted bilayer graphene. *Nature Physics*, 17(4):478–481, January 2021. doi:10.1038/s41567-020-01129-4.

[34] Asaf Rozen, Jeong Min Park, Uri Zondiner, Yuan Cao, Daniel Rodan-Legrain, Takashi Taniguchi, Kenji Watanabe, Yuval Oreg, Ady Stern, Erez Berg, Pablo Jarillo-Herrero, and Shahal Ilani. Entropic evidence for a Pomeranchuk effect in magic-angle graphene. *Nature*, 592(7853):214–219, April 2021. doi:10.1038/s41586-021-03319-3.

[35] Andrew T. Pierce, Yonglong Xie, Jeong Min Park, Eslam Khalaf, Seung Hwan Lee, Yuan Cao, Daniel E. Parker, Patrick R. Forrester, Shaowen Chen, Kenji Watanabe, Takashi Taniguchi, Ashvin Vishwanath, Pablo Jarillo-Herrero, and Amir Yacoby. Unconventional sequence of correlated Chern insulators in magic-angle twisted bilayer graphene. *Nature Physics*, 17(11):1210–1215, September 2021. doi:10.1038/s41567-021-01347-4.

[36] S. L. Tomarken, Y. Cao, A. Demir, K. Watanabe, T. Taniguchi, P. Jarillo-Herrero, and R. C. Ashoori. Electronic compressibility of magic-angle graphene superlattices. *Physical Review Letters*, 123(4), July 2019. doi:10.1103/physrevlett.123.046601.

[37] Jiachen Yu, Benjamin A. Foutty, Zhaoyu Han, Mark E. Barber, Yoni Schattner, Kenji Watanabe, Takashi Taniguchi, Philip Phillips, Zhi-Xun Shen, Steven A. Kivelson, and Benjamin E. Feldman. Correlated Hofstadter spectrum and flavor phase diagram in magic angle graphene, 2021. URL: https://arxiv.org/abs/2108.00009, doi:10.48550/ARXIV.2108.00009.

[38] Dillon Wong, Kevin P. Nuckolls, Myungchul Oh, Biao Lian, Yonglong Xie, Sangjun Jeon, Kenji Watanabe, Takashi Taniguchi, B. Andrei Bernevig, and Ali Yazdani. Cascade of electronic transitions in magic-angle twisted bilayer graphene. *Nature*, 582(7811):198–202, June 2020. doi:10.1038/s41586-020-2339-0.

[39] Youngjoon Choi, Hyunjin Kim, Yang Peng, Alex Thomson, Cyprian Lewandowski, Robert Polski, Yiran Zhang, Harpreet Singh Arora, Kenji Watanabe, Takashi Taniguchi, Jason Alicea, and Stevan Nadj-Perge. Correlation-driven topological phases in magic-angle twisted bilayer graphene. *Nature*, 589(7843):536–541, January 2021. doi:10.1038/s41586-020-03159-7.

[40] Youngjoon Choi, Hyunjin Kim, Cyprian Lewandowski, Yang Peng, Alex Thomson, Robert Polski, Yiran Zhang, Kenji Watanabe, Takashi Taniguchi, Jason Alicea, and Stevan Nadj-Perge. Interaction-driven band flattening and correlated phases in twisted bilayer graphene, 2021. URL: https://arxiv.org/abs/2102.02209, doi:10.48550/ARXIV.2102.02209.

[41] Alexander Kerelsky, Leo J. McGilly, Dante M. Kennes, Lede Xian, Matthew Yankowitz, Shaowen Chen, K. Watanabe, T. Taniguchi, James Hone, Cory Dean, Angel Rubio, and Abhay N. Pasupathy. Maximized electron interactions at the magic angle in twisted bilayer graphene. *Nature*, 572(7767):95–100, July 2019. doi:10.1038/s41586-019-1431-9.

[42] Youngjoon Choi, Jeannette Kemmer, Yang Peng, Alex Thomson, Harpreet Arora, Robert Polski, Yiran Zhang, Hechen Ren, Jason Alicea, Gil Refael, Felix von Oppen, Kenji Watanabe, Takashi Taniguchi, and Stevan Nadj-Perge. Electronic correlations in twisted bilayer graphene near the magic angle. *Nature Physics*, 15(11):1174–1180, August 2019. doi:10.1038/s41567-019-0606-5.

[43] Yonglong Xie, Biao Lian, Berthold Jäck, Xiaomeng Liu, Cheng-Li Chiu, Kenji Watanabe, Takashi Taniguchi, B. Andrei Bernevig, and Ali Yazdani. Spectroscopic signatures of many-body correlations in magic-angle twisted bilayer graphene. *Nature*, 572(7767):101–105, July 2019. doi:10.1038/s41586-019-1422-x.

[44] Liujun Zou, Hoi Chun Po, Ashvin Vishwanath, and T. Senthil. Band structure of twisted bilayer graphene: Emergent symmetries, commensurate approximants, and Wannier obstructions. *Physical Review B*, 98(8), August 2018. doi:10.1103/physrevb.98.085435.

[45] Zhida Song, Zhijun Wang, Wujun Shi, Gang Li, Chen Fang, and B. Andrei Bernevig. All magic angles in twisted bilayer graphene are topological. *Physical Review Letters*, 123(3), July 2019. doi:10.1103/physrevlett.123.036401.

[46] Junyeong Ahn, Sungjoon Park, and Bohm-Jung Yang. Failure of Nielsen-Ninomiya theorem and fragile topology in two-dimensional systems with space-time inversion symmetry: Application to twisted bilayer graphene at magic angle. *Physical Review X*, 9(2), April 2019. doi:10.1103/physrevx.9.021013.

[47] Chun-Chih Tseng, Xuetao Ma, Zhaoyu Liu, Kenji Watanabe, Takashi Taniguchi, Jiun-Haw Chu, and Matthew Yankowitz. Anomalous Hall effect at half filling in twisted bilayer graphene, 2022. URL: https://arxiv.org/abs/2202.01734, doi:10.48550/ARXIV.2202.01734.

[48] Petr Stepanov, Ming Xie, Takashi Taniguchi, Kenji Watanabe, Xiaobo Lu, Allan H. MacDonald, B. Andrei Bernevig, and Dmitri K. Efetov. Competing zero-field Chern insulators in superconducting twisted bilayer graphene. *Physical Review Letters*, 127(19), November 2021. doi:10.1103/physrevlett.127.197701.

[49] Kevin P. Nuckolls, Myungchul Oh, Dillon Wong, Biao Lian, Kenji Watanabe, Takashi Taniguchi, B. Andrei Bernevig, and Ali Yazdani. Strongly correlated Chern insulators in magic-angle twisted bilayer graphene. *Nature*, 588(7839):610–615, December 2020. doi:10.1038/s41586-020-3028-8.

[50] Ipsita Das, Xiaobo Lu, Jonah Herzog-Arbeitman, Zhi-Da Song, Kenji Watanabe, Takashi Taniguchi, B. Andrei Bernevig, and Dmitri K. Efetov. Symmetry-broken Chern insulators and Rashba-like Landau-level crossings in magic-angle bilayer graphene. *Nature Physics*, 17(6):710–714, March 2021. doi:10.1038/s41567-021-01186-3.

[51] Ipsita Das, Cheng Shen, Alexandre Jaoui, Jonah Herzog-Arbeitman, Aaron Chew, Chang-Woo Cho, Kenji Watanabe, Takashi Taniguchi, Benjamin A. Piot, B. Andrei Bernevig, and Dmitri K. Efetov. Observation of re-entrant correlated insulators and interaction driven Fermi surface reconstructions at one magnetic flux quantum per moiré unit cell in magic-angle twisted bilayer graphene, 2021. URL: https://arxiv.org/abs/2111.11341, doi:10.48550/ARXIV.2111.11341.

[52] Yonglong Xie, Andrew T. Pierce, Jeong Min Park, Daniel E. Parker, Eslam Khalaf, Patrick Ledwith, Yuan Cao, Seung Hwan Lee, Shaowen Chen, Patrick R. Forrester, Kenji Watanabe, Takashi Taniguchi, Ashvin Vishwanath, Pablo Jarillo-Herrero, and Amir Yacoby. Fractional Chern insulators in magic-angle twisted bilayer graphene. *Nature*, 600(7889):439–443, December 2021. doi:10.1038/s41586-021-04002-3.

[53] Yves H. Kwan, Yichen Hu, Steven H. Simon, and S. A. Parameswaran. Exciton band topology in spontaneous quantum anomalous Hall insulators: Applications to twisted bilayer graphene. *Phys. Rev. Lett.*, 126:137601, Mar 2021. URL: https://link.aps.org/doi/10.1103/PhysRevLett.126.137601, doi:10.1103/PhysRevLett.126.137601.

[54] Yves H. Kwan, Yichen Hu, Steven H. Simon, and S. A. Parameswaran. Excitonic fractional quantum Hall hierarchy in moiré heterostructures, 2020. *To appear in PRB*. URL: https://arxiv.org/abs/2003.11559, doi:10.48550/ARXIV.2003.11559.

[55] Yves H. Kwan, Glenn Wagner, Nilotpal Chakraborty, Steven H. Simon, and S. A. Parameswaran. Domain wall competition in the Chern insulating regime of twisted bilayer graphene. *Physical Review B*, 104(11), September 2021. doi:10.1103/physrevb.104.115404.

[56] Eslam Khalaf, Shubhayu Chatterjee, Nick Bultinck, Michael P. Zaletel, and Ashvin Vishwanath. Charged skyrmions and topological origin of superconductivity in magic-angle graphene. *Science Advances*, 7(19), May 2021. doi:10.1126/sciadv.abf5299.

[57] Yves H. Kwan, Glenn Wagner, Nick Bultinck, Steven H. Simon, and S. A. Parameswaran. Skyrmions in twisted bilayer graphene: stability, pairing, and crystallization, 2021. URL: https://arxiv.org/abs/2112.06936, doi:10.48550/ARXIV.2112.06936.

[58] Y. H. Kwan, G. Wagner, T. Soejima, M. P. Zaletel, S. H. Simon, S. A. Parameswaran, and N. Bultinck. Kekulé spiral order at all nonzero integer fillings in twisted bilayer graphene. *Physical Review X*, 11(4), December 2021. doi:10.1103/physrevx.11.041063.

[59] Glenn Wagner, Yves H. Kwan, Nick Bultinck, Steven H. Simon, and S. A. Parameswaran. Global phase diagram of the normal state of twisted bilayer graphene. *Physical Review Letters*, 128(15), April 2022. doi:10.1103/physrevlett.128.156401.

[60] Yugui Yao, Fei Ye, Xiao-Liang Qi, Shou-Cheng Zhang, and Zhong Fang. Spin-orbit gap of graphene: First-principles calculations. *Physical Review B*, 75(4), January 2007. doi:10.1103/physrevb.75.041401.

[61] E. Mostaani, N. D. Drummond, and V. I. Fal'ko. Quantum Monte Carlo calculation of the binding energy of bilayer graphene. *Physical Review Letters*, 115(11), September 2015. doi:10.1103/physrevlett.115.115501.

[62] Edward McCann and Vladimir I. Fal'ko. Landau-level degeneracy and quantum Hall effect in a graphite bilayer. *Physical Review Letters*, 96(8), March 2006. doi:10.1103/physrevlett.96.086805.

[63] Isaac Amidror. *The Theory of the Moiré Phenomenon: Volume I: Periodic Layers*, volume 38. Springer Science & Business Media, 2009.

[64] E. J. Mele. Commensuration and interlayer coherence in twisted bilayer graphene. *Physical Review B*, 81(16), April 2010. doi:10.1103/physrevb.81.161405.

[65] Jian Kang and Oskar Vafek. Symmetry, maximally localized Wannier states, and a low-energy model for twisted bilayer graphene narrow bands. *Physical Review X*, 8(3), September 2018. doi:10.1103/physrevx.8.031088.

[66] Pilkyung Moon and Mikito Koshino. Energy spectrum and quantum Hall effect in twisted bilayer graphene. *Physical Review B*, 85(19), May 2012. doi:10.1103/physrevb.85.195458.

[67] Mark Goerbig and Gilles Montambaux. Dirac Fermions in condensed matter and beyond. In *Dirac Matter*, pages 25–53. Springer, 2017.

[68] Hoi Chun Po, Liujun Zou, Ashvin Vishwanath, and T. Senthil. Origin of Mott insulating behavior and superconductivity in twisted bilayer graphene. *Physical Review X*, 8(3), September 2018. doi:10.1103/physrevx.8.031089.

[69] R. de Gail, M. O. Goerbig, F. Guinea, G. Montambaux, and A. H. Castro Neto. Topologically protected zero modes in twisted bilayer graphene. *Physical Review B*, 84(4), July 2011. doi:10.1103/physrevb.84.045436.

[70] Nguyen N. T. Nam and Mikito Koshino. Lattice relaxation and energy band modulation in twisted bilayer graphene. *Physical Review B*, 96(7), August 2017. doi:10.1103/physrevb.96.075311.

[71] Stephen Carr, Shiang Fang, Ziyan Zhu, and Efthimios Kaxiras. Exact continuum model for low-energy electronic states of twisted bilayer graphene. *Physical Review Research*, 1(1), August 2019. doi:10.1103/physrevresearch.1.013001.

[72] Mikito Koshino, Noah F. Q. Yuan, Takashi Koretsune, Masayuki Ochi, Kazuhiko Kuroki, and Liang Fu. Maximally localized Wannier orbitals and the extended Hubbard model for twisted bilayer graphene. *Physical Review X*, 8(3), September 2018. doi:10.1103/physrevx.8.031087.

[73] Patrick J. Ledwith, Eslam Khalaf, Ziyan Zhu, Stephen Carr, Efthimios Kaxiras, and Ashvin Vishwanath. TB or not TB? contrasting properties of twisted bilayer graphene and the alternating twist n-layer structures ($n = 3, 4, 5, \dots$), 2021. URL: https://arxiv.org/abs/2111.11060, doi:10.48550/ARXIV.2111.11060.

[74] Oskar Vafek and Jian Kang. Renormalization group study of hidden symmetry in twisted bilayer graphene with Coulomb interactions. *Physical Review Letters*, 125(25), December 2020. doi:10.1103/physrevlett.125.257602.

[75] Grigory Tarnopolsky, Alex Jura Kruchkov, and Ashvin Vishwanath. Origin of magic angles in twisted bilayer graphene. *Physical Review Letters*, 122(10), March 2019. doi:10.1103/physrevlett.122.106405.

[76] Patrick J. Ledwith, Grigory Tarnopolsky, Eslam Khalaf, and Ashvin Vishwanath. Fractional Chern insulator states in twisted bilayer graphene: An analytical approach. *Physical Review Research*, 2(2), May 2020. doi:10.1103/physrevresearch.2.023237.

[77] Shang Liu, Eslam Khalaf, Jong Yeon Lee, and Ashvin Vishwanath. Nematic topological semimetal and insulator in magic-angle bilayer graphene at charge neutrality. *Physical Review Research*, 3(1), January 2021. doi:10.1103/physrevresearch.3.013033.

[78] Nick Bultinck, Eslam Khalaf, Shang Liu, Shubhayu Chatterjee, Ashvin Vishwanath, and Michael P. Zaletel. Ground state and hidden symmetry of magic-angle graphene at even integer filling. *Physical Review X*, 10(3), August 2020. doi:10.1103/physrevx.10.031034.

[79] Nick Bultinck, Shubhayu Chatterjee, and Michael P. Zaletel. Mechanism for anomalous Hall ferromagnetism in twisted bilayer graphene. *Physical Review Letters*, 124(16), April 2020. doi:10.1103/physrevlett.124.166601.

[80] Shubhayu Chatterjee, Nick Bultinck, and Michael P. Zaletel. Symmetry breaking and skyrmionic transport in twisted bilayer graphene. *Physical Review B*, 101(16), April 2020. doi:10.1103/physrevb.101.165141.

[81] Tommaso Cea and Francisco Guinea. Band structure and insulating states driven by Coulomb interaction in twisted bilayer graphene. *Physical Review B*, 102(4), July 2020. doi:10.1103/physrevb.102.045107.

[82] B. Andrei Bernevig, Zhi-Da Song, Nicolas Regnault, and Biao Lian. Twisted bilayer graphene. III. Interacting Hamiltonian and exact symmetries. *Physical Review B*, 103(20), May 2021. doi:10.1103/physrevb.103.205413.

[83] Biao Lian, Zhi-Da Song, Nicolas Regnault, Dmitri K. Efetov, Ali Yazdani, and B. Andrei Bernevig. Twisted bilayer graphene. IV. Exact insulator ground states and phase diagram. *Physical Review B*, 103(20), May 2021. doi:10.1103/physrevb.103.205414.

[84] Kasra Hejazi, Xiao Chen, and Leon Balents. Hybrid Wannier Chern bands in magic angle twisted bilayer graphene and the quantized anomalous Hall effect. *Physical Review Research*, 3(1), March 2021. doi:10.1103/physrevresearch.3.013242.

[85] Ming Xie and A. H. MacDonald. Nature of the correlated insulator states in twisted bilayer graphene. *Physical Review Letters*, 124(9), March 2020. doi:10.1103/physrevlett.124.097601.

[86] Yi Zhang, Kun Jiang, Ziqiang Wang, and Fuchun Zhang. Correlated insulating phases of twisted bilayer graphene at commensurate filling fractions: A Hartree-Fock study. *Physical Review B*, 102(3), July 2020. doi:10.1103/physrevb.102.035136.

[87] Jian Kang, B. Andrei Bernevig, and Oskar Vafek. Cascades between light and heavy fermions in the normal state of magic-angle twisted bilayer graphene. *Physical Review Letters*, 127(26), December 2021. doi:10.1103/physrevlett.127.266402.

[88] Francisco Guinea and Niels R. Walet. Electrostatic effects, band distortions, and superconductivity in twisted graphene bilayers. *Proceedings of the National Academy of Sciences*, 115(52):13174–13179, December 2018. doi:10.1073/pnas.1810947115.

[89] Tommaso Cea, Niels R. Walet, and Francisco Guinea. Electronic band structure and pinning of Fermi energy to van Hove singularities in twisted bilayer graphene: A self-consistent approach. *Physical Review B*, 100(20), November 2019. doi:10.1103/physrevb.100.205113.

[90] Zachary A H Goodwin, Valerio Vitale, Xia Liang, Arash A Mostofi, and Johannes Lischner. Hartree theory calculations of quasiparticle properties in twisted bilayer graphene. *Electronic Structure*, 2(3):034001, August 2020. doi:10.1088/2516-1075/ab9f94.

[91] Eric Cancès and Claude Le Bris. On the convergence of SCF algorithms for the Hartree-Fock equations. *ESAIM: Mathematical Modelling and Numerical Analysis*, 34(4):749–774, July 2000. doi:10.1051/m2an:2000102.

[92] Jian Kang and Oskar Vafek. Strong coupling phases of partially filled twisted bilayer graphene narrow bands. *Physical Review Letters*, 122(24), June 2019. doi:10.1103/physrevlett.122.246401.

[93] Jianpeng Liu, Junwei Liu, and Xi Dai. Pseudo Landau level representation of twisted bilayer graphene: Band topology and implications on the correlated insulating phase. *Physical Review B*, 99(15), April 2019. doi:10.1103/physrevb.99.155415.

[94] B. Andrei Bernevig, Biao Lian, Aditya Cowsik, Fang Xie, Nicolas Regnault, and Zhi-Da Song. Twisted bilayer graphene. v. Exact analytic many-body excitations in Coulomb Hamiltonians: Charge gap, Goldstone modes, and absence of Cooper pairing. *Physical Review B*, 103(20), May 2021. doi:10.1103/physrevb.103.205415.

[95] Fang Xie, Aditya Cowsik, Zhi-Da Song, Biao Lian, B. Andrei Bernevig, and Nicolas Regnault. Twisted bilayer graphene. VI. An exact diagonalization study at nonzero integer filling. *Physical Review B*, 103(20), May 2021. doi:10.1103/physrevb.103.205416.

[96] Pawel Potasz, Ming Xie, and A. H. MacDonald. Exact diagonalization for magic-angle twisted bilayer graphene. *Physical Review Letters*, 127(14), September 2021. doi:10.1103/physrevlett.127.147203.

[97] Daniel E. Parker, Tomohiro Soejima, Johannes Hauschild, Michael P. Zaletel, and Nick Bultinck. Strain-induced quantum phase transitions in magic-angle graphene. *Physical Review Letters*, 127(2), July 2021. doi:10.1103/physrevlett.127.027601.

[98] Xu Zhang, Gaopei Pan, Yi Zhang, Jian Kang, and Zi Yang Meng. Momentum space quantum Monte Carlo on twisted bilayer graphene. *Chinese Physics Letters*, 38(7):077305, July 2021. doi:10.1088/0256-307x/38/7/077305.

[99] Johannes S. Hofmann, Eslam Khalaf, Ashvin Vishwanath, Erez Berg, and Jong Yeon Lee. Fermionic Monte Carlo study of a realistic model of twisted bilayer graphene. *Physical Review X*, 12(1), March 2022. doi:10.1103/physrevx.12.011061.

[100] Ajit Srivastava and Ataç Imamoğlu. Signatures of Bloch-band geometry on excitons: Nonhydrogenic spectra in transition-metal dichalcogenides. *Physical Review Letters*, 115(16), October 2015. doi:10.1103/physrevlett.115.166802.

[101] Jianhui Zhou, Wen-Yu Shan, Wang Yao, and Di Xiao. Berry phase modification to the energy spectrum of excitons. *Physical Review Letters*, 115(16), October 2015. doi:10.1103/physrevlett.115.166803.

[102] Wang Yao and Qian Niu. Berry phase effect on the exciton transport and on the exciton Bose-Einstein condensate. *Physical Review Letters*, 101(10), September 2008. doi:10.1103/physrevlett.101.106401.

[103] Gang Wang, Alexey Chernikov, Mikhail M. Glazov, Tony F. Heinz, Xavier Marie, Thierry Amand, and Bernhard Urbaszek. Colloquium : Excitons in atomically thin transition metal dichalcogenides. *Reviews of Modern Physics*, 90(2), April 2018. doi:10.1103/revmodphys.90.021001.

[104] Masaru Onga, Yijin Zhang, Toshiya Ideue, and Yoshihiro Iwasa. Exciton Hall effect in monolayer MoS2. *Nature Materials*, 16(12):1193–1197, October 2017. doi:10.1038/nmat4996.

[105] Ya-Hui Zhang, Dan Mao, and T. Senthil. Twisted bilayer graphene aligned with hexagonal boron nitride: Anomalous Hall effect and a lattice model. *Physical Review Research*, 1(3), November 2019. doi:10.1103/physrevresearch.1.033126.

[106] H. Polshyn, J. Zhu, M. A. Kumar, Y. Zhang, F. Yang, C. L. Tschirhart, M. Serlin, K. Watanabe, T. Taniguchi, A. H. MacDonald, and A. F. Young. Electrical switching of magnetic order in an orbital Chern insulator. *Nature*, 588(7836):66–70, November 2020. doi:10.1038/s41586-020-2963-8.

[107] Jihang Zhu, Jung-Jung Su, and A. H. MacDonald. Voltage-controlled magnetic reversal in orbital Chern insulators. *Physical Review Letters*, 125(22), November 2020. doi:10.1103/physrevlett.125.227702.

[108] Chunli Huang, Nemin Wei, and Allan H. MacDonald. Current-driven magnetization reversal in orbital Chern insulators. *Physical Review Letters*, 126(5), February 2021. doi:10.1103/physrevlett.126.056801.

[109] Cui-Zu Chang, Jinsong Zhang, Xiao Feng, Jie Shen, Zuocheng Zhang, Minghua Guo, Kang Li, Yunbo Ou, Pang Wei, Li-Li Wang, Zhong-Qing Ji, Yang Feng, Shuaihua Ji, Xi Chen, Jinfeng Jia, Xi Dai, Zhong Fang, Shou-Cheng Zhang, Ke He, Yayu Wang, Li Lu, Xu-Cun Ma, and Qi-Kun Xue. Experimental observation of the quantum anomalous Hall effect in a magnetic topological insulator. *Science*, 340(6129):167–170, April 2013. doi:10.1126/science.1234414.

[110] A. Karlhede, K. Lejnell, and S. L. Sondhi. Dynamics of the compact, ferromagnetic $\nu = 1$ edge. *Physical Review B*, 60(23):15948–15956, December 1999. doi:10.1103/physrevb.60.15948.

[111] D. Pines. *Theory Of Quantum Liquids: Normal Fermi Liquids*. Advanced Books Classics. Avalon Publishing, 1994. URL: https://books.google.com.hk/books?id=5fN3zgEACAAJ.

[112] Yu A Bychkov, SV Iordanskiĭ, and GM Eliashberg. Two-dimensional electrons in a strong magnetic field. *Soviet Journal of Experimental and Theoretical Physics Letters*, 33:143, 1981.

[113] C. Kallin and B. I. Halperin. Excitations from a filled Landau level in the two-dimensional electron gas. *Physical Review B*, 30(10):5655–5668, November 1984. doi:10.1103/physrevb.30.5655.

[114] Haruki Watanabe and Hitoshi Murayama. Unified description of Nambu-Goldstone bosons without Lorentz invariance. *Physical Review Letters*, 108(25), June 2012. doi:10.1103/physrevlett.108.251602.

[115] Haruki Watanabe. Counting rules of Nambu–Goldstone modes. *Annual Review of Condensed Matter Physics*, 11(1):169–187, March 2020. doi:10.1146/annurev-conmatphys-031119-050644.

[116] Yahya Alavirad and Jay Sau. Ferromagnetism and its stability from the one-magnon spectrum in twisted bilayer graphene. *Physical Review B*, 102(23), December 2020. doi:10.1103/physrevb.102.235123.

[117] F. D. M. Haldane. Fractional quantization of the Hall effect: A hierarchy of incompressible quantum fluid states. *Physical Review Letters*, 51(7):605–608, August 1983. doi:10.1103/physrevlett.51.605.

[118] LP Gor'kov and IE Dzyaloshinskii. Contribution to the theory of the Mott exciton in a strong magnetic field. *Sov. Phys. JETP*, 26:449–451, 1968.

[119] Raffaele Resta. Manifestations of Berry's phase in molecules and condensed matter. *Journal of Physics: Condensed Matter*, 12(9):R107–R143, February 2000. doi:10.1088/0953-8984/12/9/201.

[120] Takahiro Fukui, Yasuhiro Hatsugai, and Hiroshi Suzuki. Chern numbers in discretized brillouin zone: Efficient method of computing (spin) Hall conductances. *Journal of the Physical Society of Japan*, 74(6):1674–1677, June 2005. doi:10.1143/jpsj.74.1674.

[121] Peter Ring and Peter Schuck. *The nuclear many-body problem*. Springer Science & Business Media, 2004.

[122] Fengcheng Wu and Sankar Das Sarma. Collective excitations of quantum anomalous Hall ferromagnets in twisted bilayer graphene. *Physical Review Letters*, 124(4), January 2020. doi:10.1103/physrevlett.124.046403.

[123] Ryuichi Shindou, Ryo Matsumoto, Shuichi Murakami, and Jun ichiro Ohe. Topological chiral magnonic edge mode in a magnonic crystal. *Physical Review B*, 87(17), May 2013. doi:10.1103/physrevb.87.174427.

[124] Torsten Karzig, Charles-Edouard Bardyn, Netanel H. Lindner, and Gil Refael. Topological polaritons. *Physical Review X*, 5(3), July 2015. doi:10.1103/physrevx.5.031001.

[125] A. V. Nalitov, D. D. Solnyshkov, and G. Malpuech. Polariton $\mathbb{Z}$ topological insulator. *Physical Review Letters*, 114(11), March 2015. doi:10.1103/physrevlett.114.116401.

[126] Fengcheng Wu, Timothy Lovorn, and A. H. MacDonald. Topological exciton bands in moiré heterojunctions. *Physical Review Letters*, 118(14), April 2017. doi:10.1103/physrevlett.118.147401.

[127] Z. R. Gong, W. Z. Luo, Z. F. Jiang, and H. C. Fu. Chiral topological excitons in the monolayer transition metal dichalcogenides. *Scientific Reports*, 7(1), February 2017. doi:10.1038/srep42390.

[128] Ke Chen and Ryuichi Shindou. Chiral topological excitons in a Chern band insulator. *Physical Review B*, 96(16), October 2017. doi:10.1103/physrevb.96.161101.

[129] Igor V. Kukushkin, Jurgen H. Smet, Vito W. Scarola, Vladimir Umansky, and Klaus von Klitzing. Dispersion of the excitations of fractional quantum Hall states. *Science*, 324(5930):1044–1047, May 2009. doi:10.1126/science.1171472.

[130] Nikolaos Stefanidis and Inti Sodemann. Excitonic laughlin states in ideal topological insulator flat bands and their possible presence in moiré superlattice materials. *Physical Review B*, 102(3), July 2020. doi:10.1103/physrevb.102.035158.

[131] K. Moon, H. Mori, Kun Yang, S. M. Girvin, A. H. MacDonald, L. Zheng, D. Yoshioka, and Shou-Cheng Zhang. Spontaneous interlayer coherence in double-layer quantum Hall systems: Charged vortices and Kosterlitz-Thouless phase transitions. *Physical Review B*, 51(8):5138–5170, February 1995. doi:10.1103/physrevb.51.5138.

[132] Kun Yang. Dipolar excitons, spontaneous phase coherence, and superfluid-insulator transition in bilayer quantum Hall systems at $\nu > 1$. *Physical Review Letters*, 87(5), July 2001. doi:10.1103/physrevlett.87.056802.

[133] Ya-Hui Zhang. Composite fermion insulator in opposite-fields quantum Hall bilayers, 2018. URL: https://arxiv.org/abs/1810.03600, doi:10.48550/ARXIV.1810.03600.

[134] Max A. Metlitski, David F. Mross, Subir Sachdev, and T. Senthil. Cooper pairing in non-Fermi liquids. *Physical Review B*, 91(11), March 2015. doi:10.1103/physrevb.91.115111.

[135] Yong Baek Kim, Chetan Nayak, Eugene Demler, N. Read, and S. Das Sarma. Bilayer paired quantum Hall states and Coulomb drag. *Physical Review B*, 63(20), April 2001. doi:10.1103/physrevb.63.205315.

[136] X. G. Wen and A. Zee. Shift and spin vector: New topological quantum numbers for the Hall fluids. *Physical Review Letters*, 69(6):953–956, August 1992. doi:10.1103/physrevlett.69.953.

[137] Jason Alicea, Olexei I. Motrunich, G. Refael, and Matthew P. A. Fisher. Interlayer coherent composite Fermi liquid phase in quantum Hall bilayers. *Physical Review Letters*, 103(25), December 2009. doi:10.1103/physrevlett.103.256403.

[138] Boris Spivak and Steven A. Kivelson. Phases intermediate between a two-dimensional electron liquid and Wigner crystal. *Physical Review B*, 70(15), October 2004. doi:10.1103/physrevb.70.155114.

[139] Michael M. Fogler. Stripe and bubble phases in quantum Hall systems. In *High Magnetic Fields*, pages 98–138. Springer Berlin Heidelberg, 2002. doi:10.1007/3-540-45649-x_4.

[140] N. R. Cooper, E. H. Rezayi, and S. H. Simon. Vortex lattices in rotating atomic Bose gases with dipolar interactions. *Physical Review Letters*, 95(20), November 2005. doi:10.1103/physrevlett.95.200402.

[141] N.R. Cooper. Rapidly rotating atomic gases. *Advances in Physics*, 57(6):539–616, November 2008. doi:10.1080/00018730802564122.

[142] C. L. Kane and Matthew P. A. Fisher. Quantized thermal transport in the fractional quantum Hall effect. *Physical Review B*, 55(23):15832–15837, June 1997. doi:10.1103/physrevb.55.15832.

[143] Guorui Chen, Aaron L. Sharpe, Eli J. Fox, Ya-Hui Zhang, Shaoxin Wang, Lili Jiang, Bosai Lyu, Hongyuan Li, Kenji Watanabe, Takashi Taniguchi, Zhiwen Shi, T. Senthil, David Goldhaber-Gordon, Yuanbo Zhang, and Feng Wang. Tunable correlated Chern insulator and ferromagnetism in a moiré superlattice. *Nature*, 579(7797):56–61, March 2020. doi:10.1038/s41586-020-2049-7.

[144] Tingxin Li, Shengwei Jiang, Bowen Shen, Yang Zhang, Lizhong Li, Zui Tao, Trithep Devakul, Kenji Watanabe, Takashi Taniguchi, Liang Fu, Jie Shan, and Kin Fai Mak. Quantum anomalous Hall effect from intertwined moiré bands. *Nature*, 600(7890):641–646, December 2021. doi:10.1038/s41586-021-04171-1.

[145] Cheng Shen, Yanbang Chu, QuanSheng Wu, Na Li, Shuopei Wang, Yanchong Zhao, Jian Tang, Jieying Liu, Jinpeng Tian, Kenji Watanabe, Takashi Taniguchi, Rong Yang, Zi Yang Meng, Dongxia Shi, Oleg V. Yazyev, and Guangyu Zhang. Correlated states in twisted double bilayer graphene. *Nature Physics*, 16(5):520–525, March 2020. doi:10.1038/s41567-020-0825-9.

[146] Xiaomeng Liu, Zeyu Hao, Eslam Khalaf, Jong Yeon Lee, Yuval Ronen, Hyobin Yoo, Danial Haei Najafabadi, Kenji Watanabe, Takashi Taniguchi, Ashvin Vishwanath, and Philip Kim. Tunable spin-polarized correlated states in twisted double bilayer graphene. *Nature*, 583(7815):221–225, July 2020. doi:10.1038/s41586-020-2458-7.

[147] Yuan Cao, Daniel Rodan-Legrain, Oriol Rubies-Bigorda, Jeong Min Park, Kenji Watanabe, Takashi Taniguchi, and Pablo Jarillo-Herrero. Tunable correlated states and spin-polarized phases in twisted bilayer–bilayer graphene. *Nature*, 583(7815):215–220, May 2020. doi:10.1038/s41586-020-2260-6.

[148] Minhao He, Jiaqi Cai, Ya-Hui Zhang, Yang Liu, Yuhao Li, Takashi Taniguchi, Kenji Watanabe, David H. Cobden, Matthew Yankowitz, and Xiaodong Xu. Chirality-dependent topological states in twisted double bilayer graphene, 2021. URL: https://arxiv.org/abs/2109.08255, doi:10.48550/ARXIV.2109.08255.

[149] H. Polshyn, Y. Zhang, M. A. Kumar, T. Soejima, P. Ledwith, K. Watanabe, T. Taniguchi, A. Vishwanath, M. P. Zaletel, and A. F. Young. Topological charge density waves at half-integer filling of a moiré superlattice. *Nature Physics*, 18(1):42–47, December 2021. doi:10.1038/s41567-021-01418-6.

[150] Xianqing Lin and Jun Ni. Symmetry breaking in the double moiré superlattices of relaxed twisted bilayer graphene on hexagonal boron nitride. *Physical Review B*, 102(3), July 2020. doi:10.1103/physrevb.102.035441.

[151] Tommaso Cea, Pierre A. Pantaleón, and Francisco Guinea. Band structure of twisted bilayer graphene on hexagonal boron nitride. *Physical Review B*, 102(15), October 2020. doi:10.1103/physrevb.102.155136.

[152] Jingtian Shi, Jihang Zhu, and A. H. MacDonald. Moiré commensurability and the quantum anomalous Hall effect in twisted bilayer graphene on hexagonal boron nitride. *Physical Review B*, 103(7), February 2021. doi:10.1103/physrevb.103.075122.

[153] Vladimir I. Fal'ko and S. V. Iordanskii. Topological defects and Goldstone excitations in domain walls between ferromagnetic quantum Hall liquids. *Physical Review Letters*, 82(2):402–405, January 1999. doi:10.1103/physrevlett.82.402.

[154] Aditi Mitra and S. M. Girvin. Electron/nuclear spin domain walls in quantum Hall systems. *Physical Review B*, 67(24), June 2003. doi:10.1103/physrevb.67.245311.

[155] D. A. Abanin, S. A. Parameswaran, S. A. Kivelson, and S. L. Sondhi. Nematic valley ordering in quantum Hall systems. *Physical Review B*, 82(3), July 2010. doi:10.1103/physrevb.82.035428.

[156] Akshay Kumar, S. A. Parameswaran, and S. L. Sondhi. Microscopic theory of a quantum Hall ising nematic: Domain walls and disorder. *Physical Review B*, 88(4), July 2013. doi:10.1103/physrevb.88.045133.

[157] Kartiek Agarwal, Mallika T. Randeria, A. Yazdani, S. L. Sondhi, and S. A. Parameswaran. Topology- and symmetry-protected domain wall conduction in quantum Hall nematics. *Physical Review B*, 100(16), October 2019. doi:10.1103/physrevb.100.165103.

[158] Jeroen Danon, Ajit C. Balram, Samuel Sánchez, and Mark S. Rudner. Charge and spin textures of Ising quantum Hall ferromagnet domain walls. *Physical Review B*, 100(23), December 2019. doi:10.1103/physrevb.100.235406.

[159] Mallika T. Randeria, Kartiek Agarwal, Benjamin E. Feldman, Hao Ding, Huiwen Ji, R. J. Cava, S. L. Sondhi, Siddharth A. Parameswaran, and Ali Yazdani. Interacting multi-channel topological boundary modes in a quantum Hall valley system. *Nature*, 566(7744):363–367, February 2019. doi:10.1038/s41586-019-0913-0.

[160] Eslam Khalaf, Nick Bultinck, Ashvin Vishwanath, and Michael P. Zaletel. Soft modes in magic angle twisted bilayer graphene, 2020. URL: https://arxiv.org/abs/2009.14827, doi:10.48550/ARXIV.2009.14827.

[161] Gal Shavit and Yuval Oreg. Domain formation driven by the entropy of topological edge modes. *Physical Review Letters*, 128(15), April 2022. doi:10.1103/physrevlett.128.156801.

[162] Xiao-Liang Qi. Generic wave-function description of fractional quantum anomalous Hall states and fractional topological insulators. *Physical Review Letters*, 107(12), September 2011. doi:10.1103/physrevlett.107.126803.

[163] Thomas Scaffidi and Gunnar Möller. Adiabatic continuation of fractional Chern insulators to fractional quantum Hall states. *Physical Review Letters*, 109(24), December 2012. doi:10.1103/physrevlett.109.246805.

[164] Yang-Le Wu, N. Regnault, and B. Andrei Bernevig. Gauge-fixed Wannier wave functions for fractional topological insulators. *Physical Review B*, 86(8), August 2012. doi:10.1103/physrevb.86.085129.

[165] Maissam Barkeshli and Xiao-Liang Qi. Topological nematic states and non-Abelian lattice dislocations. *Physical Review X*, 2(3), August 2012. doi:10.1103/physrevx.2.031013.

[166] Xiao Li, Fan Zhang, Qian Niu, and A. H. MacDonald. Spontaneous layer-pseudospin domain walls in bilayer graphene. *Physical Review Letters*, 113(11), September 2014. doi:10.1103/physrevlett.113.116803.

[167] Wen-Yu He, David Goldhaber-Gordon, and K. T. Law. Giant orbital magnetoelectric effect and current-induced magnetization switching in twisted bilayer graphene. *Nature Communications*, 11(1), April 2020. doi:10.1038/s41467-020-15473-9.

[168] J T Chalker and P D Coddington. Percolation, quantum tunnelling and the integer Hall effect. *Journal of Physics C: Solid State Physics*, 21(14):2665–2679, May 1988. doi:10.1088/0022-3719/21/14/008.

[169] C. L. Tschirhart, M. Serlin, H. Polshyn, A. Shragai, Z. Xia, J. Zhu, Y. Zhang, K. Watanabe, T. Taniguchi, M. E. Huber, and A. F. Young. Imaging orbital ferromagnetism in a moiré Chern insulator. *Science*, 372(6548):1323–1327, June 2021. doi:10.1126/science.abd3190.

[170] Sameer Grover, Matan Bocarsly, Aviram Uri, Petr Stepanov, Giorgio Di Battista, Indranil Roy, Jiewen Xiao, Alexander Y. Meltzer, Yuri Myasoedov, Keshav Pareek, Kenji Watanabe, Takashi Taniguchi, Binghai Yan, Ady Stern, Erez Berg, Dmitri K. Efetov, and Eli Zeldov. Imaging Chern mosaic and Berry-curvature magnetism in magic-angle graphene, 2022. URL: https://arxiv.org/abs/2201.06901, doi:10.48550/ARXIV.2201.06901.

[171] AA Belavin and AM Polyakov. Metastable states of two-dimensional isotropic ferromagnets. *JETP lett*, 22(10):245–248, 1975.

[172] S. L. Sondhi, A. Karlhede, S. A. Kivelson, and E. H. Rezayi. Skyrmions and the crossover from the integer to fractional quantum Hall effect at small Zeeman energies. *Physical Review B*, 47(24):16419–16426, June 1993. doi:10.1103/physrevb.47.16419.

[173] H. A. Fertig, L. Brey, R. Côté, and A. H. MacDonald. Charged spin-texture excitations and the Hartree-Fock approximation in the quantum Hall effect. *Physical Review B*, 50(15):11018–11021, October 1994. doi:10.1103/physrevb.50.11018.

[174] M. Abolfath, J. J. Palacios, H. A. Fertig, S. M. Girvin, and A. H. MacDonald. Critical comparison of classical field theory and microscopic wave functions for skyrmions in quantum Hall ferromagnets. *Physical Review B*, 56(11):6795–6804, September 1997. doi:10.1103/physrevb.56.6795.

[175] Ya-Hui Zhang, Dan Mao, Yuan Cao, Pablo Jarillo-Herrero, and T. Senthil. Nearly flat Chern bands in moiré superlattices. *Physical Review B*, 99(7), February 2019. doi:10.1103/physrevb.99.075127.

[176] Fengcheng Wu and S. Das Sarma. Quantum geometry and stability of moiré flatband ferromagnetism. *Physical Review B*, 102(16), October 2020. doi:10.1103/physrevb.102.165118.

[177] A. G. Abanov and P. B. Wiegmann. Chiral nonlinear σ models as models for topological superconductivity. *Physical Review Letters*, 86(7):1319–1322, February 2001. doi:10.1103/physrevlett.86.1319.

[178] Tarun Grover and T. Senthil. Topological spin Hall states, charged skyrmions, and superconductivity in two dimensions. *Physical Review Letters*, 100(15), April 2008. doi:10.1103/physrevlett.100.156804.

[179] Shubhayu Chatterjee, Matteo Ippoliti, and Michael P. Zaletel. Skyrmion superconductivity: Dmrg evidence for a topological route to superconductivity, 2020. URL: https://arxiv.org/abs/2010.01144, doi:10.48550/ARXIV.2010.01144.

[180] Eslam Khalaf and Ashvin Vishwanath. From electrons to baby skyrmions in Chern ferromagnets: A topological mechanism for spin-polaron formation in twisted bilayer graphene, 2021. URL: https://arxiv.org/abs/2112.06935, doi:10.48550/ARXIV.2112.06935.

[181] Frank Schindler, Oskar Vafek, and B. Andrei Bernevig. Trions in twisted bilayer graphene. *Physical Review B*, 105(15), April 2022. doi:10.1103/physrevb.105.155135.

[182] Yuhang Jiang, Xinyuan Lai, Kenji Watanabe, Takashi Taniguchi, Kristjan Haule, Jinhai Mao, and Eva Y. Andrei. Charge order and broken rotational symmetry in magic-angle twisted bilayer graphene. *Nature*, 573(7772):91–95, July 2019. doi:10.1038/s41586-019-1460-4.

[183] K. Lejnell, A. Karlhede, and S. L. Sondhi. Effective-action studies of quantum Hall spin textures. *Physical Review B*, 59(15):10183–10193, April 1999. doi:10.1103/physrevb.59.10183.

[184] David R. Nelson and J. M. Kosterlitz. Universal jump in the superfluid density of two-dimensional superfluids. *Physical Review Letters*, 39(19):1201–1205, November 1977. doi:10.1103/physrevlett.39.1201.

[185] Thomas Bömerich, Lukas Heinen, and Achim Rosch. Skyrmion and tetarton lattices in twisted bilayer graphene. *Physical Review B*, 102(10), September 2020. doi:10.1103/physrevb.102.100408.

[186] Ming Xie and A. H. MacDonald. Weak-field Hall resistivity and spin-valley flavor symmetry breaking in magic-angle twisted bilayer graphene. *Physical Review Letters*, 127(19), November 2021. doi:10.1103/physrevlett.127.196401.

[187] Jian Kang and Oskar Vafek. Non-Abelian Dirac node braiding and near-degeneracy of correlated phases at odd integer filling in magic-angle twisted bilayer graphene. *Physical Review B*, 102(3), July 2020. doi:10.1103/physrevb.102.035161.

[188] Tomohiro Soejima, Daniel E. Parker, Nick Bultinck, Johannes Hauschild, and Michael P. Zaletel. Efficient simulation of moiré materials using the density matrix renormalization group. *Physical Review B*, 102(20), November 2020. doi:10.1103/physrevb.102.205111.

[189] Jianpeng Liu and Xi Dai. Theories for the correlated insulating states and quantum anomalous Hall effect phenomena in twisted bilayer graphene. *Physical Review B*, 103(3), January 2021. doi:10.1103/physrevb.103.035427.

[190] Gal Shavit, Erez Berg, Ady Stern, and Yuval Oreg. Theory of correlated insulators and superconductivity in twisted bilayer graphene. *Physical Review Letters*, 127(24), December 2021. doi:10.1103/physrevlett.127.247703.

[191] Shihao Zhang, Xin Lu, and Jianpeng Liu. Correlated insulators, density wave states, and their nonlinear optical response in magic-angle twisted bilayer graphene, 2021. URL: https://arxiv.org/abs/2109.11441, doi:10.48550/ARXIV.2109.11441.

[192] Louk Rademaker, Dmitry A. Abanin, and Paula Mellado. Charge smoothening and band flattening due to Hartree corrections in twisted bilayer graphene. *Physical Review B*, 100(20), November 2019. doi:10.1103/physrevb.100.205114.

[193] Yunlong Lian and Mark O. Goerbig. Spin-valley skyrmions in graphene at filling factor $\nu = -1$. *Physical Review B*, 95(24), June 2017. doi:10.1103/physrevb.95.245428.

[194] Jonathan Atteia, Yunlong Lian, and Mark Oliver Goerbig. Skyrmion zoo in graphene at charge neutrality in a strong magnetic field. *Physical Review B*, 103(3), January 2021. doi:10.1103/physrevb.103.035403.

[195] S. E. Barrett, G. Dabbagh, L. N. Pfeiffer, K. W. West, and R. Tycko. Optically pumped NMR evidence for finite-size skyrmions in GaAs quantum wells near Landau level filling $\nu = 1$. *Physical Review Letters*, 74(25):5112–5115, June 1995. doi:10.1103/physrevlett.74.5112.

[196] Dumitru Călugăru, Nicolas Regnault, Myungchul Oh, Kevin P. Nuckolls, Dillon Wong, Ryan L. Lee, Ali Yazdani, Oskar Vafek, and B. Andrei Bernevig. Spectroscopy of twisted bilayer graphene correlated insulators, 2021. URL: https://arxiv.org/abs/2110.15300, doi:10.48550/ARXIV.2110.15300.

[197] Jung Pyo Hong, Tomohiro Soejima, and Michael P. Zaletel. Detecting symmetry breaking in magic angle graphene using scanning tunneling microscopy, 2021. URL: https://arxiv.org/abs/2110.14674, doi:10.48550/ARXIV.2110.14674.

[198] Si-Yu Li, Yu Zhang, Long-Jing Yin, and Lin He. Scanning tunneling microscope study of quantum Hall isospin ferromagnetic states in the zero Landau level in a graphene monolayer. *Physical Review B*, 100(8), August 2019. doi:10.1103/physrevb.100.085437.

[199] Xiaomeng Liu, Gelareh Farahi, Cheng-Li Chiu, Zlatko Papic, Kenji Watanabe, Takashi Taniguchi, Michael P. Zaletel, and Ali Yazdani. Visualizing broken symmetry and topological defects in a quantum Hall ferromagnet. *Science*, 375(6578):321–326, January 2022. doi:10.1126/science.abm3770.

[200] A. Coissard, D. Wander, H. Vignaud, A. G. Grushin, C. Repellin, K. Watanabe, T. Taniguchi, F. Gay, C. Winkelmann, H. Courtois, H. Sellier, and B. Sacépé. Imaging tunable quantum Hall broken-symmetry orders in charge-neutral graphene, 2021. URL: https://arxiv.org/abs/2110.02811, doi:10.48550/ARXIV.2110.02811.

[201] Eslam Khalaf, Alex J. Kruchkov, Grigory Tarnopolsky, and Ashvin Vishwanath. Magic angle hierarchy in twisted graphene multilayers. *Physical Review B*, 100(8), August 2019. doi:10.1103/physrevb.100.085109.

[202] Jeong Min Park, Yuan Cao, Kenji Watanabe, Takashi Taniguchi, and Pablo Jarillo-Herrero. Tunable strongly coupled superconductivity in magic-angle twisted trilayer graphene. *Nature*, 590(7845):249–255, February 2021. doi:10.1038/s41586-021-03192-0.

[203] Fengcheng Wu, Timothy Lovorn, Emanuel Tutuc, and A. H. MacDonald. Hubbard model physics in transition metal dichalcogenide moiré bands. *Physical Review Letters*, 121(2), July 2018. doi:10.1103/physrevlett.121.026402.

[204] Bin-Bin Chen, Yuan Da Liao, Ziyu Chen, Oskar Vafek, Jian Kang, Wei Li, and Zi Yang Meng. Realization of topological Mott insulator in a twisted bilayer graphene lattice model. *Nature Communications*, 12(1), September 2021. doi:10.1038/s41467-021-25438-1.

[205] S. M. Girvin. The quantum Hall effect: Novel excitations and broken symmetries. In *Aspects topologiques de la physique en basse dimension. Topological aspects of low dimensional systems*, pages 53–175. Springer Berlin Heidelberg. doi:10.1007/3-540-46637-1_2.

[206] Jan Zaanen and Olle Gunnarsson. Charged magnetic domain lines and the magnetism of high-T_c oxides. *Physical Review B*, 40(10):7391–7394, October 1989. doi:10.1103/physrevb.40.7391.

[207] D. Poilblanc and T. M. Rice. Charged solitons in the Hartree-Fock approximation to the large-U Hubbard model. *Physical Review B*, 39(13):9749–9752, May 1989. doi:10.1103/physrevb.39.9749.

[208] M. Inui and P. B. Littlewood. Hartree-fock study of the magnetism in the single-band Hubbard model. *Physical Review B*, 44(9):4415–4422, September 1991. doi:10.1103/physrevb.44.4415.

[209] T. Giamarchi and C. Lhuillier. Variational monte carlo study of incommensurate antiferromagnetic phases in the two-dimensional Hubbard model. *Physical Review B*, 42(16):10641–10647, December 1990. doi:10.1103/physrevb.42.10641.

[210] V.J. Emery and S.A. Kivelson. Frustrated electronic phase separation and high-temperature superconductors. *Physica C: Superconductivity*, 209(4):597–621, May 1993. doi:10.1016/0921-4534(93)90581-a.

[211] S. A. Kivelson, E. Fradkin, and V. J. Emery. Electronic liquid-crystal phases of a doped Mott insulator. *Nature*, 393(6685):550–553, June 1998. doi:10.1038/31177.

[212] V. J. Emery, S. A. Kivelson, and J. M. Tranquada. Stripe phases in high-temperature superconductors. *Proceedings of the National Academy of Sciences*, 96(16):8814–8817, August 1999. doi:10.1073/pnas.96.16.8814.

[213] S. A. Kivelson, I. P. Bindloss, E. Fradkin, V. Oganesyan, J. M. Tranquada, A. Kapitulnik, and C. Howald. How to detect fluctuating stripes in the high-temperature superconductors. *Reviews of Modern Physics*, 75(4):1201–1241, October 2003. doi:10.1103/revmodphys.75.1201.

[214] Eduardo Fradkin, Steven A. Kivelson, and John M. Tranquada. Colloquium: Theory of intertwined orders in high temperature superconductors. *Reviews of Modern Physics*, 87(2):457–482, May 2015. doi:10.1103/revmodphys.87.457.

[215] Bo-Xiao Zheng, Chia-Min Chung, Philippe Corboz, Georg Ehlers, Ming-Pu Qin, Reinhard M. Noack, Hao Shi, Steven R. White, Shiwei Zhang, and Garnet Kin-Lic Chan. Stripe order in the underdoped region of the two-dimensional Hubbard model. *Science*, 358(6367):1155–1160, December 2017. doi:10.1126/science.aam7127.

[216] Edwin W. Huang, Christian B. Mendl, Hong-Chen Jiang, Brian Moritz, and Thomas P. Devereaux. Stripe order from the perspective of the Hubbard model. *npj Quantum Materials*, 3(1), April 2018. doi:10.1038/s41535-018-0097-0.

[217] Kazushige Machida. Magnetism in La2CuO4 based compounds. *Physica C: Superconductivity*, 158(1-2):192–196, April 1989. doi:10.1016/0921-4534(89)90316-x.

[218] Masaru Kato, Kazushige Machida, Hiizu Nakanishi, and Mitsutaka Fujita. Soliton lattice modulation of incommensurate spin density wave in two dimensional Hubbard model -a mean field study-. *Journal of the Physical Society of Japan*, 59(3):1047–1058, March 1990. doi:10.1143/jpsj.59.1047.

[219] A. A. Koulakov, M. M. Fogler, and B. I. Shklovskii. Charge density wave in two-dimensional electron liquid in weak magnetic field. *Physical Review Letters*, 76(3):499–502, January 1996. doi:10.1103/physrevlett.76.499.

[220] M. M. Fogler, A. A. Koulakov, and B. I. Shklovskii. Ground state of a two-dimensional electron liquid in a weak magnetic field. *Physical Review B*, 54(3):1853–1871, July 1996. doi:10.1103/physrevb.54.1853.

[221] R. Moessner and J. T. Chalker. Exact results for interacting electrons in high Landau levels. *Physical Review B*, 54(7):5006–5015, August 1996. doi:10.1103/physrevb.54.5006.

[222] Michael M. Fogler. Stripe and bubble phases in quantum Hall systems. In *High Magnetic Fields*, pages 98–138. Springer Berlin Heidelberg, 2002. doi:10.1007/3-540-45649-x_4.

[223] Florie Mesple, Ahmed Missaoui, Tommaso Cea, Loic Huder, Francisco Guinea, Guy Trambly de Laissardière, Claude Chapelier, and Vincent T. Renard. Heterostrain determines flat bands in magic-angle twisted graphene layers. *Physical Review Letters*, 127(12), September 2021. doi:10.1103/physrevlett.127.126405.

[224] Loïc Huder, Alexandre Artaud, Toai Le Quang, Guy Trambly de Laissardière, Aloysius G. M. Jansen, Gérard Lapertot, Claude Chapelier, and Vincent T. Renard. Electronic spectrum of twisted graphene layers under heterostrain. *Physical Review Letters*, 120(15), April 2018. doi:10.1103/physrevlett.120.156405.

[225] Zhen Bi, Noah F. Q. Yuan, and Liang Fu. Designing flat bands by strain. *Physical Review B*, 100(3), July 2019. doi:10.1103/physrevb.100.035448.

[226] Guoxin Cao. Atomistic studies of mechanical properties of graphene. *Polymers*, 6(9):2404–2432, September 2014. doi:10.3390/polym6092404.

[227] Yves H. Kwan, S. A. Parameswaran, and S. L. Sondhi. Twisted bilayer graphene in a parallel magnetic field. *Physical Review B*, 101(20), May 2020. doi:10.1103/physrevb.101.205116.

[228] Kasra Hejazi, Chunxiao Liu, Hassan Shapourian, Xiao Chen, and Leon Balents. Multiple topological transitions in twisted bilayer graphene near the first magic angle. *Physical Review B*, 99(3), January 2019. doi:10.1103/physrevb.99.035111.

[229] Shiang Fang, Stephen Carr, Ziyan Zhu, Daniel Massatt, and Efthimios Kaxiras. Angle-dependent *ab initio* low-energy Hamiltonians for a relaxed twisted bilayer graphene heterostructure, 2019. URL: https://arxiv.org/abs/1908.00058, doi:10.48550/ARXIV.1908.00058.

[230] Niels R. Walet and Francisco Guinea. Lattice deformation, low energy models and flat bands in twisted graphene bilayers, 2019. URL: https://arxiv.org/abs/1903.00340, doi:10.48550/ARXIV.1903.00340.

[231] H. Polshyn, Y. Zhang, M. A. Kumar, T. Soejima, P. Ledwith, K. Watanabe, T. Taniguchi, A. Vishwanath, M. P. Zaletel, and A. F. Young. Topological charge density waves at half-integer filling of a moiré superlattice. *Nature Physics*, 18(1):42–47, December 2021. doi:10.1038/s41567-021-01418-6.

[232] L. M. Sandratskii. Energy band structure calculations for crystals with spiral magnetic structure. *physica status solidi (b)*, 136(1):167–180, July 1986. doi:10.1002/pssb.2221360119.

[233] Sergej Y. Savrasov, Antonina Toropova, Mikhail I. Katsnelson, Alexander I. Lichtenstein, Vladimir Antropov, and Gabriel Kotliar. Electronic structure and magnetic properties of solids. *Zeitschrift für Kristallographie - Crystalline Materials*, 220(5-6):473–488, May 2005. doi:10.1524/zkri.220.5.473.65072.

[234] Masaki Oshikawa. Commensurability, excitation gap, and topology in quantum many-particle systems on a periodic lattice. *Physical Review Letters*, 84(7):1535–1538, February 2000. doi:10.1103/physrevlett.84.1535.

[235] Masaki Oshikawa. Topological approach to Luttinger's theorem and the Fermi surface of a Kondo lattice. *Physical Review Letters*, 84(15):3370–3373, April 2000. doi:10.1103/physrevlett.84.3370.

[236] Eslam Khalaf, Patrick Ledwith, and Ashvin Vishwanath. Symmetry constraints on superconductivity in twisted bilayer graphene: Fractional vortices, $4e$ condensates or non-unitary pairing, 2020. URL: https://arxiv.org/abs/2012.05915, doi:10.48550/ARXIV.2012.05915.

[237] Ethan Lake and T. Senthil. Reentrant superconductivity through a quantum Lifshitz transition in twisted trilayer graphene. *Physical Review B*, 104(17), November 2021. doi:10.1103/physrevb.104.174505.

[238] V.V. Cheianov, V.I. Fal'ko, O. Syljuåsen, and B.L. Altshuler. Hidden Kekulé ordering of adatoms on graphene. *Solid State Communications*, 149(37-38):1499–1501, October 2009. doi:10.1016/j.ssc.2009.07.008.

[239] Vadim V. Cheianov, Olav Syljuåsen, B. L. Altshuler, and Vladimir Fal'ko. Ordered states of adatoms on graphene. *Physical Review B*, 80(23), December 2009. doi:10.1103/physrevb.80.233409.

[240] Christopher Gutiérrez, Cheol-Joo Kim, Lola Brown, Theanne Schiros, Dennis Nordlund, Edward B. Lochocki, Kyle M. Shen, Jiwoong Park, and Abhay N. Pasupathy. Imaging chiral symmetry breaking from Kekulé bond order in graphene. *Nature Physics*, 12(10):950–958, May 2016. doi:10.1038/nphys3776.

[241] C. A. Marianetti and H. G. Yevick. Failure mechanisms of graphene under tension. *Physical Review Letters*, 105(24), December 2010. doi:10.1103/physrevlett.105.245502.

[242] Sandro Sorella, Kazuhiro Seki, Oleg O. Brovko, Tomonori Shirakawa, Shohei Miyakoshi, Seiji Yunoki, and Erio Tosatti. Correlation-driven dimerization and topological gap opening in isotropically strained graphene. *Physical Review Letters*, 121(6), August 2018. doi:10.1103/physrevlett.121.066402.

[243] Daejin Eom and Ja-Yong Koo. Direct measurement of strain-driven Kekulé distortion in graphene and its electronic properties. *Nanoscale*, 12(38):19604–19608, 2020. doi:10.1039/d0nr03565c.

[244] Maxim Kharitonov. Phase diagram for the $\nu = 0$ quantum Hall state in monolayer graphene. *Physical Review B*, 85(15), April 2012. doi:10.1103/physrevb.85.155439.

[245] Tianle Wang, Tomohiro Soejima, Daniel Parker, Johannes Hauschild, Nick Bultinck, and Michael Zaletel. Strain-induced Kekule spiral order in magic-angle graphene: a density matrix renormalization group study. *Bulletin of the American Physical Society*, 2022.

[246] Maine Christos, Subir Sachdev, and Mathias S. Scheurer. Superconductivity, correlated insulators, and Wess-Zumino-Witten terms in twisted bilayer graphene. *Proceedings of the National Academy of Sciences*, 117(47):29543–29554, November 2020. doi:10.1073/pnas.2014691117.

[247] Maine Christos, Subir Sachdev, and Mathias S. Scheurer. Correlated insulators, semimetals, and superconductivity in twisted trilayer graphene. *Physical Review X*, 12(2), April 2022. doi:10.1103/physrevx.12.021018.